
A 500 kHz high harmonics generation XUV light source for photoelectron spectroscopy

Johannes Michael Feldl



München 2016

Eine 500 kHz Hohe Harmonische Erzeugung XUV Lichtquelle zur Photoelektronen Spektroskopie

Johannes Michael Feldl

Masterarbeit
an der Fakultät für Physik
Ludwig-Maximilians-Universität
München

von
Johannes Michael Feldl
aus Eggenfelden

München, den 09.09.2016

Erstgutachter: Prof. Dr. Matthias Kling

Zweitgutachter: Dr. Ralph Ernstorfer

Contents

Introductory	vii
1 Theoretical Foundation	1
1.1 Ultrafast Optics	1
1.1.1 Electric field, Intensity and Phase	1
1.1.2 Pulse Spectrum	3
1.1.3 The Time-Bandwidth Product	3
1.1.4 Chirped Pulses	4
1.2 Nonlinear Optics	6
1.2.1 Basics of the Nonlinear Optics	6
1.2.2 Birefringence	8
1.2.3 Difference Frequency Generation and Optical Parametric Amplification	9
1.2.4 Theory of Optical Parametric Amplification	10
1.2.5 NOPA Theory	13
1.2.6 Supercontinuum Generation	16
1.3 High Harmonics Generation	17
1.3.1 Three-Step Model of Ultrashort Pulses Interacting with a Gaseous Medium in the Strong Field Regime	17
1.3.2 Wavelength Scaling	21
1.3.3 Phase-Matching	22
1.3.4 High Harmonics Spectrum	25
1.3.5 Interaction Gas	26
1.3.6 High Harmonics Generation at High-Repetition Rates	27
2 Generation of High-Repetition Rate XUV Pulses	29
2.1 Laser Setup and Beamline	30
2.2 Experimental HHG Setup	33
2.2.1 HHG Chamber and Gas Target	33
2.2.2 The Gas-Catch	40
2.2.3 Spectral Monochromatization	44
2.3 XUV Characterization	49
2.3.1 Spectral Characterization	49
2.3.2 XUV Flux	57

2.3.3	XUV Spot Profile	62
3	High-Repetition Rate XUV Photoelectron Spectroscopy and Future Im- plementations	65
3.1	The trARPES Beamline	67
3.2	ARPES and Space-Charge Effects	70
3.3	Temporal Resolution with LAPE	72
3.4	Time-resolved ARPES on WSe ₂	74
3.5	NOPA as Pump Source	76
3.5.1	Experimental Challenges and Realization	76
3.5.2	First Results	78
4	Summary	81
	Acknowledgements	91

Introductory

Time- and Angle-Resolved Photoelectron Spectroscopy with High-Repetition Rate XUV Pulses

A new group of materials attracted tremendous attention over the last few years, and it is still growing. Meant are stacked heterostructures, consisting of different two-dimensional layers with different properties, such as electrical insulation, conduction or semiconduction [1]. A broad variety of individual designed nano-electronics are promised. Transition metal dichalcogenides (TMDCs) can be manufactured in monolayer thicknesses [2]. This is not the only characteristic of TMDCs, making them an ideal candidate to allow for such constructions. In plane of a monolayer, they are strongly bound via covalent interactions, whilst between the layers, only weak van der Waals forces apply. These however alter the band structure. TMDCs, which are semiconducting with an indirect band gap when they are in a bulk crystal, can become a semiconductor with a direct band gap when they shrink down to a few layers, promising to be the new electrical transistor on an atomic scale [3].

The investigation of these fascinating materials is one of the main goals of our research group. In order to do so we apply, in the words of Geim et al. [1], one of the 'heavy artilleries of physics', being photoelectron spectroscopy (PES). PES can provide energy and momentum resolution of the investigated electronic states, because in the process of photoemission, the momentum vector parallel to the surface is conserved. Thus, detecting the kinetic energy and the angle of emission, which is angle-resolved photoelectron spectroscopy (ARPES), these informations can be achieved. In addition, PES is highly surface sensitive due to the very small mean free path of photoelectrons and thus perfect to probe only a few layers of a bulk sample, resolving in-plane characteristics. There is even the possibility of observing dynamics of non-equilibrium states via time-delayed pump-probe experiments [4, 5]. The left graphic of figure 1 shows the principle of this time-resolved APRES (trARPES). Usually unoccupied states, which are very important for the electrical properties of a material, can be occupied with electrons by optical pumping (done by the so called pump pulse). High energetic photons then are able to photoemit these electrons, allowing for their investigation in energy and momentum. When either the pump or probe pulse is delayed with respect to the other, the time evolution of this electrons can be observed, yielding informations of important physical processes such as lifetimes or exciton formations. In order to do

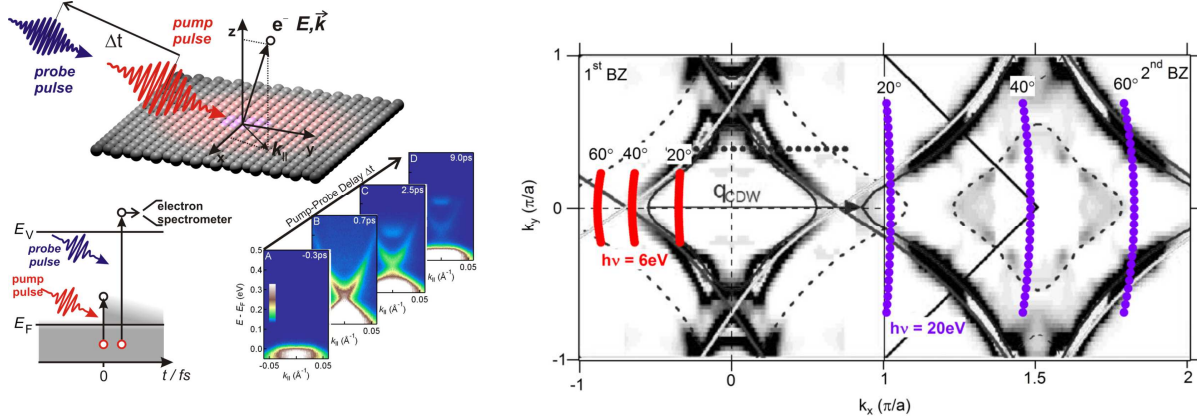


Figure 1: *Left)* Scheme of the principle of trARPES measurements. A pump beam excites electrons into non-equilibrium states and a high energetic probe pulse photoemits them. The detected photoelectrons provide informations of the energy and momentum spectrum of the crystal. By delaying pump and probe pulse to each other, movies of these dynamic processes can be taken. *Right)* Shown is the Brillouin zone of CeTe_3 , displaying the need for ≈ 20 eV of probe photon energies to cover the full Brillouin zone. Figure courtesy of P. Kirchmann.

access the full Brillouin zone, probing pulses of extreme ultraviolet¹(XUV) light are necessary. This is indicated on the right graphic of figure 1, where the first Brillouin zone of CeTe_3 is shown and how much of the momentum space with 6 eV or 20 eV can be accessed.

Another important factor for ARPES measurements is the influence of space charges [6]. Due to their Coulomb interaction, electrons repel each other, whereby their energy and momentum information gets modified. This spread lowers the achievable resolution of the measurement. An ideal source would emit only one electron per pulse at a very high repetition rate to counteract the low counting statistics.

At repetition rates of several hundreds of kHz the 4th harmonic of a Ti:sapphire output can be generated, offering high counting statistics but only ≈ 6 eV photon energy, which limits the accessible Brillouin zone to its center. High harmonics generation (HHG) in contrast allows for high enough photon energies. But HHG requires laser intensities of $\approx 10^{14}$ W/cm² which was mainly accessible by Ti:sapphire lasers with low repetition rates in the regime of a few kHz.

New laser developments allow us to bridge this gap with a 500 kHz high-repetition rate HHG with photon energies of 22 eV. This enables probing of the complete first Brillouin zone with high counting statistics.

The main scope of this thesis was to establish this XUV HHG source and to build a

¹Photon energies in the regime of 10 eV to 124 eV

beamline for trARPES measurements. Therefore a fiber-slab combination, driving an optical parametric chirped pulse amplifier (OPCPA) is in use to generate high harmonics in a rare gas jet under tight focusing condition. In the harmonic's spectrum, a single harmonic needed to be isolated and UHV conditions must be provided in order to run surface sensitive PES. As an improvement of the system, an additional NOPA as trARPES pump source, based on residual beams, was investigated

Outline

The first chapter of this thesis briefly covers the theoretical aspects needed for the various topics covered within this work, such as ultrashort laser pulses, optical parametric amplifiers and high harmonic generation.

Chapter two introduces the used laser system and describes the considerations and experimental approaches to fulfill the requirements for an efficient HHG and trARPES application. Afterwards, the XUV light source is characterized.

In the third chapter, the final trARPES beamline is shown and further characterizations of the light source based on first trARPES measurements are given. As an outlook for future implementations, a noncollinear OPA (NOPA) was tested as possible tunable pump source.

Chapter 1

Theoretical Foundation

This thesis covers topics which all take place in the regime of ultrashort phenomena and a prime attention on electromagnetic bursts in the femtosecond regime. Therefore a brief introduction will be given, covering the electromagnetic field, its intensity and phase as well as phase effects which modify the temporal properties of a pulse in an essential way for the working principle of the later on described OPCPA and NOPA. Accompanying ultrashort pulses, nonlinear optics play a crucial role at multiple stages in this experimental work *e. g.* the second harmonic generation, the optical parametric amplifier and the high harmonics generation. All the essential principles are introduced to the reader, being able to continue with the subsequent chapters.

1.1 Ultrafast Optics

1.1.1 Electric field, Intensity and Phase

Ultrashort light pulses are electromagnetic waves which temporal appearances is a product of a fast oscillating field vector and a pulse shaping envelope function. In full generality this can be a complex function in space and time $\mathcal{E}(\mathbf{x}, \mathbf{y}, \mathbf{z}, t)$ we assume a linear polarized field and even neglect the spatial portion of the field since the main interest of the following discussion lies on the temporal behavior. Following Ref. [7] the now scalar equation of the electric field can be written as:

$$\mathcal{E}(t) = \frac{1}{2} \sqrt{I(t)} e^{i[\omega_0 t - \phi(t)]} + c.c. \quad (1.1)$$

with the carrier angular frequency ω_0 and the time dependent intensity $I(t)$ and phase $\phi(t)$ whereas t is set to be the time in the pulse's reference frame and *c.c.* is understood as usual as *complex conjugate*. For the sake of a simplified analytic, this part will be ignored, resulting in a complex pulse field with the complex amplitude:

$$E(t) \equiv \sqrt{I(t)} e^{-i\phi(t)} \quad (1.2)$$

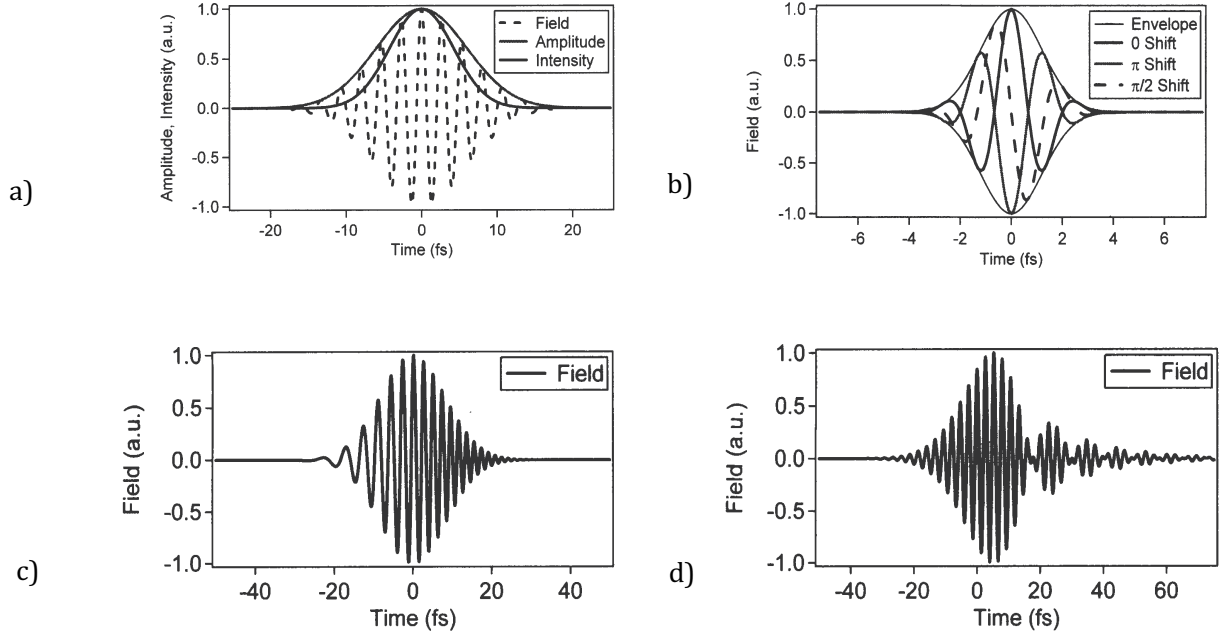


Figure 1.1: *a)* Electric field and the intensity of an ultrashort pulse are shown. *b)* Phase shifts in zeroth order delay the carrier wave relative to the envelope. *c)* Pulse with a positive quadratic temporal phase. The instantaneous frequency becomes a linear function of time. *d)* Shown is a positive cubic temporal phase, leading to side pulses after the main peak. Figures adopted from [7].

Since it is just the amplitude, the fast oscillation carrier field is omitted and multiplied by the factor of 2. For the intensity, which is the quantity we have experimental access to via measuring the power. For the moment just the shape of the pulse is of interest, so the real *irradiance* does not be taken into account and constant factors such as the *speed of light* and the *permittivity* can also be omitted. In this case following equation holds:

$$I(t) = |E(t)|^2 \quad (1.3)$$

In 1.1 a) the rapidly oscillating electric field and its envelope is depicted. Furthermore also the intensity envelope is shown where it can be seen that in this case of a Gaussian pulse shape, that the intensity acts like a gating in time, narrowing the pulse, but the general pulse shape stays the same. From equation 1.2 the phase can be retracted:

$$\phi(t) = -\arctan \left\{ \frac{\text{Im}[E(t)]}{\text{Re}[E(t)]} \right\} \quad (1.4)$$

1.1.2 Pulse Spectrum

Fourier's theorem states that a function in time can be converted in the frequency domain containing the same amount of information as before and back-converted. The corresponding equations are as following¹:

$$\tilde{\mathcal{E}}(\omega) = \int_{-\infty}^{\infty} \mathcal{E}(t) e^{-i\omega t} dt \quad (1.5)$$

$$\mathcal{E}(t) = \frac{1}{2\pi} \int_{-\infty}^{\infty} \tilde{\mathcal{E}}(\omega) e^{-i\omega t} d\omega \quad (1.6)$$

In contrast to the time domain, for the frequency domain it is convention to use transform the real electric field to yield a not to zero shifted spectrum. The transformation produces an equal spectrum in for negative frequencies which can be neglected. Equation 1.5 applied to the real electric field results in:

$$\tilde{\mathcal{E}}(\omega) = \sqrt{S(\omega)} e^{-i\varphi(\omega)} \quad (1.7)$$

with $S(\omega)$ and $\varphi(\omega)$ being the spectrum and the spectral phase respectively. For the spectrum applies:

$$S(\omega) = |\tilde{\mathcal{E}}(\omega)|^2 \quad (1.8)$$

Also for the spectral phase holds a similar expression as for the temporal one:

$$\varphi(\omega) = -\arctan \left\{ \frac{\text{Im}[\tilde{\mathcal{E}}(\omega)]}{\text{Re}[\tilde{\mathcal{E}}(\omega)]} \right\} \quad (1.9)$$

1.1.3 The Time-Bandwidth Product

There is a quantity called the *time-bandwidth product* (TBP) and as the name suggests it is the product of the pulse duration τ in time and the spectral width $\Delta\nu$.

$$\tau \Delta\nu = c_B \quad (1.10)$$

Here c_B is a dimensionless constant which can not fall below a profile dependent value, since the temporal and spectral width are related to each other through the Fourier transformation. The minimum value is reached, when the temporal and spectral phases are a constant, meaning the pulses do not show a substructure but a 'clean' pulse shape, as will be further discussed in 1.1.4. Such pulses are called to be *bandwidth limited* or *Fourier limited*. Since the Fourier transformation is linear it can not happen that either the spectral or the temporal phase are linear, they occur simultaneously. The Fourier transformation and

¹Fourier transformations exhibit a \sim over the equation.

the TBP make clear that one of the necessary – but not sufficient – requirements for the generation of an ultrashort pulse is a broad spectrum. A given spectrum hereby determines the minimal pulse duration which is achievable. In the experiment described in this thesis, this fact is of crucial importance for the OPCPA as well as the NOPA to amplify a sufficient broad spectrum to support the wanted pulse duration. It is very important to notice that values of c_B found in the literature can differ a lot, caused by the fact that there is no unique definition of the temporal and spectral width. Very common and often used are the Full Width at Half Maximum (FWHM), the $1/e$ amplitude of the electric field or the second-order momentum which are all briefly introduced in Ref. [7] with their individual advantages and drawbacks. To define such widths it is also important to assume a pulse shape. In reality this is often just an assumption and the different pulse shapes have different TBPs as well. For a Gaussian pulse shape with a width definition according to the FWHM has a TBP of $c_{B,Gaussian} = 0.441$ and a derivation of this can be found in [8].

1.1.4 Chirped Pulses

Having a closer look at the temporal phase $\phi(t)$ of equation 1.2 a total phase of the wave looks like this:

$$\phi_0 = \omega(t) - \phi(t) \quad (1.11)$$

With $\phi(t)$ containing frequency vs. time information a instantaneous angular frequency $\omega_{inst}(t)$ and a instantaneous frequency $\nu_{inst}(t)$ of the pulse can be defined:

$$\omega_{inst}(t) \equiv \omega_0 - \frac{d\phi}{dt} \quad (1.12)$$

$$\nu_{inst}(t) = \nu_0 - \frac{1}{2\pi} \frac{d\phi}{dt} \quad (1.13)$$

A Taylor expansion around time $t = 0$ of the temporal phase can be written as:

$$\phi(t) = \phi_0 + t\phi_1 + t^2\phi_2/2 + \dots \quad (1.14)$$

Information about time vs. frequency is given in the spectral phase so a group delay $t_{group}(\omega)$ can be defined:

$$t_{group}(\omega) = \frac{d\phi}{d\omega} \quad (1.15)$$

In a similar fashion can the spectral frequency be expanded in a Taylor series around the central angular carrier frequency:

$$\varphi(\omega) = \varphi_0 + (\omega - \omega_0)\varphi_1 + (\omega - \omega_0)^2\varphi_2/2 + \dots \quad (1.16)$$

Now we will have a closer look on the effect of the first orders of this expansion on a pulse.

Zeroth-order Phase

Even if the zeroth-order phase term ϕ_0 often is called to be the *absolute phase* it is more a relative phase. It describes the relative phase of the carrier wave to the envelope. Usually this does not have a huge impact on the pulse, since the shape stays unaffected but for the shortest, so called few-cycle pulses where the *slowly varying envelope approximation* (SVEA) [9, 10] is not valid anymore, it can be of importance [11, 12]. Such a case is depicted in figure 1.1 b) where the maximum electrical field strength depends drastically on the zeroth-order phase.

First-order Phase

Fourier transforming a pulse with a non-zero spectral phase ϕ_1 results in $E(t - \tau)$, a shift of the pulse envelope in time. In most of the applications this is uncritical as well and not shown in figure 1.1.

Second-order Phase

A pulse is *linearly chirped* when a non-zero ϕ_2 is present, resulting in a linear change of the instantaneous frequency containing a pulse in time, compare with figure 1.1 c). When a pulse propagates through a medium that is not vacuum, a positive linear chirp will be induced leading to a stretching of an unchirped initial pulse where the red frequency components are before the blue ones in time. The inversion of this also exists and the convention for this is to call it negatively chirped. The complex field of a Gaussian pulse affected by a quadratic temporal phase is:

$$E(t) = [E_0 \exp(-at^2)] \exp(ibt^2) \quad (1.17)$$

with the constant E_0 , roughly the pulse duration $1/\sqrt{a}$ and the chirp parameter b . Fourier transformed it looks like this:

$$\tilde{E}(\omega) = \frac{\sqrt{\pi}}{a - ib} \exp \left[-\frac{\omega^2}{4(a - ib)} \right] \quad (1.18)$$

This order of chirp is mainly used in the OPCPA to stretch the incoming pulse such in time, that frequencies are separated in time, with two main effects, being lowering the intensity and therefore the impact on optical components and for the possibility to time-gate parts of the spectrum 1.2.5.

Third and Higher-order Phases

Third-order phases can have a dramatic effect on the pulse shape. When the third-order coefficient ϕ_3 is positive, there are oscillations after the main pulse and before, when ϕ_3

is negative, compare with figure 1.1 d). With increasing order of the phase term, the pulse becomes more and more complex. But at the same time do this distortions get less significant and can be neglected if not a few-cycle pulse is affected.

1.2 Nonlinear Optics

1.2.1 Basics of the Nonlinear Optics

Nonlinear optics describes a field of physics where the presence of a light field modifies the optical properties of matter in such a way, that its response to the light field is not linear anymore, but deviating from that. It is no coincidence that one of these effects, the *second harmonic generation* (SHG) [13] was first discovered one year after the invention of the first laser in 1960 by Maiman [14]. For nonlinear optical effects the light field needs to be in the order of the atomic electric field strength $E_{\text{at}} = e/(4\pi\epsilon_0 a_0^2)$ which is orders of magnitude higher than everything we encounter in nature in our daily life [15]. But laser light sources provide a powerful tool which can be very tightly focused to a couple of microns and all its energy can be crammed into ultrashort pulses of a few femtoseconds, resulting in intensities of 10^{12} W/cm² and way beyond, where nonlinear effects show a strong presence!

The wave equation is the fundamental relation of optics, here in just one spatial dimension for simplicity:

$$\frac{\partial^2 \mathcal{E}}{\partial z^2} - \frac{1}{c_0^2} \frac{\partial^2 \mathcal{E}}{\partial t^2} = \mu_0 \frac{\partial^2 \mathcal{P}}{\partial t^2} \quad (1.19)$$

with c_0 as the speed of light in vacuum, μ_0 as the magnetic permeability of free space, \mathcal{E} is the real electric field and \mathcal{P} is the real induced polarization [7]. The latter contains the information on how the light field influences the medium and in return the effect of the medium back to the light field.

In the linear approach, the induced polarization shows a linear dependence on the electric field

$$\mathcal{P} = \epsilon_0 \chi^{(1)} \mathcal{E} \quad (1.20)$$

where the new quantities ϵ_0 and $\chi^{(1)}$ represent the electric permittivity of free space and the linear susceptibility, respectively. For higher intensities though, this approach is not sufficient but higher-order terms must be included in a perturbative treatment:

$$\mathcal{P} = \epsilon_0 \left[\chi^{(1)} \mathcal{E} + \chi^{(2)} \mathcal{E}^2 + \chi^{(3)} \mathcal{E}^3 + \dots \right] \quad (1.21)$$

with $\chi^{(n)}$ being the n th-order susceptibility, which are fairly weak at low intensities for $n > 1$ but since they grow with the n th-order of the electric field, their influence gains great growth for high intensities!

The induced polarization can be understood as a source term. Extending it into the nonlinear regime by one order, meaning consider \mathcal{P} up to $\chi^{(2)}$ yields some very interesting

effects. Therefore let us consider two beams with time and spatial dependence [7]:

$$\begin{aligned}\mathcal{E}(\vec{r}, t) = & \frac{1}{2}E_1(\vec{r}, t) \exp [i(\omega_1 t - \vec{k}_1 \cdot \vec{r})] \\ & + \frac{1}{2}E_2(\vec{r}, t) \exp [i(\omega_2 t - \vec{k}_2 \cdot \vec{r})] + c.c.\end{aligned}\quad (1.22)$$

with the complex field $E_m(\vec{r}, t)$ and $m = 1, 2$ for beam 1 and 2 respectively. To see the interacting term with $\chi^{(2)}$ the square of this field is needed:

$$\begin{aligned}\mathcal{E}^2(\vec{r}, t) = & \frac{1}{4}E_1^2 \exp [2i(\omega_1 t - \vec{k}_1 \cdot \vec{r})] \\ & + \frac{1}{2}E_1 E_1^* + \frac{1}{4}E_1^{*2} \exp [-2i(\omega_1 t - \vec{k}_1 \cdot \vec{r})] \\ & + \frac{1}{4}E_2^2 \exp [2i(\omega_2 t - \vec{k}_2 \cdot \vec{r})] + \frac{1}{2}E_2 E_2^* \\ & + \frac{1}{4}E_2^{*2} \exp [-2i(\omega_2 t - \vec{k}_2 \cdot \vec{r})] \\ & + \frac{1}{2}E_1 E_2 \exp \{i[(\omega_1 + \omega_2)t - (\vec{k}_1 + \vec{k}_2) \cdot \vec{r}]\} \\ & + \frac{1}{2}E_1^* E_2^* \exp \{-i[(\omega_1 + \omega_2)t - (\vec{k}_1 + \vec{k}_2) \cdot \vec{r}]\} \\ & + \frac{1}{2}E_1 E_2^* \exp \{i[(\omega_1 - \omega_2)t - (\vec{k}_1 - \vec{k}_2) \cdot \vec{r}]\} \\ & + \frac{1}{2}E_1^* E_2 \exp \{-i[(\omega_1 - \omega_2)t - (\vec{k}_1 - \vec{k}_2) \cdot \vec{r}]\}.\end{aligned}\quad (1.23)$$

Each of this lines shows some interesting feature, especially when considering the expressions for the angular frequencies and the k -vectors. The right hand side of the first two lines display a frequency at $2\omega_1$ which means that a new beam is generated, propagating along the same direction as the original one, but with a doubled photon energy. This is the important process of the already mentioned SHG which is several times implemented in the experimental setup of this thesis. There is also a static zero-frequency term, called *optical rectification* but usually it is small enough to be neglected.

The following two lines are the same as the first two but for the second incoming wave. In the next two lines the field has a frequency of $\omega_1 + \omega_2$ hence this effect is called *sum frequency generation* (SFG). The last two lines exhibit the fundamental principal of the OPCPA and NOPA where the new generated wave has a frequency of $\omega_1 - \omega_2$. The new beams of the latter two effects also follow a new, from the the fundamental beams deviating, direction, making it easy to separate them, compare $\vec{k}_1 + \vec{k}_2$ and $\vec{k}_1 - \vec{k}_2$.

In order that these effects occur, they need to fulfill energy and momentum conservation, which is in the community of ultrafast optics also called, they need to be *phase-matched*. Here presented for a N-wave-mixing process and a canceled \hbar for the energy conservation:

$$\omega_0 = \pm\omega_1 \pm \omega_2 \pm \dots \pm \omega_N \quad (1.24)$$

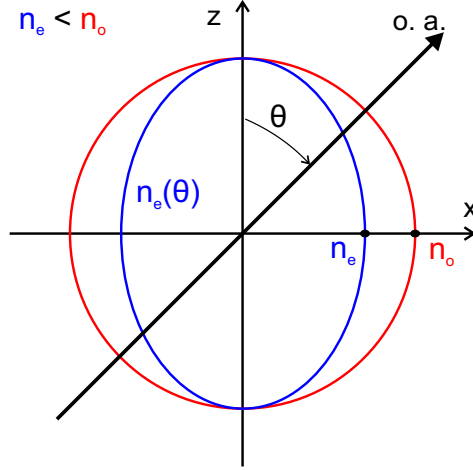


Figure 1.2: Scheme of the refractive indices of a negative uniaxial crystal.

$$\vec{k}_0 = \pm \vec{k}_1 \pm \vec{k}_2 \pm \dots \pm \vec{k}_N \quad (1.25)$$

Here the index 0 denotes the generated and/or signal beam. Beside the requirement of high intensities, the necessity of phase-matching prevents us from observing nonlinear effects in regular life and only just one of the above described second order effects can occur for one set of conditions.

Restricting the beams to be collinear for the case of DFG with the conservation rules being $\omega_p = \omega_s + \omega_i$ and $k_p = k_s + k_i$ and having the relation $k_j = \omega_j n(\omega_j)/c_0$ in mind with $j = p, s, i$ whereas $\omega_p > \omega_s > \omega_i$, equation 1.24 can be transformed into:

$$(n(\omega_p) - n(\omega_i)) \omega_p = (n(\omega_s) - n(\omega_i)) \omega_s \quad (1.26)$$

Renaming $A = n(\omega_p) - n(\omega_i)$ and $B = n(\omega_s) - n(\omega_i)$ it is clear, that this equation is not fulfilled with an isotropic medium with normal dispersion. There, for the visible frequency range, $n(\omega_p) > n(\omega_s) > n(\omega_i)$ holds true, resulting in $A > B$ but for the same time $\omega_p > \omega_s$ is given which contradicts the initial constraint in equation 1.26.

To solve this problem, dispersion with $n(\omega_p) < n(\omega_s)$ is needed. Since this is an issue that covers a lot of important nonlinear phenomena such as SHG and the OPA process, the next section will be about such materials having the desired optical properties, before the principal of the DFG and by that, of the OPA, is described.

1.2.2 Birefringence

Special requirements are needed to match the phase of two beams of different frequencies in a dispersive medium. Isotropic media, *e. g.* fused silica or CaF_2 , show a normal dispersion and for this reason do not work to fulfill the phase matching requirement. However, a group of uniaxial crystals overcomes this problem. Due to their anisotropic unit cell, the materials response to the electric field depends on its polarization, because the electrons experience a

different behavior depending on the direction of the asymmetric crystal they are driven by the field.

One special direction in such crystals is called the *optical axis* (z axis) [16]. The *principal plane* refers to the plane containing the z axis and the wave vector \vec{k} of the incident wave. A wave with perpendicular polarization to this plane is called the *ordinary beam* (o) and a parallel polarized wave is known as an *extraordinary beam* (e). The ordinary beam obtains the same refractive index for all directions, whereas for the extraordinary beam the refractive index does depend on the direction. This is also called *birefringence*.

Since the principle of superposition holds, every randomly polarized beam can be decomposed into an ordinary and an extraordinary beam. Along the optic axis the refractive index is equal for both polarizations. The refractive indexes for the ordinary and the extraordinary beam are known as n_o and n_e respectively.

The angle dependence of $n_e(\theta)$ can be expressed as follows, whereas θ as the polar angle between the z axis and the k -vector [16].

$$n_e(\theta) = n_o \sqrt{\frac{1 + \tan^2 \theta}{1 + (n_o/n_e)^2 \tan^2 \theta}} \quad (1.27)$$

Is $n_e < n_o$ then the crystal is negative uniaxial (see figure 1.2), otherwise it is positive. Completely independent is n_e of the azimuthal angle ϕ between the projection of the k -vector onto the xy plane and the x axis.

Another effect occurs for the extraordinary beam in an uniaxial crystal. The direction of the phase \vec{k} and the one of the energy (Poynting vector S) generally does not coincide. This so-called *walk-off angle* can be calculated via:

$$\rho(\theta) = \pm \arctan [(n_o/n_e)^2 \tan \theta] \mp \theta \quad (1.28)$$

where the upper signs are to be used for a negative and the lower ones for a positive uniaxial crystal. In our experiment, we use nonlinear crystals of the type β -BaB₂O₄, also known as *beta-barium borate* (BBO).

1.2.3 Difference Frequency Generation and Optical Parametric Amplification

A basic explanation of the principals of DFG is fairly easy done. A high intense *pump* beam at the frequency ω_p amplifies a low intensity *signal* beam with ω_s at which a third beam, the *idler* beam at a frequency ω_i is generated. The signal beam before the amplification is called the *seed* beam. The photon energy of the beams scales like $\omega_p > \omega_s > \omega_i$.

The three beams must be phase-matched in a nonlinear crystal to satisfy energy and momentum conservation.

$$\omega_p = \omega_s + \omega_i \quad (1.29)$$

$$\vec{k}_p = \vec{k}_s + \vec{k}_i \quad (1.30)$$

The amplification range of the signal can in principal reach from ω_p to $\omega_p/2$, the so-called degeneracy condition where signal and idler have the same frequency [17]. For an efficient process, pump intensities in the order of tens of GW/cm² are needed.

Optical parametric amplification follows the same rules and the actual only difference to DFG is in the intensity of the pump beam. When both, pump and signal are comparable in intensity, the process is called DFG, otherwise, with a much higher pump intensity, it is called OPA.

1.2.4 Theory of Optical Parametric Amplification

For the derivation of the general properties of the optical parametric amplifying process as done in Ref. [17] we act on the assumption of a monochromatic plane wave at frequency ω , linearly polarized and propagating into the z direction in a medium with nonlinear polarization at the same frequency. Under these conditions, the electric field and nonlinear polarization are

$$\mathcal{E}(z, t) = \text{Re} \{ A(z) \exp [i(\omega t - kz)] \} \quad (1.31)$$

$$\mathcal{P}^{\text{NL}}(z, t) = \text{Re} \{ P^{\text{NL}}(z) \exp [i(\omega t - k_p z)] \}, \quad (1.32)$$

with $A(z)$ being the vector potential and $P^{\text{NL}}(z)$ the complex nonlinear polarization. By modifying the wave equation 1.19 with the phase velocity $v = c_0/n$ instead of the speed of light in vacuum c_0 for a dispersive material, the needed derivatives for solving this equation can be calculated:

$$\frac{\partial^2 \mathcal{P}^{\text{NL}}}{\partial t^2} = -\omega^2 P^{\text{NL}} \exp [i(\omega t - k_p z)] \quad (1.33)$$

$$\frac{\partial^2 \mathcal{E}}{\partial t^2} = -\omega^2 A(z) \exp [i(\omega t - kz)] \quad (1.34)$$

$$\frac{\partial^2 \mathcal{E}}{\partial z^2} = \left[\frac{\partial^2 A}{\partial z^2} - 2ik \frac{\partial A}{\partial z} - k^2 A(z) \right] \exp [i(\omega t - kz)] \quad (1.35)$$

Taking advantage of the *slowly varying amplitude approximation*, the second derivative can be neglected when following relation is true:

$$\left| \frac{\partial^2 A}{\partial z^2} \right| \ll 2k \left| \frac{\partial A}{\partial z} \right| \quad (1.36)$$

With this approximation and replacing $k = \omega n/c_0$ the derivatives can be inserted into the wave equation and following propagation equation is yielded:

$$\frac{\partial A}{\partial z} = -i \frac{\mu_0 c_0 \omega}{2n} P^{\text{NL}} \exp [-i(k_p - k)z] \quad (1.37)$$

Considering the interaction of a pump, signal and idler beam with $\omega_p > \omega_s > \omega_i$ and $\omega_p = \omega_s + \omega_i$ in a second order nonlinear polarization medium, the component of this nonlinear polarization vector along direction n is expressed as:

$$P_n^{\text{NL}} = \epsilon_0 \chi_{nml}^{(2)} E_m E_l \quad (1.38)$$

where n, m and l each can take on of the spatial coordinate axis x, y and z. The third-rank second order nonlinear susceptibility tensor $\chi^{(2)}$ is used in the Einstein summation convention. For the derivation a collinear OPA with parallel wave vectors for all three beams is assumed. With

$$E_n = A_n e^{i(k_n z)} \quad (1.39)$$

and the resulting nonlinear polarization

$$P_n^{\text{NL}} = \epsilon_0 \chi_{nml}^{(2)} A_m A_l e^{i(k_m + k_l z)} \quad (1.40)$$

inserted into equation 1.37, the following coupled equations can be derived:

$$\frac{\partial A_i}{\partial z} = -i \frac{\omega_i d_{\text{eff}}}{n_i c_0} A_s^* A_p \exp(-i\Delta k z) \quad (1.41)$$

$$\frac{\partial A_s}{\partial z} = -i \frac{\omega_s d_{\text{eff}}}{n_s c_0} A_i^* A_p \exp(-i\Delta k z) \quad (1.42)$$

$$\frac{\partial A_p}{\partial z} = -i \frac{\omega_p d_{\text{eff}}}{n_p c_0} A_i A_s \exp(-i\Delta k z) \quad (1.43)$$

where the so-called *effective nonlinear optical coefficient* $d_{\text{eff}} = \frac{1}{2} \chi_{nml}^{(2)}$ which depends on the polarization and the propagation direction of the three beams was introduced. See *e. g.* reference [15] for more information.

The coupled equations can be integrated for the beam propagating in a nonlinear crystal with length L . In parametric amplification process, the pump beam is much stronger than the signal beam and pump depletion can be neglected, leading to the assumption that $A_p \cong \text{const.}$ From the seed beam, a initial signal intensity A_{s0} is present and no initial idler beam $A_{i0} = 0$ is assumed.

$$\begin{aligned} A_s(L) &= -i \frac{\omega_s d_{\text{eff}}}{n_s c_0} A_i^* A_p \int_0^L e^{-i\Delta k z} dz \\ &= -i \frac{\omega_s d_{\text{eff}}}{n_s c_0} A_i^* A_p \left(\frac{e^{-i\Delta k L} - 1}{i\Delta k} \right) \end{aligned} \quad (1.44)$$

The interesting quantity that can be measured is the intensity, which can be obtained by the magnitude of the time-averaged Poynting vector, which in this case is [15]:

$$I_n = 2n_n \epsilon_0 c_0 |A_n|^2 \quad (1.45)$$

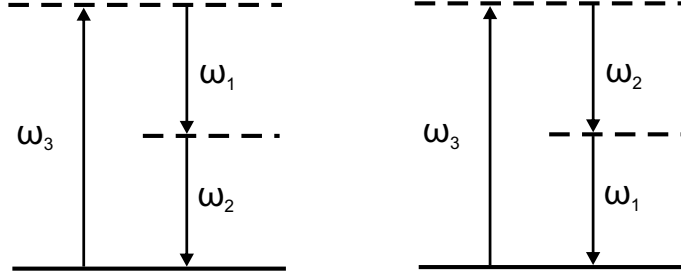


Figure 1.3: Decay of the pump photon in either an signal or idler photon. Either way, the other photon is emitted as well.

Now the signal and idler intensity after a nonlinear crystal with length L can be deviated, and the results are [17]:

$$I_s(L) = I_{s0} \left[1 - \frac{\Gamma^2}{g^2} \sinh^2(gL) \right] \quad (1.46)$$

$$I_i(L) = I_{i0} \frac{\omega_i}{\omega_s} \frac{\Gamma^2}{g^2} \sinh^2(gL) \quad (1.47)$$

and

$$g = \sqrt{\Gamma^2 - \left(\frac{\Delta k}{2} \right)^2} \quad (1.48)$$

$$\Gamma^2 = \frac{\omega_i \omega_s d_{\text{eff}}^2 |A_p|^2}{n_i n_s c_0^2} = \frac{2 \omega_i \omega_s d_{\text{eff}}^2 I_p}{n_i n_s n_p \epsilon_0 c_0^3} = \frac{8 \pi^2 d_{\text{eff}}^2 I_p}{n_i n_s n_p \lambda_i \lambda_s \epsilon_0 c_0} \quad (1.49)$$

For a maximum of amplification, perfect phase-matching ($\Delta k = 0$) is necessary.

A simplification of equation 1.46 and 1.47 can be done in the large gain approximation ($\Gamma L \gg 1$):

$$I_s(L) \cong \frac{1}{4} I_{s0} e^{2\Gamma L} \quad (1.50)$$

$$I_i(L) \cong \frac{\omega_i}{4\omega_s} I_{s0} e^{2\Gamma L} \quad (1.51)$$

Here it can be seen, that with growing crystal length, the intensity of the signal as well as of the idler beam growth exponentially. Starting at the beginning of the crystal, then a high intensity beam amplifies a relatively weak seed beam, which stimulates this process. Thereby a pump photon is killed and a signal and idler are created. As depicted in figure 1.3 the pump photon decay is stimulated from both, the signal and idler photon. This means, a signal photon which stimulates a conversion of a pump photon creates another signal photon and an idler photon. Each signal photon can now stimulate this process on its own again, but also the idler photon does so, resulting again in a new signal and idler

photon. That is a positive feedback explaining the exponential growth of the amplified waves.

It can be shown [17], that phase matching for a type I negative crystal is achieved for the phase matching angle θ_m (defined as the angle between the propagating beams and the optical axis of the nonlinear crystal) being

$$\theta_m = \arcsin \left[\frac{n_{ep}}{n_{ep}(\theta_m)} \sqrt{\frac{n_{op}^2 - n_{ep}^2(\theta_m)}{n_{op}^2 - n_{ep}^2}} \right], \quad (1.52)$$

following the here introduced index convention.

Parametric Amplification for Ultrashort Pulses

Ultrashort pulses differ from continuous waves (which were assumed so far) not only in time, but also in frequency. Single-frequency ultrashort pulses do not exist. Hence group velocity mismatches (GVM) between the different pulses need to be considered. The GVM between the pump and the amplified beams sets a limit to the interaction length and GVM between the two amplified beams reduces the phase matching bandwidth. Latter can be estimated within the large-gain approximation to a phase matched FWHM bandwidth of [17]

$$\Delta\nu \cong \frac{2(\ln 2)^{1/2}}{\pi} \left(\frac{\Gamma}{L} \right)^{1/2} \frac{1}{\left| \frac{1}{v_{gs}} - \frac{1}{v_{gi}} \right|}, \quad (1.53)$$

with the group velocities v_{gs} for the signal beam and v_{gi} for the idler beam.

1.2.5 NOPA Theory

The discussion of the theory given here, should be understood as an extension of the description of a OPA and will just cover NOPA specific topics.

As the name suggests, the difference between an OPA and NOPA is, that in a NOPA the signal and pump beam propagate with an angle α to each other in the nonlinear crystal, resulting in broadband phase-matching, first suggested by Gale et al. [89]. The propagation direction of the idler is at an angle Ω with respect to the signal. The phase-matching condition now is a vector equation and can be split into a parallel and perpendicular projection to the signal wave vector [17]:

$$\Delta k_{\parallel} = k_p \cos \alpha - k_s - k_i \cos \Omega = 0 \quad (1.54)$$

$$\Delta k_{\perp} = k_p \sin \alpha - k_i \sin \Omega = 0. \quad (1.55)$$

A changed signal frequency by $\Delta\omega$ also changes the idler frequency by $\Delta\omega$ with the opposite sign. A first order approximation of the wave vector mismatch along the two directions, which both have to vanish in order to obtain broadband phase-matching, can be represented as:

$$\Delta k_{\parallel} \cong -\frac{\partial k_s}{\partial \omega_s} \Delta\omega + \frac{\partial k_i}{\partial \omega_i} \cos \Omega \Delta\omega - k_i \sin \Omega \frac{\partial \Omega}{\partial \omega_i} \Delta\omega = 0 \quad (1.56)$$

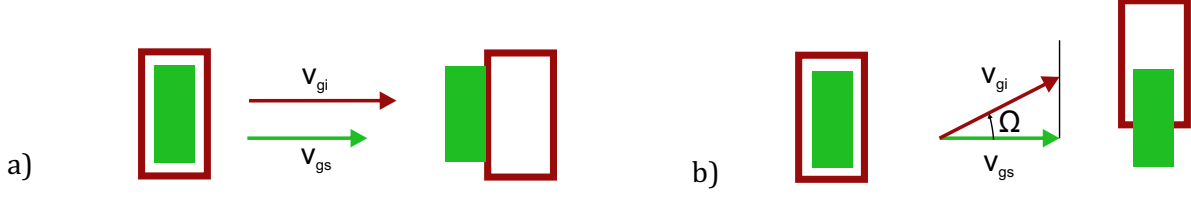


Figure 1.4: a) In a collinear OPA, the signal and idler soon lose temporal overlap, due to different group velocities. b) The noncollinear setup permits temporal overlap over the whole time of spatial overlap, resulting in an increased amplified bandwidth.

$$\Delta k_{\perp} \cong -\frac{\partial k_i}{\partial \omega_i} \sin \Omega \Delta \omega + k_i \cos \Omega \frac{\partial \Omega}{\partial \omega_i} \Delta \omega = 0 \quad (1.57)$$

From these two equations, it can be shown, that in case of phase-matching, the group velocity of the signal (ν_{gs}) and the idler (ν_{gi}) are related to each other by the signal-idler angle Ω to

$$\nu_{gs} = \nu_{gi} \cos \Omega. \quad (1.58)$$

This means, that the projection of ν_{gi} onto ν_{gs} can match the group velocity of the signal, when $\nu_{gi} > \nu_{gs}$, which is true in case of a type I phase-matching negative uniaxial crystals (*e. g.* BBO), and thus, allows for an effective overlap within the crystal, compare with figure 1.4.

Related to Ω and for the user more practical is the angle α , describing the noncollinearity of the signal and pump in the nonlinear crystal, which is given by

$$\alpha = \arcsin \left(\frac{1 - \nu_{gs}^2 / \nu_{gi}^2}{1 + 2\nu_{gs}n_s\lambda_i / \nu_{gi}n_i\lambda_s + n_s^2\lambda_i^2 / n_i^2\lambda_s^2} \right)^{1/2}. \quad (1.59)$$

Cerullo et al. [17] calculated the phase-matching angle θ_m as a function of signal wavelength for different pump-signal angles, for a pump wavelength of 400 nm and at a signal at 600 nm in a type I BBO, see figure 1.5. This plot visualizes the advantage over a noncollinear OPA over an collinear version. For latter, $\alpha = 0^\circ$ and the phase-matching angle shows a strong dependence on the wavelength, leading to a small amplified bandwidth. In contrast, with $\alpha = 3.7^\circ$, phase-matching is achieved over a range of 500 nm to 750 nm at $\theta_m = 31.3^\circ$ (for a pump beam, perpendicular to the crystal's surface), yielding a broadband amplification.

Since the signal is strongly linear chirped, due to the supercontinuum generation (compare section 1.2.6), the amplified bandwidth also depends on the pulse durations of the pump and signal pulses. Figure 1.5 illustrates this. When the pump is equal in duration to the signal, the full bandwidth is amplified and pulses of around 10 femtos can be achieved in the visible after recompression [90]. On the other hand, in case of a shorter pump pulse, the pump acts as a temporal gating and only a fraction of the signal bandwidth is amplified, allowing an signal photon energy selective output [91]. When the signal pulse is delayed with respect to the pump pulse, the pump amplifies different instantaneous frequencies and

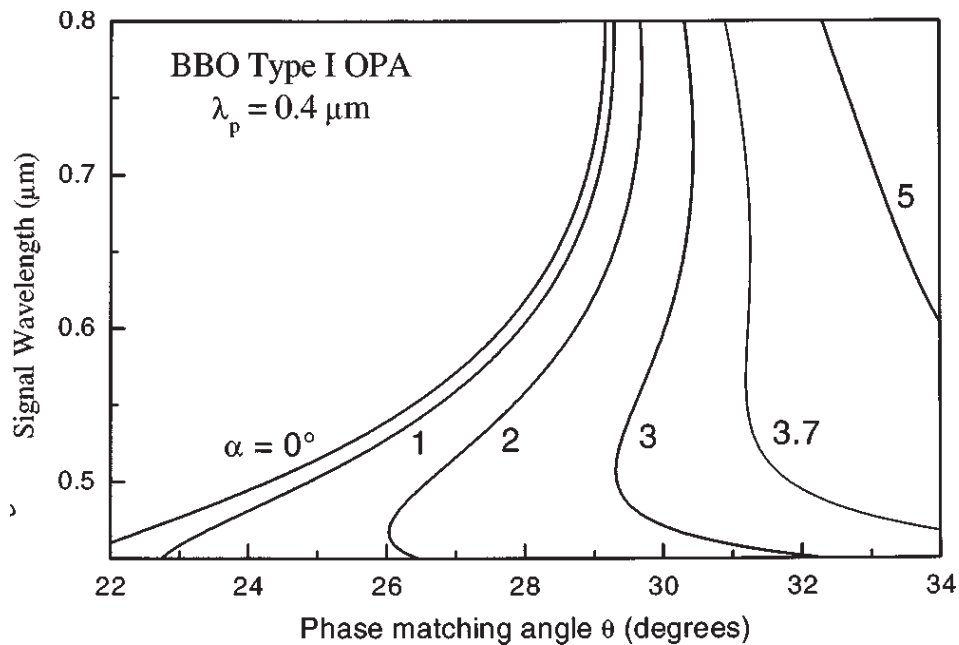


Figure 1.5: Phase-matching curves for different pump-signal angles α as a function of wavelength for a type I BBO pumped with 400 nm, figure adopted from [17].

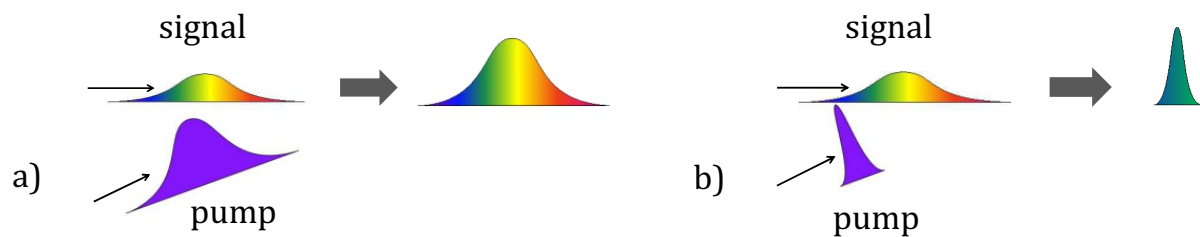


Figure 1.6: a) NOPA with an equivalent pulse duration of the signal and pump. This yields an amplification of a broad bandwidth, which in turn can be compressed to a few tens of femtoseconds. b) A NOPA with a shorter pump pulse than signal pulse. Here the pump acts as a narrow temporal gate for the amplified spectrum, since the signal pulse is chirped and thus changes its instantaneous frequency with time. The result is a narrowband pulse, which is more wavelength selective but not as compressible in time as a fully amplified bandwidth. Delaying the signal with respect to the pulse offers the possibility of a tunable output.

thus, a wavelength-tunable amplifier can be built. An illustration of this is depicted in figure 1.6.

1.2.6 Supercontinuum Generation

OPA and NOPA use a broadband seed beam which is amplified in the nonlinear crystal. In this section, the generation of such a beam will be discussed. Is a ultrashort pulse focused into a dispersive material *e. g.* sapphire, then its spectrum is extremely broadened and was first discovered by Alfano and Shapiro [18]. This effect is referred as supercontinuum generation (SCG). Since many experiments use laser pulses in the near infrared regime, the broadened spectrum can cover almost the whole visible spectrum, looking whitish on a screen, it is also known as white light generation.

The origin of SCG is a intensity dependent refractive index and the rapidly changing intensity of ultrashort laser pulses. In case of high intensities, the refractive index $n^2 = 1 + \chi^{(L)}$ with the linear susceptibility χ^L needs to be extended by nonlinear factors χ^{NL} (compare equation 1.21) to

$$n = \sqrt{1 + \chi^L + \chi^{NL}} = n_0 + n_2 I. \quad (1.60)$$

As can be seen, the refractive index is a sum of the linear refractive index n_0 and a intensity I induced nonlinear term n_2 . This nonlinear term also leads to nonlinear phase shifts ϕ^{NL} . Inserting this into equation 1.12 the instantaneous frequency $\omega_{\text{inst}}(t)$ at position z within the medium is

$$\omega_{\text{inst}}(t) = \omega_0 - n_2 \frac{\omega_0}{c} z \frac{\partial I(t)}{\partial t}. \quad (1.61)$$

Where c is the speed of light and a Gaussian plane wave was assumed. This equation can be interpreted, that the time dependent change in intensity in a dispersive medium generates new frequencies around the central frequency ω_0 . This phenomena is also called *self-phase modulation* and a more general expression than SCG.

Since the sign of the phase changes from the rising to the falling slope of the intensity profile, frequencies higher, as well as lower compared to ω_0 are generated. The leading edge of the pulse is responsible for lower frequencies and the trailing one for higher frequencies [19]. Another consequence from this is, that the spectral broadened pulse is strongly linear chirped and broadened in time.

The new generated frequencies are not symmetrically distributed around ω_0 , but are in majority of higher frequencies. The group velocity v_{group} is also intensity dependent:

$$v_{\text{group}} = \frac{c}{n(I) + \omega \frac{\partial n(I)}{\partial \omega}}. \quad (1.62)$$

From this equation it follows, that the peak intensity of the pulse has a lower group velocity than its wings. As a result, the main intensity shifts to the back of the pulse, leading to less pronounced change in intensity over time for the leading edge compared to the trailing edge, also called *self-steepening*. Hence, the pulse experiences a blue shift, because of the trailing edge, which now overweights in the nonlinear process.

1.3 High Harmonics Generation

Despite the early observation of low-order harmonics such as the SHG after the invention of the laser, higher-order harmonics were first discovered in 1987. The first published spectrum by McPherson *et al.* [20] already shows the typical properties, which include, that higher-order harmonics do not show a strong drop in intensity with increasing multiplicity of the harmonic, as it would be the case for the perturbative regime as discussed in section 1.2.1, but show an almost plateau like strength until a certain order, where the intensity drastically drops again. Another characteristic is the occurrence of just odd harmonics. McPherson *et al.* used a 248 nm laser, focused in Neon. This thesis is restricted on the work and discussion of the generation in rare gases, which is the mostly applied approach.

1.3.1 Three-Step Model of Ultrashort Pulses Interacting with a Gaseous Medium in the Strong Field Regime

The generation of low-order harmonics can be explained with a perturbation theory as done in section 1.2.1, but not the properties of high-order harmonics. In perturbation theory, a simultaneous absorption of N photons, leading to ionization is assumed. But the expected intensity I dependent ionization rates of I^N could not be confirmed experimentally. High harmonics occur, when the electric field of the driving laser is in the order of 10^{10} V/m. For this large field amplitudes, which strongly distort the Coulomb potential of the nuclei felt by electrons, Keldysh developed a strong field ionization theory, suggesting tunnel ionization [21]. This framework is able to predict the observed exponential dependency of the ionization rate as a function of laser intensity.

Even though these regimes can not be separated by a hard line, the *Keldysh parameter* γ was introduced to distinguish between them. It depends on the ionization potential I_P of the atom and the laser field and is defined as:

$$\gamma = \sqrt{\frac{I_P}{2U_P}} \quad (1.63)$$

where U_P is the ponderomotive potential, given by

$$U_P = \frac{e^2 E_0^2}{4m\omega^2} \quad (1.64)$$

which is a function of the maximum amplitude of the electric field E_0 , its frequency ω and the mass m and charge e of an electron. The ponderomotive potential is the classical kinetic energy of a free electron in an electromagnetic field, averaged over one cycle. For $\gamma > 1$ ionization results as multiphoton absorption as predicted in the perturbative theory. Tunnel ionization and thus the dominant process for HHG, occurs for $\gamma < 1$. A very low Keldysh parameter ($\gamma \ll 1$) results in below the ionization potential suppressed Coulomb potential, leading to above-barrier ionization.

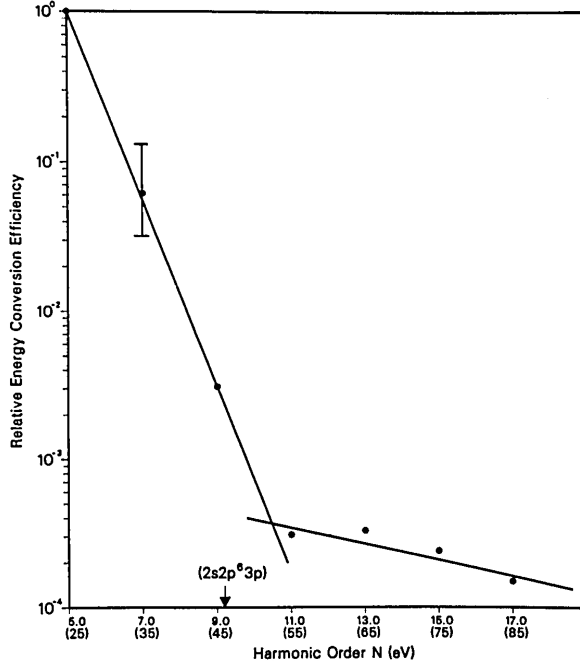


Figure 1.7: First Measured HHG Spectrum by [20], showing a plateau-like intensity for different high-order harmonics, after a rapid decrease for low-order harmonics.

The process of HHG can be explained by a semi-classical model, introduced by Corkum [22] and is called the *three-step model*. It includes the ionization of the atom via tunnel ionization, the acceleration of the free electron in the laser field and its possible recombination with the parent ion, releasing the excess energy in a high energetic photon. These processes are schematically depicted in figure 1.8. A more detailed discussion of each step follows now. A quantum mechanical treatment, the *strong field approximation*, introduced by Lewenstein et al. can be found in reference [23].

Ionization

In the case of a strong electric field acting on an atom, the combination of the attractive force of the nuclei and the external field can form a finite barrier for an electron, through which it can tunnel into vacuum state. As usual in tunneling processes, the probability can be in terms of tunneling times τ_t , giving a different definition of the Keldysh parameter [25]:

$$\gamma = 4\pi \frac{\tau_t}{T} \quad (1.65)$$

with T being the time for one cycle of the optical field. Successful tunneling requires a quasi-static external field in the frame of the tunneling electron, which means $\tau_t \ll T$. When the laser frequency is too high, meaning higher than the atomic-orbital frequency, the potential is faster modulated than the electron needs to tunnel through the barrier and tunnel ionization is no longer possible.

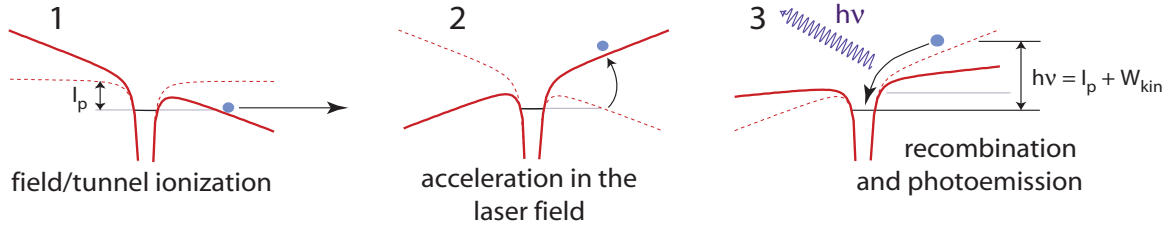


Figure 1.8: In the first step of the three-step model, the Coulomb potential seen by an electron from the nucleus, gets strongly deformed, building a finite potential barrier, through which the electron can tunnel. In step two, the emitted electron is accelerated by the driving laser field. Due to the periodic oscillation, the direction of the field changes and the electron is back-accelerated. Thus, in step three, it can recombine with the parent ion and emit an high energetic photon, carrying the energy of the ionization potential and the gained kinetic energy of the electron during the excursion. Figure taken from [24].

A theoretical model to estimate these tunnel ionization rates is the ADK model [26], but it will be just left here as a comment.

Acceleration and Electron Trajectories

In the three-step model, the electron propagation is considered to follow classical mechanic laws. Furthermore, the initial velocity of the electron at the time of ionization t_i is assumed to be zero and its position is defined as zero as well. Only the electric field of the laser is considered to act on the electron, the magnetic field and any influences from the ion are neglected. With a linear polarized light field $E(t) = E_0 \sin(\omega t)$ at frequency ω , the force experienced by the electron is

$$F(t) = m\ddot{x}(t) = -eE(t) \quad (1.66)$$

where m and e again are the mass and charge of an electron, respectively. Hence, the electron's velocity and trajectory can be derived:

$$\ddot{x}(t) = -\frac{eE_0}{m} \sin(\omega t) \quad (1.67)$$

$$\dot{x}(t) = \frac{eE_0}{m\omega} [\cos(\omega t) - \cos(\omega t_i)] \quad (1.68)$$

$$x(t) = \frac{eE_0}{m\omega^2} [\sin(\omega t) - \sin(\omega t_i) - \omega(t - t_i) \cos(\omega t_i)]. \quad (1.69)$$

The energy which an electron gains in the driving laser field, given by the ponderomotive potential, depends on the initial phase of the electric field $\omega t_i + \phi$ at the time of its tunneling into the continuum. Trajectories for different initial phases experience a different acceleration due to the driving laser field. There are some trajectories, where electrons

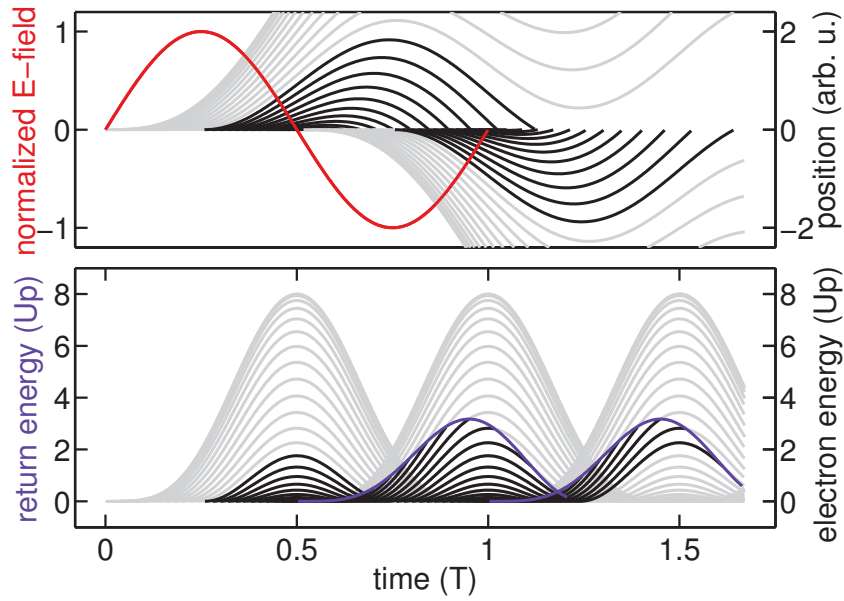


Figure 1.9: *Top)* Shown are different electron trajectories as a function of tunneling time with respect to the phase of the driving electric field. In red, one cycle of the driving electric field is plotted. The gray lines correspond to electron trajectories which gain so much energy, that no recombination can take place anymore. In contrast, the black curves can recombine. *Bottom)* Each trajectory corresponds with a certain ponderomotive energy. The one with the highest energy is plotted in blue. This trajectory determines the cut-off energy for a given rare gas. All other energies can be achieved by a short and a long trajectory. Figure taken from [27].

experience such a strong acceleration, that no return to the parent ion is possible², while other lead to a trace back to the ion. There is one phase, where the electron gains the highest energy, whilst still being back-accelerated with the possibility to recombine. Electrons from this trajectory contribute to the high harmonics with the highest photon energy, named the cut-off energy. For all other energies, below the cut-off, there are two possible trajectories. One, called the short trajectory, because its traveling time is short, and the other one is the long trajectory with a longer traveling time.

Recombination

When the initial phase of the laser field at the time of ionization allows for a return of the electron to the ion, then there is the possibility of recombining. In this step, a photon is emitted which carries the energy corresponding to the ionization potential I_p in case the electron was at rest. Did the electron gain kinetic energy in the driving field, then the photon's energy is increased by that amount, leading to high-order harmonic photons. An upper value of the photon energy is set by the trajectory that allows for gaining the most kinetic energy while still being able to recombine. This is the so called cut-off energy:

$$E_{cutoff} = I_p + 3.17U_p. \quad (1.70)$$

Since electrons tunnel and recombine each half cycle, the high harmonics pulse consists of a train of very short single attosecond pulses.

1.3.2 Wavelength Scaling

In the previous section, the electron trajectory was treated in a classic mechanical manner. However, in a quantum mechanical model the electron's wave function also spreads transversely due to quantum diffusion, leading to a drastic reduction in recombination probability and thus in HHG yield [28]. As shown in figure 1.10, the total spatial spread of the wave function depends on the wavelength of the driving field. A longer wavelength coincides with a longer cycle in time. The electron is accelerated within one half cycle of the driving field, until it changes its sign and accelerates the electron in the opposite direction. The longer one half cycle is, the longer the excursion and thus the greater the quantum diffusion of the electron wave function will be. Hence, an efficient single-atom response and thus HHG, the wavelength of the driving field should be minimized. This makes the short trajectory to be more preferred to the long trajectory. Indeed, in the work presented in [29] a more efficient HHG was found for the short trajectory. The referred work was done for Keldysh parameters close to unity and single-atom response scaling with the wavelength of $\lambda^{4.7 \pm 1}$ was found for the short trajectory and driving fields in the visible regime.

²At least in this model, where back scattering effects are neglected.

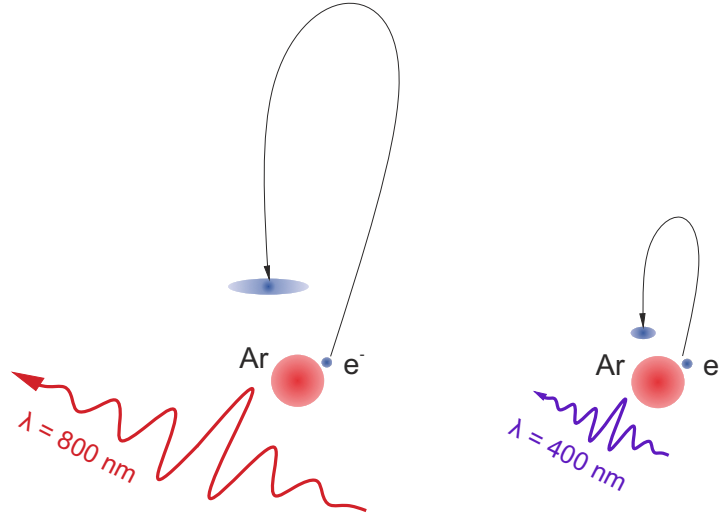


Figure 1.10: The electron's wave function spreads spatially when being in the continuum due to quantum diffusion. This reduces the probability of recombining with the parent ion. Thus, the traveling time of the electron should be minimized. A shorter wavelength of the driving field can achieve this, because the electric field oscillates more rapidly and the electron is back-accelerated in a shorter time. Schematically shown are the electron trajectories emitted from an ionized argon atom by a 800 nm (left) and 400 nm (right) laser field.

In combination with highest HHG photon energy that is required for an experiment, a guideline for an optimized driving laser frequency can be given. Since the cut-off energy (equation 1.70) depends on the ponderomotive potential (equation 1.64) the maximum HHG photon energy scales with $\sim \lambda^2$, this sets a lower limit for the wavelength. For the case of 22 eV XUV photons, we are aiming at, the λ scaling was experimentally proven by Wang et al. [30], comparing a driving wavelength of 390 nm with 780 nm.

1.3.3 Phase-Matching

The overall yield in high harmonics is not just a function of the quantum mechanical single-atom efficiency, but a coherent summation of many emitting atoms. In order to enable a constructive summation, all emitters must be in phase and thus, the driving field and the harmonic need to be phase-matched into the whole interaction volume of the laser with the noble gas atoms. This however, can only be partly achieved, due to several effects, such as the wavelength dependency of the refractive index, leading to different phase accumulations for the driving and harmonic wave. The high intensities of $10 \times 10^{14} \text{ W/cm}^2$ which are necessary for HHG result in a partial ionization of the interaction atoms. Those free electrons cause plasma dispersion, which is again different for the harmonic and the driving field. Such high intensities in general require focusing of the driving beam, altering the phase spatially. Another contributor is the single-atom phase. These effects shall be discussed now.

Neutral Dispersion

The dispersion experienced by a wave depends in gas on several conditions, such as the element of the gas, its pressure, the wave's wavelength and the regimes of HHG, also on the intensity of the laser.

The phase shift $d\varphi$ of a electromagnetic wave with frequency ω propagating a distance dz through a medium of refractive index n is

$$d\varphi = \frac{n\omega}{c_0} dz, \quad (1.71)$$

with c_0 being the vacuum speed of light. The different phase shift for the driving field and the harmonic of H th order resulting from normal dispersion thus is

$$d\varphi_n = (n_{Dn}(z, t) - n_{Hn}(z, t)) \frac{H\omega}{c_0} dz. \quad (1.72)$$

Here, n_{Dn} and n_{Hn} are the corresponding neutral refractive indices for the driving and the harmonic field, respectively. Due to inhomogeneities in the gas density and intensity dependent values of the refractive index, n is a function of space and time. Integrating equation 1.72 over a distance $z - z_0$ yields the total phase-mismatch:

$$\Delta\varphi_n = \frac{H\omega}{c_0} \int_{z_0}^z (n_{Dn}(z', t) - n_{Hn}(z', t)) dz'. \quad (1.73)$$

Plasma Dispersion

As a consequence of the intense driving laser, free electrons are generated which contribute negatively to the refractive index. Since the density of free electrons depends on the laser intensity, plasma dispersion is a function of time. But recombination occurs in a much larger time scale than the interaction of the femtosecond laser pulse, thus it does reduce after the peak intensity has passed. When the free electron density N_e exceeds a critical density N_c , the refractive index decreases to zero and phase-matching is no longer possible. The index of refraction can be expressed as [31]:

$$n(z, t) = \sqrt{1 - \frac{N_e(z, t)}{N_c}}. \quad (1.74)$$

$N_c = \epsilon_0 m \omega^2 / e^2$ defines the critical density, at which plasma frequency and laser frequency are equal, resulting in a complete absorption of electromagnetic waves with this frequency. The phase-mismatch $\Delta\varphi_p$ for driving and harmonic phase can be calculated similar to the neutral dispersion:

$$\Delta\varphi_p = \frac{H\omega}{c_0} \int_{z_0}^z (n_{Dp}(z', t) - n_{Hp}(z', t)) dz', \quad (1.75)$$

Geometrical Phase

As a consequence of focusing the driving laser, the wavefront is bent and an additional off-axis phase shift is induced compared to a plane wave. For a Gaussian beam, the corresponding phase along the spatial cylindrical coordinates r and z is [32]:

$$\varphi(r, z) = kz - \xi(z) + \frac{kr^2}{2R(z)} \quad (1.76)$$

where k is the wave number, $R(z)$ the radius of curvature of the wavefront and $\xi(z)$ the *Gouy phase* [33]. It is given as

$$\xi(z) = \tan^{-1} \left(\frac{z}{z_0} \right), \quad (1.77)$$

with $z_0 = \pi w_0^2 / \lambda$ being the Rayleigh length of a Gaussian beam.

The different phase shift for driving field and harmonic field of H th order, that arises from focusing thus can be expressed as [34]:

$$\Delta\varphi_g(r, z) = (H - 1) \left(\frac{kr^2}{2R(z)} - \xi(z) \right). \quad (1.78)$$

Thus, the variation of the harmonic is H times larger than for the driving field. In total, the geometrical phase undergoes a shift of π when propagating from $-\infty$ to ∞ .

Single-Atom Phase

The single-atom phase is the phase shift that a harmonic of order H acquires as a sum of the phase of the electron wave function while being in the continuum and the delay with respect to the reference phase (driving laser field), because of its excursion into the continuum.

It can be shown, that the phase term that results from the continuum is [35]:

$$\varphi_a = -\frac{1}{\hbar} S(p, t_i, t_r) \quad (1.79)$$

with the quasi-classical action S , being

$$S_H^k(p, t_i, t_r) = \int_{t_i}^{t_r} \left(\frac{p(t, k, H)^2}{2m} + I_P \right) dt. \quad (1.80)$$

Here, I_P is the ionization potential of the atom, p the classical momentum, m the electron mass, t_i and t_r the tunneling time and the return time, respectively. The action integral also depends on the harmonic order H and the trajectory k , which can be the short or long trajectory.

The phase-mismatch then is:

$$\Delta\varphi_a = H\omega t_r - \frac{1}{\hbar} S_H^k(p, t_i, t_r) \quad (1.81)$$

and can be approximated by the linear equation

$$\Delta\varphi_a \approx \alpha_H^k I, \quad (1.82)$$

where α_H^k is a trajectory and harmonic order dependent coefficient. This coefficient is almost independent of the intensity for the short trajectory, in contrast to the long trajectory [27].

Total Phase

In summary, the total acquired phase-mismatch is:

$$\Delta\varphi_{tot} = \Delta\varphi_n + \Delta\varphi_p + \Delta\varphi_g + \Delta\varphi_a. \quad (1.83)$$

While the normal dispersion leads to a retardation of the driving phase compared to the harmonic phase, due to a refractive index below unity in the XUV regime, the opposite is the case for the plasma dispersion. In case of the geometric phase, the fundamental's phase travels faster, because the beam is more divergent compared to the harmonic beam and thus, the wavefronts are more curved, leading to faster traveling along the optical axis. The contribution of the atomic phase depends on the trajectory.

The total phase-mismatch $\Delta\varphi_{tot}$ should be zero over the whole HHG volume for a maximum yield. In reality, this is not possible, since a Gaussian beam profile alters the refractive index and free electron generation differently on the optical axis compared to the less intense parts. Therefore, it is convenient to at least optimize the phase-matching along the optical axis (z direction). A on axis k-vector mismatch can be defined as [27]:

$$\Delta k = Hk(\omega) - k(H\omega) = \frac{H\omega}{c_D} - \frac{H\omega}{c_H} = \frac{d\Delta\varphi}{dz}, \quad (1.84)$$

with the driving laser (c_D) and harmonic (c_H) phase velocity, respectively. Table 1.1, adopted from [27, 36] summarizes the different phase contributions.

Phase Term	Neutral	Plasma	Geometric	Atomic
Sign	+	-	-	-sign(z)
Dependencies	H	$I(t), H$	focusing, H	$H, I(t), \text{traj.}$

Table 1.1: Signs and dependencies of the different phase terms.

1.3.4 High Harmonics Spectrum

Some spectral features of a typical HHG spectrum were already introduced, being the harmonic plateau, or the cut-off harmonic, which follows equation 1.70. Another characteristic is, that only odd multiples of the driving frequency occur. A possible explanation of this is hidden in the inversion symmetry of noble gases. In such a medium, all properties must

be parity invariant, which means (when comparing with equation 1.21) $\chi^{(n)}(\vec{r}) = \chi^{(n)}(-\vec{r})$. Since the polarization vector and the electric field vector are polar vectors (odd parity), no even contributor is allowed. In combination that the n^{th} order of the electric field is proportional with the n^{th} multiple of the fundamental frequency ω , only odd multiples can be generated³, and the harmonics are separated from each other by 2ω .

In general, the shorter the pulse duration of the driving pulse is, the broader is its spectrum, which in turn supports broader high harmonic spectra. The actual spectrum can differ from the expected one, because certain effects cause a blue-shift and a broadening of the harmonic peaks. Some of the phase effects from the earlier section are time dependent. These time dependent phases generate additional frequencies, that lead to a broadening of the spectrum and a shift of the instantaneous frequency with respect to the central frequency ω_0

$$\omega(t) = \frac{d\varphi(t)}{dt} = \omega_0 + \delta\omega. \quad (1.85)$$

As already described in section 1.2.6, self-steepening of the pulse leads to a higher weightage of higher frequencies and thus a blue-shift.

A manipulation of the bandwidth towards a narrower bandwidth, can be obtained, when the driving laser pulse is stretched in time, resulting in more laser cycles that contribute to the HHG [37]. According to Fourier's theorem, more equally separated events in the time domain are coupled with a narrowing spectrum in the frequency domain. Of course this only holds true, as long as the stretched pulse still supports the intensity, which is required for the generation of the desired harmonic order.

1.3.5 Interaction Gas

[38] The type of noble gas that interacts with the driving laser has an influence on the generated high harmonics. The first ionization potential I_P for example determines the necessary intensity, at which the HHG is the most efficient. A lower I_P requires less intense driving laser fields, but at the same time, the critical ionization density (compare equation 1.74) is more easily reached, limiting the maximal applied field amplitude and thus the maximum accessible high harmonics photon energy. To achieve very high harmonic orders, lighter noble gases, which have a higher ionization potential are required, coming along with the need for very high intensities though.

Another quantity is the dipole polarizability $\alpha_{dip}(\omega)$. With increasing mass of the atom, $\alpha_{dip}(\omega)$ increases, which should yield higher conversion efficiencies [27]. In case of a driving laser frequency in the visible regime, $\alpha_{dip}(\omega)$ can be well approximated by the static polarizability α_{dip} [39].

Table 1.2 lists these properties for the elements of the noble gas group, with data taken from [38].

³As long as inversion symmetry is not broken

	He	Ne	Ar	Kr	Xe
I_P [eV]	24.6	21.6	15.8	14.0	12.1
α_{dip} [1.6488×10^{-41} Cm ² /V]	1.38	2.67	11.1	16.8	26.7

Table 1.2: First ionization potential and static dipole polarizabilities for different noble gases.

As can be seen in the table, the ionization potentials are in the regime of typical XUV photon energies. If the I_P is lower than the photon energy, the gas can reabsorb the XUV. This has to be considered when high gas densities are reached. Even in the case of a perfectly phase-matched HHG, reabsorption can be dominant and no high harmonics will be detected. In order to avoid this, not just the gas density in the interaction volume must be below a critical density, also the whole load to the vacuum beamline should be minimized.

1.3.6 High Harmonics Generation at High-Repetition Rates

High-repetition rate laser systems suffer from the drawback of a low pulse energy, making it harder to achieve the necessary intensities to drive HHG with enough coherent emitters for a strong high harmonics yield. To compensate for this, very small foci are needed. This in turn leads to a strong, negative phase contribution around the focus, arising from the geometrical phase term.

Heyl et al. [40] demonstrated in simulations, that the phase linked to neutral dispersion can be compensated for the negative phase of the geometrical and plasma terms. Hence, phase-matching should be possible for tight focusing conditions, provided that the short trajectory favored in HHG process, since it supports the neutral dispersion phase, in contrast to the long trajectory, contributing to the phase with a negative sign. Since the effect of the dispersion scales linear with the density and thus the pressure of the gas medium, high gas pressures in the interaction volume are needed for phase-matching with a tight focus. Further studies, done by Rothhardt et al [41], investigated the scaling of main physical quantities of HHG and limiting effects such as dephasing, absorption and plasma defocusing with respect to the focal spot diameter. Their results revealed, that these effects are invariant of the focal conditions along the optical axis and small off-axis angles. As conclusion, the same HHG efficiency should be achieved with tight focusing compared to loose focusing. But the interaction volume needs to be smaller for tight focusing, because the geometric phase leads to a shortened coherence length $l_c = \pi/\Delta k_{tot}$ (with Δk_{tot} being the total phase-mismatch of driving and harmonic field). To avoid running into absorption limitation, l_c should exceed the absorption length l_{abs} ($l_{abs} = 1/\sigma\rho$ with σ being the absorption cross-section and ρ the gas density) by a factor of five [42].

In summary, in the tight focus regime, HHG can be generated with equal conversion efficiencies as in loose focusing, a very dense gas target provided.

Chapter 2

Generation of High-Repetition Rate XUV Pulses

The main experimental scope for this thesis was to establish a high-repetition rate HHG source and beamline, suitable for trARPES experiments in the full first Brillouin zone. As already mentioned in the introduction, a special laser system with a high-repetition rate for the sake of a fast data acquisition and low space charge-effects was designed. On the other side, a high-repetition rate comes along with a low pulse energy. To compensate this for an efficient HHG, tight focusing is needed [41]. Therefore, high noble gas densities, equivalent to high backing pressures, are needed to fulfill phase-matching. This is in conflict with photoelectron spectroscopy which requires ultra-high vacuum (UHV) for an uncontaminated sample and no scattering of the photoelectrons. This is a challenge for the gas supply system and vacuum pumping system. Furthermore, ARPES experiments require a monochromatic light source, which is not intrinsically provided by the high-harmonics spectrum. These challenges are faced by frequency doubling of the laser before it drives the HHG. Despite the loss in power, the higher photon energy of the fundamental pulse leads to better single-atom response, which should even increase the conversion efficiency into high-harmonic photons [30]. This also allows for a wider range of spectral filtering techniques due to the 2ω spacing between the harmonics, and thus, enabling us an isolation of a single harmonic without much distortion of the XUV beam and at the same time simplifies the differential pumping line.

In this chapter, first the laser setup will be introduced, then the considerations and technical approaches for the HHG source are described, including the gas and vacuum system, as well as the spectral filtering. It follows a characterization of the XUV light source. This includes its spectral, temporal, spatial and photon flux properties, as well as its dependence on different parameter such as backing pressure, input power and the gas target.

2.1 Laser Setup and Beamline

The laser system was specially designed to meet the requirements, being high harmonics generation at a high repetition rate of 500 kHz and a monochromatized harmonics photon energy exceeding 20 eV, as already mentioned in the preface. High intensities are needed for the process of tunnel ionization, which so far was mainly accessed by Ti:sapphire laser systems [43]. A technological bottleneck represent the relative low repetition rates of a few kHz of such systems. When pushing these systems to higher repetition rates, *e. g.* with regenerative amplifiers [40, 44] in the range of 100 kHz, they quickly drop in pulse energy below a level where high harmonics can be generated without great effort. Even though it could be shown that HHG in gaseous mediums work up into the MHz regime [45, 46], generated with a fiber laser system. The development of high power amplifiers based on Yb:YAG with an output exceeding 1 kW [47] paved the way for another new technological approaches.

Our approach is a ytterbium based master oscillator fiber amplifier (MOFA) operating at 500 kHz that seeds both, a white-light supercontinuum and a Yb:YAG InnoSlab amplifier with short path length. After a frequency doubling stage of the pump, both beam run a non-collinear OPCPA from which a high power output with a scalable spectrum in the range between 680 nm and 900 nm, yielding the opportunity for a tunable driving laser and different applications. This setup will now be briefly described, a more detailed description can be found in Ref. [48].

A schematic sketch of the laser system is depicted in figure 2.1. A nonlinear polarization evolution mode-locked [50] Ytterbium fiber oscillator operating in all normal dispersive regime [51] runs at 25 MHz. The central wavelength is at 1030 nm with a FWHM bandwidth of 10 nm. After stretching the oscillator output to 130 ps, the pulses passes a dual-stage fiber amplifier with a selection of the repetition rate in between these two amplifiers, with a fiber-coupled acousto-optical modulator in a range of 0.3 to 1 MHz. Another amplification stage up to 9 W average power consists of a 80 cm long rod-type photonic crystal fiber. This output is split in a ratio of 60/40 where the latter one directly seeds a Yb:YAG InnoSlab amplifier (Amphos 200) which provides a 1.6 nm narrow band amplification up to 200 W at 1030 nm. This serves as the pump for the OPCPA after a compression down to 1.25 ps and frequency doubling in a 2 mm thick BBO to >80 W at 515 nm. The other 60% rod-type output is compressed to 360 fs and generates a stable white-light supercontinuum [52] in a 20 mm thick YAG crystal in a spectral range from 600 nm to 900 nm, for seeding the OPCPA.

The non-collinear OPCPA, which is described in section 1.2.5 consists of a 4 mm thick BBO crystal (type I, $\theta = 24.3^\circ$, internal angle 2.4°). This configuration allows a certain adjustability in terms of amplified central wavelength and bandwidth by changing the seed-pump time overlap or introducing more chirp in the seed by a changing the amount of dispersive material for the seed. Since the pump pulse is much shorter in time, it acts as a temporal gating for the amplified seed spectrum.

We use a central wavelength of around 795 nm and obtain 24 W average power in the signal.

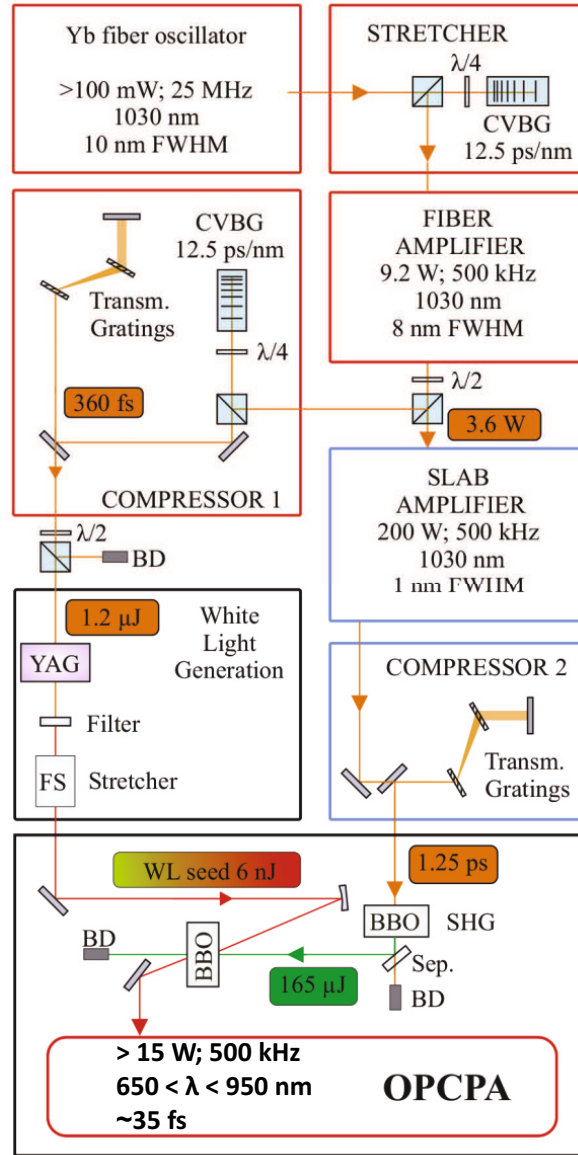


Figure 2.1: Laser layout: CVBG = Chirped Volume Bragg Grating, FS = Fused Silica, BD = Beam Dump, Sep. = Wavelength Separator, SHG = Second Harmonic Generation. Figure adopted from [48]

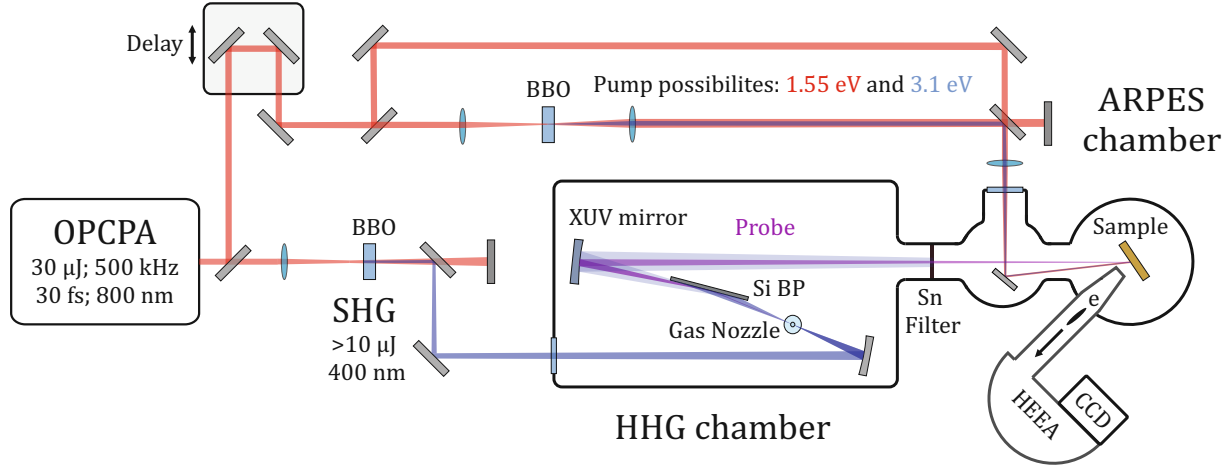


Figure 2.2: Schematic beam line of the pump/probe trARPES experiment. After the OPCA, the beam is separated into a pump and a probe arm. First one can be delayed with respect to the probe pulse for time-scanning. A BBO crystal allows for SHG of the pump when needed. The probe pulse is as well doubled in frequency, before it enters the vacuum chamber where the XUV are generated in a rare gas jet. After monochromatization, of the XUV probe pulse, both beam arms overlap almost collinearly on the sample in the UVH chamber, where the photoemitted electrons are detected with a hemispherical energy analyzer.

After a fused silica Brewster cut prism compressor sub-20 fs and >16 W average power are obtained.

This beam becomes separated by a beam splitter with 5% transmission which is used as the pump beam for the trARPES experiment and controlled in power via a combination of motorized waveplate and thin-film polarizers. To enable time-resolved ARPES, the pump beam can be delayed by a retro-reflector which is mounted on a motorized stage with a scanning range of 150 mm. Afterwards, the beam can be doubled in frequency in a 0.1 mm thick BBO, allowing for pump pulse photon energies of 1.55 eV or 3.1 eV. This beam is incoupled into the vacuum beamline and propagates close to collinearity with the probe pulse to the sample in the experimental chamber. A scheme of this setup is depicted in figure 2.2.

The main part remaining after the 95/5 beam splitter, can be regulated in intensity via a motorized achromatic $\lambda/2$ waveplate and is frequency doubled in a 100 μm thick type I BBO and angle of $\theta = 29.2^\circ$ for the sake of a higher single-atom response in the HHG process and a broader spacing between single harmonics, as outlined in section 1.3.2. The SHG output exceeds 5 W at a central wavelength of 400 nm and enters the vacuum part of the beamline where it drives the HHG.

The following part now will focus on the realization of the high harmonics generation with

this UV beam.

2.2 Experimental HHG Setup

The OPCPA system described above, is the starting point for the experimental part of this thesis, which was to establish a stable and monochromatized 7th order high-harmonic generation and to connect this XUV source with the ARPES experimental chamber. When beginning to work at this laboratory, the OPCPA was already in operation and just minor modifications were done there. The beam path ended in a vacuum chamber, further on named as *HHG chamber*, with a McPherson 234/302 Monochromator attached. In the following sections, considerations of the design and the technical realization of the HHG generation will be described.

2.2.1 HHG Chamber and Gas Target

XUV radiation is strongly absorbed in air [53], mainly consisting of molecular nitrogen and oxygen, therefore HHG must be done in vacuum with as less particles, such as air and water, as possible. The entrance window to the HHG chamber consists of a 1 mm thick CaF_2 to minimize dispersion. It is worth noticing that the BBO crystal for frequency doubling the compressed OPCPA output and therefore generating the driving pulse for the HHG process, first was placed inside the HHG chamber, but suffered from thermal laser induced damage very easily as soon as the chamber was evacuated. To solve this problem, the crystal was placed in front of the HHG chamber and there thermal air convection proved to be sufficient for a long term operation without any damage to the crystal.

Inside the chamber, schematically depicted in figure 2.3, the optical components are mounted on a breadboard, which in turn is placed on a vibration dumping material to reduce mechanical instabilities. To reach a sufficient high intensity for high-harmonics generation, the UV beam is tightly focused via a spherical dielectric mirror with a small curvature radius of $r = 200$ mm resulting in a focal length of $f = 100$ mm. In order to reduce optical aberrations and thus a distortion of the laser mode, which results in low high-harmonics generation efficiency [54], the angle of incidence on the focusing spherical mirror is chosen to be as small as possible withing the geometrical constrains.

Assuming a Gaussian beam profile, both in time and space, the peak intensity is [55]:

$$I_{0p} = \frac{1.88}{\pi} \frac{\varepsilon}{w^2 \tau} \quad (2.1)$$

Where ε is the pulse energy, w the $1/e^2$ radius of the beam size and τ is the FWHM pulse duration.

Measuring such a tightly focused beam is not trivial, since the spot size varies rapidly when the beam profiler is slightly misplaced along the beam path or a bit tilted or the very high intensities which are reached when measuring the profile at maximum power. Latter is

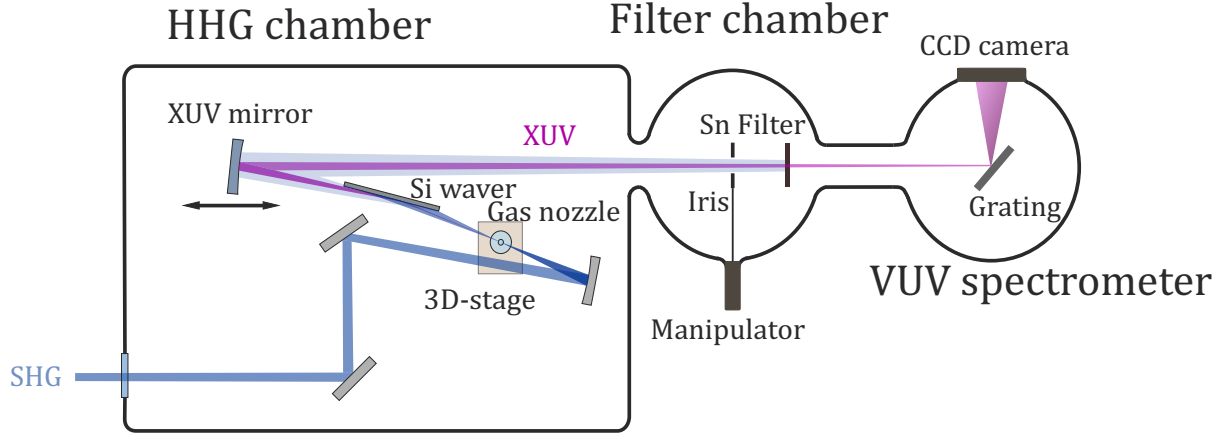


Figure 2.3: HHG chamber state for characterization of the high-harmonics, before the connection with the ARPES chamber. The essential elements are the gas target, for monochromatization of the spectrum the silicon wafer in Brewster's angle, the XUV mirror and the thin metal Filter. The harmonics are investigated with a VUV spectrometer.

needed, since the profile can be power depend because of the foregoing non-linear effects. Another difficulty is the bulkiness of the beam-profiler, either clipping the beam, or a greater angle of incidence on the focusing mirror has to be chosen, which in turn affects the spot profile. Our device, a Spiricon BGS-USB-SP620, has a pixel area of $4.4\text{ }\mu\text{m} \times 4.4\text{ }\mu\text{m}$ which is in the order of magnitude of the expected beam waist, thus not allowing for proper displayed profile. Taking advantage of the assumption of the beam waist scaling linearly with the focal length, $w_0 \sim f$, an easier to handle measurement was done with a $f = 250\text{ mm}$ lens, which is depicted in figure 2.4. This image shows a $D4\sigma$ spot size of $25 \times 29\text{ }\mu\text{m}^2$, implying $10 \times 12\text{ }\mu\text{m}^2$ as down scaled spot size for the $f = 100\text{ mm}$ mirror and an average $D4\sigma$ width of $11\text{ }\mu\text{m}$.

Concerning the pulse duration of the second harmonic, no FROG (frequency resolved optical gating) specified for this wavelength was available. To get an estimated pulse duration, a spectrum was taken, see figure 2.4, and the in section 1.1.3 outlined time-bandwidth product for a Gaussian pulse was used. Since the prism compressor of the fundamental beam is optimized for the SHG in the BBO an almost Fourier limited pulse duration is assumed for the second harmonic as simplification. The measured spectrum has a FWHM bandwidth of 7 nm which results in a Fourier limited FWHM pulse duration of 33.6 fs . Furthermore, this pulse propagates along the $100\text{ }\mu\text{m}$ thick BBO of the SHG and passes a 1 mm thick CaF_2 window. A duration of 33.9 fs can be estimated from the group-velocity dispersion (GVD) k_l'' for CaF_2 at 400 nm of $68\text{ fs}^2/\text{mm}$ [56] and $150\text{ fs}^2/\text{mm}$ for the extraordinary beam in the BBO [57], following the formula for a Gaussian pulse,

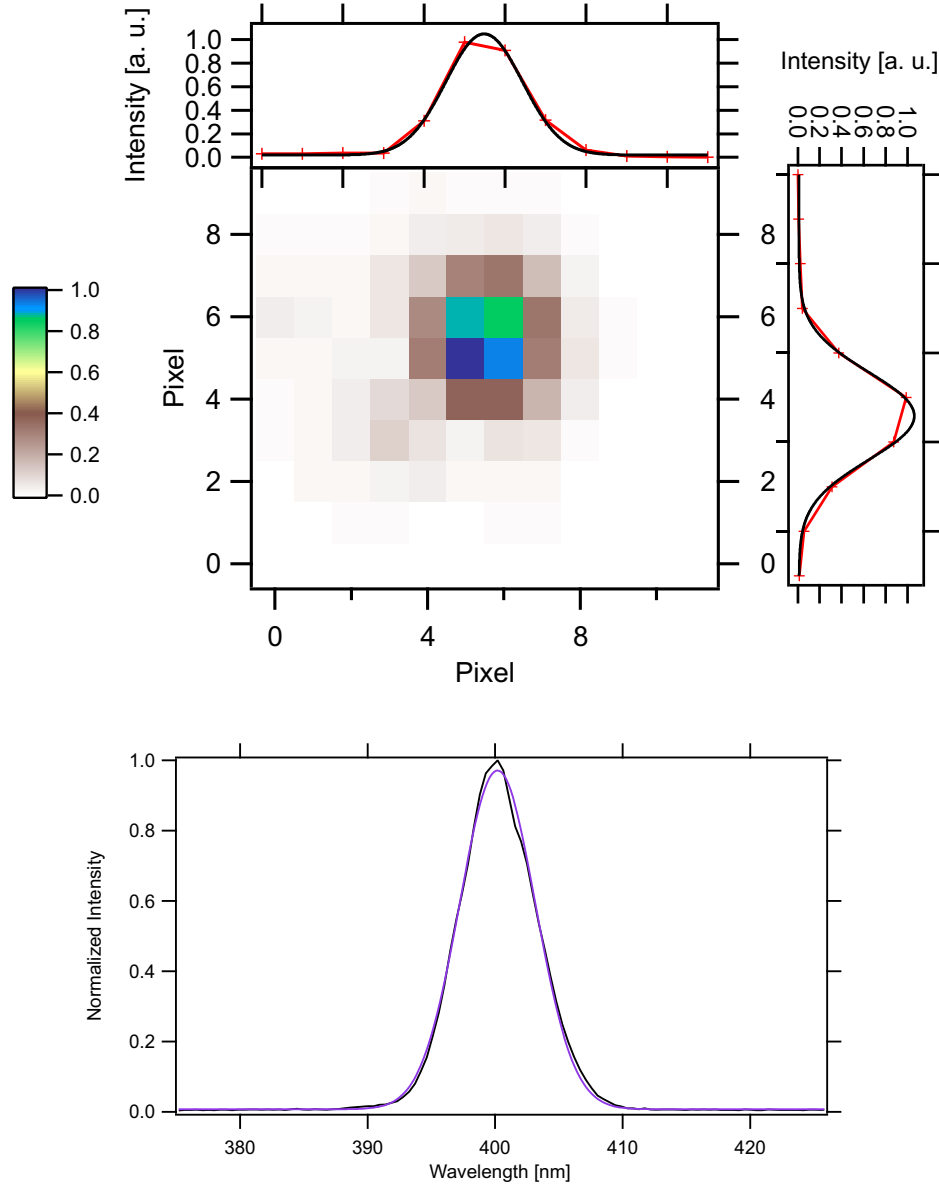


Figure 2.4: *Top*) SHG spot profile with a $f = 250$ mm lens for estimating the spot size of the SHG to $11\ \mu\text{m}$ for a $f = 100$ mm lens. See text for details. *Bottom*) The spectrum of the SHG beam reveals a FWHM bandwidth of 7 nm.

given by Diels [8]:

$$\tau_G(L) = \tau_{Gmin} \sqrt{1 + \left(\frac{2 |k_l''| L}{\tau_{Gmin}^2} \right)^2} \quad (2.2)$$

where L is the propagation length in the material and τ_{Gmin} the Fourier-limited FWHM duration.

With the aforementioned pulse properties, a peak intensity of $5.8 \times 10^{14} \text{ W/cm}^2$ results, being a bit higher than the target value of $1 \times 10^{14} \text{ W/cm}^2$, but a Keldysh parameter of $\gamma = 0.95$ (*cf.* section 1.3.1) states being in the main regime for efficient tunnel ionization. The real peak intensity even might be a bit lower, due to more dispersion from $\sim 200 \text{ mm}$ propagation in air and hitting on five dielectric mirrors, brining the achieved Keldysh parameter even closer to unity. The beam is able to ionize air or a noble gas jet. The latter streams out from a gas target which in turn is mounted on a three dimensional piezo-electrical stage with a minimum step size of about 1 nm . This allows for an precise positioning of the gas volume with respect to the laser focus to achieve the best possible phase-matching. The backing pressure in the supply line of the gas nozzle is controlled by a MKS Instruments compact pressure regulator with a maximum pressure supply of 6.9 bar .

The co-propagating UV and XUV beam now hit a silicon waver where they get separated. More on that in 2.2.3. Here, the reflected XUV part is used and finally focused by a spherical concave multilayer mirror with high reflectivity for 21.7 eV . The mirror is mounted on a motorized optical mirror mount, which allows a fine tuning of the beam pointing on the sample. Additionally, this assembly sits on a motorized translation stage, enabling a movement along the optical axis and thus a fine tuning of the focus position along this axis. Before the McPherson Monochromator there is an additional small vacuum chamber with an motorized aperture, sitting and on a three dimensional manipulator to adjust it relative to the XUV beam and for this reason can be used as variable attenuator or mode-cleaner. Furthermore, a filter wheel with a motorized rotation axis, which can house six metal filters, is also installed in this chamber.

The HHG chamber is pumped by a combination of an Edwards XDS35i scroll pump and a Pfeiffer Vacuum HiPace 700 turbopump. The filter chamber and the spectrometer are equipped with turbomolecular pump with 67 ls^{-1} and 260 ls^{-1} nominal pumping speed for N_2 , respectively.

So far, a beam suitable for driving HHG has been introduced. For the actual HHG, an interaction medium is needed. This is done in a rare gas jet, which technical challenges and realization will be addressed in the next section.

The Gas Target

For efficient HHG, a certain gas interaction volume and rare gas pressure is needed. This interaction volume is also called the gas target. Since no material is yet known which provides a high mechanical stability to withstand high pressure and exhibits a high transparency in

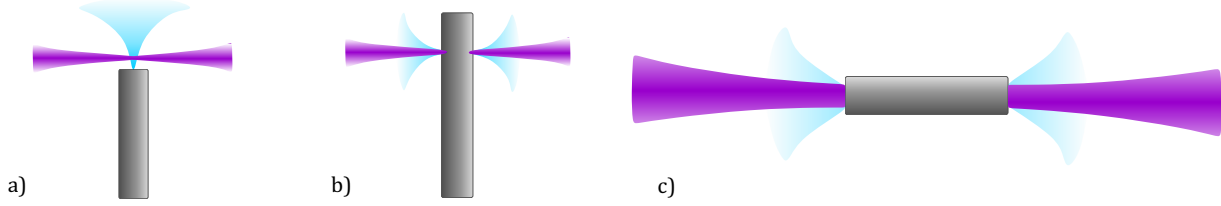


Figure 2.5: Different types of gas targets with the driving laser in violet and the rare gas jet in blue. a) Gas jet out of an single-orifice nozzle with converging inner diameter. b) Capillary with two laser-drilled orifices. c) Gas filled waveguide.

the UV and XUV regime, the rare gas can not be confined to a certain area. In addition, not all electron recombine until the arrival of the next pulse, leading to different HHG conditions than for the previous pulse. Because of this, a guidance for a rare gas stream with a continuous flow to the laser focus is needed.

Different concepts are used for this purpose, one of them being a gas-filled waveguide. It is reported [28] that due to a reduced wavefront curvature in the waveguide a fully phase-matched HHG is achievable. But it is restricted to a loose focusing, because for tight focusing it suffers from incoupling and stability difficulties owing to its dimensions.

For tight focusing a free standing capillary with one orifice is suggested [28] but also metal tubes with two apertures are commonly used [58], see figure 2.5. In the latter type, the interaction region is within the tube and its holes are drilled by the laser itself to keep them and by thus the gas load as small as necessary. Both types of nozzles were investigated in this thesis. The single-orifice nozzle has been tested in two configurations. The first one is a conical glass nozzle with an inner diameter which converges to $150\text{ }\mu\text{m}$ when approaching the orifice and an outer diameter of 1 mm while the second target is a glass nozzle with a constant inner diameter of $500\text{ }\mu\text{m}$. Nickel has proven to be a good material for the nozzle with the laser drilled apertures [59], because it can melt relatively easy under the impact of high intense laser pulses and is commercially available with thin wall thicknesses at a low price value. The investigated nickel tube is of 2.5 mm diameter with 0.125 mm wall thickness and two holes which are drilled by the driving laser itself with the nozzle in the final position.

The expected phase-matching pressure at the position of the laser focus is given by following equation, given in [41]:

$$p = p_0 \frac{\lambda^2}{2\pi^2 w_0^2 \Delta\delta \left(1 - \frac{\eta}{\eta_c}\right)} \quad (2.3)$$

where p_0 is standard pressure (1013 mbar), λ the wavelength of the HHG driving laser, w_0 its beam waist, $\Delta\delta$ the difference of the refractive indices of the fundamental and high harmonic with the desired order, η is the ionization fraction and η_c is the critical ionization fraction. Latter is reached, when the dispersion due to free electrons exceeds the atomic dispersion and no phase-matching can be reached anymore. For an estimation of

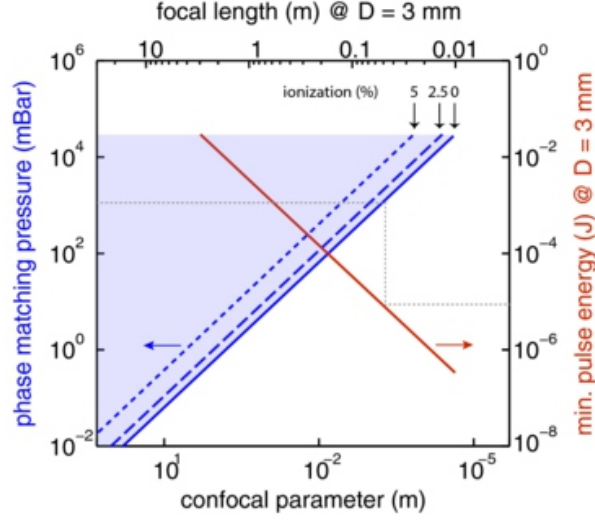


Figure 2.6: Shown is a simulation of the phase-matching pressure of argon as a function of the confocal parameter for the 21st harmonic of a driving laser with a central wavelength of 800 nm, a pulse duration of 45 fs, 1.4×10^{14} W/cm² peak intensity. Graph taken from [40].

the phase-matching pressure which is to be expected in our HHG setup, this formula is consulted, with an ionization ratio of $\eta/\eta_c = 0.9$, since one might be interested in a high intensity where phase-matching is still possible, to achieve the highest high harmonics flux. $\Delta\delta$ was estimated to 282×10^{-6} with data for the fundamental from [27] and from [60] for the 7th harmonic. As a result, in the laser focus, the phase-matching pressure is estimated to be around 2400 mbar.

Heyl *et al.* [40] simulated the phase-matching pressure as a function of the confocal parameter $b = 2\pi w_0^2/\lambda$, where w_0 is the beam waist of a Gaussian intensity profile. His simulation, depicted in figure 2.6 was done for a driving laser with a central wavelength of 800 nm, a pulse duration of 45 fs, 1.4×10^{14} W/cm² peak intensity in argon for the 21th harmonic order. This does not directly apply to our parameters which are of higher driving photon energy and lower high harmonic photon energy and therefore a different dispersion and ionization fraction is expected. But if the differences in refractive indices are in the order of a few percent, and thus, it still is regarded as suitable to get a clue of the order of magnitude of the phase-matching pressure which should be achieved. For our configuration with $b \approx 1 \times 10^{-4}$ m this translates into a phase-matching pressure of a few bars according to the graph, which fits to the result given by equation 2.3.

In order to estimate the gas load which is to be expected for each type of nozzle with a corresponding phase-matching pressure p_{pm} of 1 bar, first the required backing pressure p_b in the supply line of the glass nozzle, has to be determined. Here the backing pressure differs from the pressure in the interaction volume, because this is in the expanding gas jet and not within the reservoir. Since the interaction region in the nickel capillary is within the tube and by this in the reservoir, it can be assumed, that $p_{pm} \approx p_b$.

The centerline¹ pressure in a given distance from the nozzle opening is estimated based on the formulas given in [61]. The calculation is done for argon gas. A free jet expansion is assumed since the following relation, which must be fulfilled for the occurrence of such a supersonic gas expansion, holds true in our case:

$$\frac{p_b}{p_a} \geq \left(\frac{\kappa}{\kappa - 1} \right)^{\frac{\kappa}{\kappa - 1}} \quad (2.4)$$

where κ is the isentropic exponent² and p_a is the base pressure. In the case of argon $\kappa = 5/3$. Along the centerline the pressure is described by

$$p = p_b \left(1 + \frac{\kappa - 1}{2} M_a^2 \right)^{-\frac{\kappa}{\kappa - 1}} \quad (2.5)$$

with the Mach number M_a , which is the ratio of the velocity to the speed of sound. At the orifice of the nozzle $M_a = 1$ but as a characteristic of the supersonic expansion, it increases along the centerline which in turn alters the pressure there. Up to a distance x from the nozzle opening equal the diameter of the orifice, this Mach number increase can be estimated with a power series fit to numerical simulations [61]:

$$M_a = 1 + A(\kappa)\xi^2 + B(\kappa)\xi^3 \quad (2.6)$$

Here $A(\kappa)$ and $B(\kappa)$ are constants that can be found in [61] and $\xi = x/d$ is the relative distance to the orifice diameter d .

A mass flow rate G now can be described, which is the total mass per second streaming out from the nozzle into the vacuum chamber. To keep the vacuum pumps running, this quantity should be minimized.

$$G = Aw\rho \quad (2.7)$$

A denotes the nozzle's orifice area and ρ and w the density and flow velocity, respectively:

$$\rho = \frac{p_b M}{RT_0} \left(1 + \frac{\kappa - 1}{2} M_a^2 \right)^{-\frac{1}{\kappa - 1}} \quad (2.8)$$

$$w = M_a \sqrt{\frac{\kappa RT_0}{M} \left(1 + \frac{\kappa - 1}{2} M_a^2 \right)} \quad (2.9)$$

Where M is the molar mass of the rare gas and $M_a = 1$ at the nozzle opening. Equation 2.4 must be fulfilled and the gas in the reservoir is assumed to be at rest and an isentropic flow with no friction or heat conduction.

¹By centerline, an axis normal to the orifice and symmetrically centered with respect to the orifice's border is meant. Here, the pressure outside the nozzle along the centerline as a function of distance to the opening is estimated.

² $\kappa = C_p/C_v$ is also known as the heat capacity ratio of the heat capacity of constant pressure to heat capacity at constant volume for a real gases.

The mass flow out of the glass nozzle can be calculated in a straightforward manner by inserting equation 2.8 and 2.9 into 2.9 with a nozzle diameter of 150 μm . It is assumed that the pressure at the nozzle's exit is constant for the hole cross-section.

For the metal capillary first an estimation of the size of the laser drilled holes need to be done. For this purpose the beam focus is considered to be in the center of the axis between both orifices. Considering a Gaussian beam, the spatial width can be calculated at the capillary's wall. Based on the investigation of such a trial capillary, a diameter of 180 μm of each hole is estimated. As already mentioned, $p_{pm} \approx p_b$ is assumed and of course both orifices have to be taken into account as an exit for the gas jet.

As a result, figure 2.7 shows that for a phase-matching pressure of 1 bar at an assumed center of the laser beam as close as $x = 2w_0$ with respect to the nozzle opening, a backing pressure of 2.4 bar is needed. For the sake of a more generalization, the pressure in the graph is normalized to the backing pressure and $\xi = x/d$, which is the ratio of the distance of the nozzle to its opening diameter, is introduced. For the needed phase-matching pressure, the glass nozzle configuration shows a 18 % lower mass flow rate G compared to the nickel capillary with 1 bar backing presser, since $p_{pm} \approx p_b$ is assumed for this type of nozzle.

The main requirement on the gas target however is to allow for high conversion efficiencies from the driving field into the desired high harmonic and a stable high harmonic photon flux. The metal capillary with the laser drilled holes resulted in a lower high harmonics photon flux than the glass nozzle. This might be, because of a too large interaction volume within the tube, whereby reabsorption of the XUV photons by the noble gas occurs. In terms of stability, it was not possible achieve a stable XUV flux from the laser drilled capillary. Pointing jitters of the driving laser have a huge influence on the flux, because the beam is easily clipped and diffracted by the drilled aperture, resulting in a very unstable XUV flux. Also the aligning procedure through the two small holes is very difficult. All these aspects lead to an enlarging of the orifices with time which cases a reduced noble gas pressure within the tube and changes the conversion efficiency. The ablation of the tube in general is a risk of contamination of the other optical components with nickel. Because of all this negative aspects, a further characterization of the XUV light source with this kind of gas target was dropped and will not be further considered in this thesis.

In addition to these advantages of the glass nozzle against the metal capillary, the first one in allows for a very simple but highly efficient way of catching the rare gas jet and therefore reduces the overall chamber pressure significantly because of its gas jet being perpendicular to the laser beam. This important feature for achieving phase-matching will be discussed in the next section.

2.2.2 The Gas-Catch

One of the technical challenges about the tight focusing configuration is to induce a confined, high-density, free standing gas volume under vacuum. Even if short gas burst could be managed by the vacuum system, a long term gas load must be significantly lower to keep the system running. But high statistics measurements tend to be in the order of hours

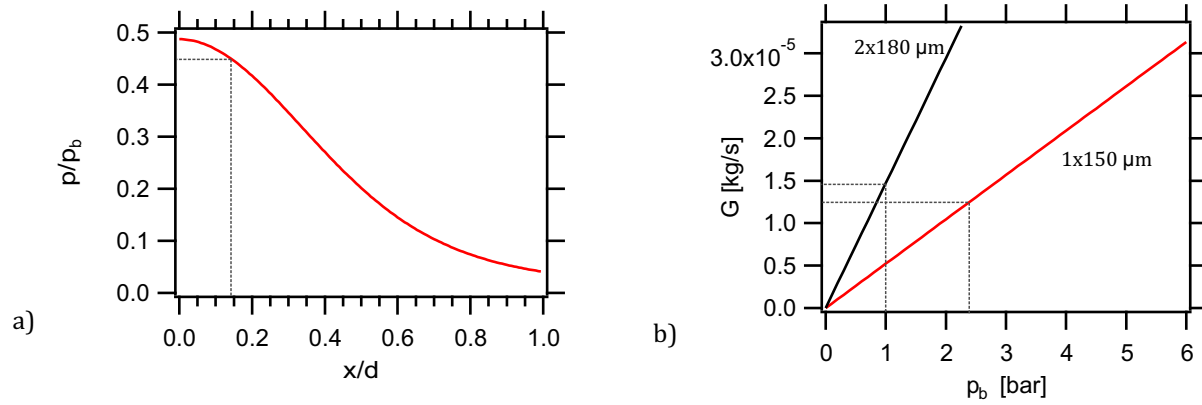


Figure 2.7: a) To the backing pressure p_b normalized centerline pressure versus the relative distance x/d . The markings correspond to a $150 \mu\text{m}$ orifice diameter and a $2w_0$ distant laser focus where a pressure of 1 bar is desired. b) Theoretical mass flow rate out of the glass nozzle with an $150 \mu\text{m}$ orifice (red) and a metal capillary with two $180 \mu\text{m}$ diameter openings (black) against the backing pressure.

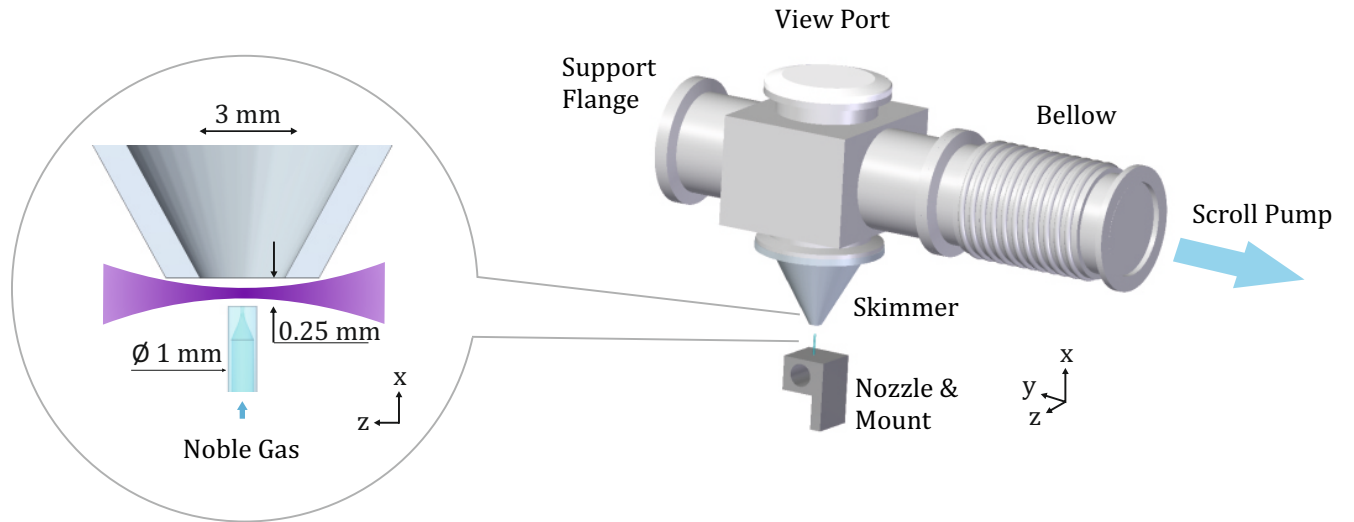


Figure 2.8: *left*) The converging glass nozzle with an orifice of $150 \mu\text{m}$ and the skimmer with the laser focus in between is shown in a vertical cut. *right*) Depicted is the assembled gas-catch with the skimmer, the KV40 cross-piece, the view port and a bellow which differs from the real one. Not shown are the clamping rings and the hanger assembly for the cross-piece on the free KV40 flange.

or even days. In fact, pulsed gas valves have been tested [62] but there, this technology was limited to very low repetition rates of 10 Hz and not useful for our high repetition rate system. The experiment itself often requires a UHV base pressure whose realization becomes trickier the higher the gas load is. Due to this challenge, many high repetition rate HHG setups suffer an inefficient harmonics generation, because they can not reach the phase-matching pressure [40, 63].

Indeed, trying a nozzle with a 150 μm opening, the chamber pressure and turbopump current increased vastly in our setup. For a long-term operation, a turbopump current of 2 A was found to be a threshold, which should not be exceeded in order to prevent overheating or slowing down of the turbomolecular pump. This limit was already reached with 400 mbar of argon backing pressure, see figure 2.10. To avoid running into this limitation, a simple apparatus which catches most of the interaction media, was installed. The basic idea is, that the expanding gas jet shoots into a small inset vacuum tight chamber, after leaving the laser focus behind, which is separately pumped by a Edwards XDS35i scroll pump.

The skimmer has an orifice of 3 mm and is vis-à-vis to the gas target, see figure 2.8. It is shaped like cone to have a small cross-section close to the opening and hence not clipping close by propagating beam towards the focusing mirror. On the other side, a fast increase in the lateral cut is desired to allow a free expansion of the gas and enables an efficient pumping, since the flow rate scale in the expected regime of Knudsen flow with $L \propto r^4$. This part was manufactured individually, whereas the other parts consists of standard opto-mechanical or vacuum components for a quick availability and easy maintenance. The main connection body of the gas-catch, where the skimmer is attached to, is a standard KV40 cross piece. Another requirement for the construction is the freedom to move in the x, y, z axis while in operation. This is necessary because the gas target owns the same degree of freedom and the gas-catch has to follow the target. This is realized by a three-dimensional translation manipulator, attached to the HHG chamber, on which the gas-catch is mounted. The top port of the cross piece is covered with a window flange. Since the cover of the HHG chamber is transparent it is possible to align the gas-catch by directly observing the nozzle. The vertical axis can be adjusted via scattered light from the driving laser beam or on the XUV flux signal, since it should be as close to the focus as possible without clipping any beam. The connection between the HHG chamber, and thereby the scroll pump, with the gas-catch is done with a very flexible metal bellow which allows a wide range of movements without putting a critical amount of force on the construction, risking its stability. For a better visualization see figure 2.8.

A different skimmer configuration, where the gas target is completely inserted into the skimmer opening and provided with two small holes for the laser, was also in discussion. Apart from a way more complicated aligning procedure, the actual expected advantage of a reduced chamber pressure, turned out to be false. This pressure characterization was done in a foregoing test with a simplified catching device which had no laser orifices nor the cone shape. Figure 2.9 shows data taken with the currently used skimmer and the

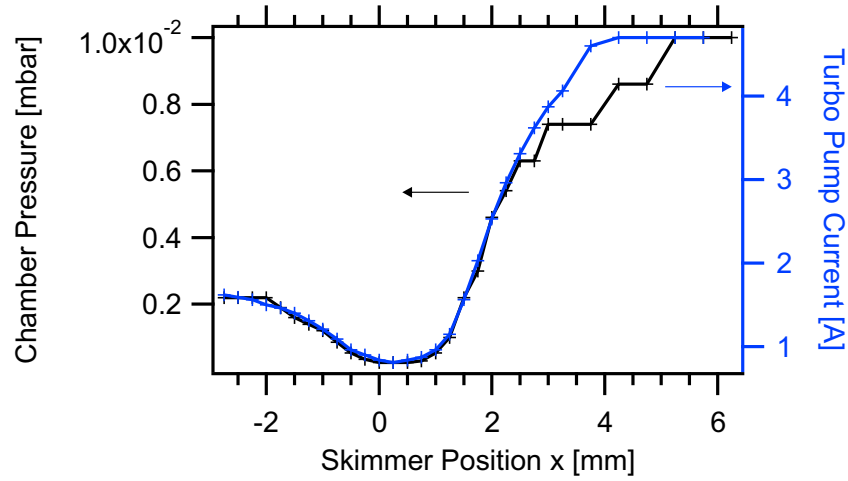


Figure 2.9: The evolution of the HHG chamber pressure (black) and the turbo pump current (blue) against the skimmer position relative to the nozzle opening are traced. Position $x = 0$ indicates the point where the nozzle enters the skimmer orifice. The best condition is for a separation from the two parts of about $250\text{ }\mu\text{m}$ observed, which at the same time allows to focus the driving laser in between without being clipped. The measurement was performed with a $150\text{ }\mu\text{m}$ nozzle orifice and 3 bar backing pressure.

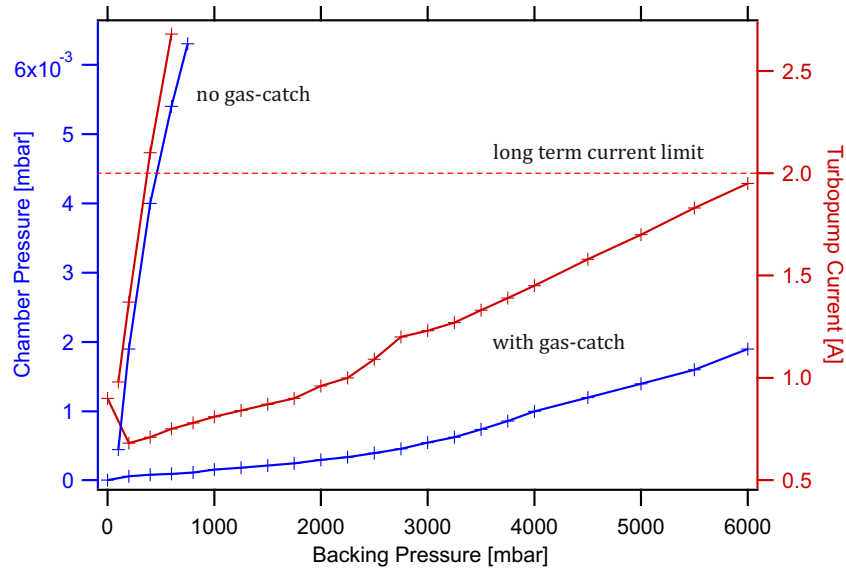


Figure 2.10: The measured HHG chamber pressure and turbopump current vs. the applied backing pressure (argon) with and without the gas-catch is shown. The dashed line marks the maximum current of 2 A which should not be exceeded for a longer time period. Without a gas-catch, this value is already reached for around 400 mbar whereas with gas-catch, this could not be reached within the measured regime of up to 6 bar.

nozzle inserted. Displayed is not just the turbo pump current, which is an indicator for the load the pump has to deal with but also the chamber pressure, measured by a combination of a Pirani gauge and cold-cathode. Position 0 from the x-axis means, where the nozzle enters the skimmer orifice. This positioning range, where the nozzle opening is inside the skimmer corresponds to the alternative approach, except for the two laser holes. The unexpected result is revealed that an introduction of the nozzle into the skimmer does not lower but increase the chamber pressure until it stabilizes. This effect might be due to changed boundary conditions, which disturb the free jet expansion and lead to a increased scattering, or the pressure difference is not good enough anymore, in order for the free jet expansion to occur. This was not further investigated but taken as a justification for the apparatus which does not enclose the nozzle.

In operation, the gas-catch has a significant influence on the vacuum system. This is depicted in figure 2.10. The red line marks the maximum current of 2 A which should not be exceeded for a longer time period. Without a gas-catch, this value is already reached for around 400 mbar with argon and a nozzle with a 150 μm orifice, whereas with gas-catch, this could not be reached within the measured regime of up to 6 bar. Together with the estimated phase-matching pressure of a few bars, this means we are no longer limited in phase-matching by the vacuum system.

2.2.3 Spectral Monochromatization

As pointed out in chapter 1.3.4, a typical HHG spectrum has more than just one harmonic but several odd multiples of the fundamental laser which even can be of a similar intensity, known as the harmonic-plateau. When it comes to the application on photo-electron spectroscopy, this is a problem. Electrons which were photo-emitted by a different harmonic than the desired one, generate a replica of the electronic structure on the analyzer, separated in energy by the difference of the actual exciting photon to the desired photon energy. But the actual situation is even more complex, since the electronic structure of solid state system does not exhibit a mono-energetic but very complex structure. The separation of the harmonics scales with 2ω , with ω being the driving laser frequency, which in our case results in 6.2 eV spacing between the harmonics. Photo-emitted electrons are detected with a kinetic energy E_K of $E_K = \hbar\omega - E_B - \phi$ where $\hbar\omega$ is the XUV photon energy, E_B the electron's binding energy and ϕ the work function which depends on the observed material. Below the Fermi level (higher binding energy), almost all the energy states are occupied at room temperature and for this reason contribute strong to the photo-emitted electron signal. In contrast to this, states above the Fermi level are basically unoccupied, when no special excitation process like pumping with photons in the visible spectrum is applied, and thus do not contribute to the detected signal. Lower harmonics than the designated one play a role when electrons are observed with at least $2\hbar\omega$ higher binding energy than the Fermi energy E_F . Because then these electrons are detected at the same energy as the electrons from the Fermi level, excited by the lower (5th) harmonic. Since that strongly bound states are almost completely occupied, they just contribute to the electronic properties of a material in a minor way and are to a minor degree of interest. On the other side, higher harmonics

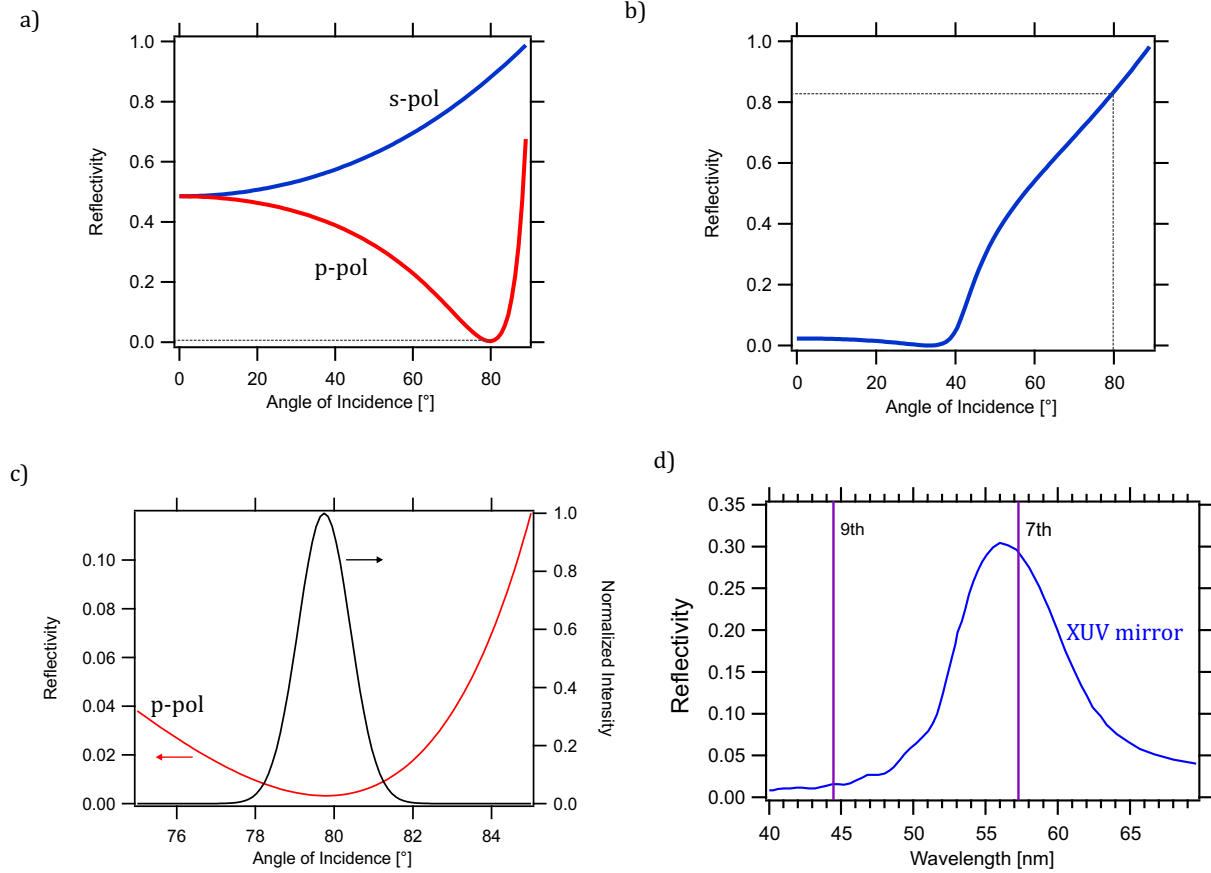


Figure 2.11: a) Calculated Si wafer reflectivity for p-polarization (red) and s-polarization (blue) b) Calculated reflectivity of the Si wafer for the 7th harmonic with a reflectivity of 83% at an angle of incidence of 79.8°. c) Magnified section of the p-polarized reflectivity (red) of 400 nm on the Si wafer around the Brewster's angle. In black, the weighting function for the total reflectivity is shown. To estimate the total reflectivity, it has to be considered, that the divergent not only incidents at the Brewster's angle, but also small deviations of it. In combination with a Gaussian beam profile, each angle can be related with an intensity portion. d) Calculated reflectivity of the XUV mirror with marks for the 7th and 9th harmonic. The 7th harmonic is reflected with 83% for the Brewster's angle of the 400 nm beam.

than the designated one, *e.g.* the 9th, lead to a very strong photoemission, as long as the observation window is below 6.2 eV above the Fermi edge, since then they excite the occupied states. In contrast to core-level electrons, states of band structures for typical TMDCs with $\Delta E \approx 5$ eV [37] below the Fermi edge and above determine the material's electronic properties and thus are of interest for us. To probe the states above Fermi level, they have to be occupied by exciting electrons with a pumping beam. The transfer function still yields an occupation which is orders of magnitude subordinate to the states below E_F . This results in an overlapping, non-separable spectrum.

Also the driving laser field is not unproblematic. Apart from being orders of magnitude higher in intensity than the high harmonics and strongly exciting the sample, which is not always requested, multi-photon photoemission can happen. Here an electron gets excited and photo-emitted by multiple photons from the intense driving laser field. For more details on the process of two-photon photoemission see ref. [64].

For these reasons of not producing and overlapping replicas of the spectrum and a constant excitation of the sample, one single harmonic has to be isolated from the high harmonic spectrum, as well as the driving laser need to be filtered.

A common technique for monochromatization is the use of a grating monochromator [65]. But this comes along with the introduction of a temporal dispersion and a pulse front tilt [66, 67], which lower the time resolution. Time-delay compensated monochromators, which counteract the temporal dispersion, use a pair of gratings [68] with a combined throughput of less than 20%. The problem that arises with such devices is, that they are very difficult to align and just minor deviations from the ideal beam path, such as the divergence of the beam or a mis-aligned optical component or changed beam incoupling result in a distorted and stretched pulse. Multilayer mirrors can provide a good opportunity the reflectivity around a certain wavelength without a significant one on the temporal and pulse front properties of the pulse [69]. But regarding to the availability of coatings for certain energies in the XUV, the overall transmission can drop rapidly when several of these mirror are used.

In our experiment we want to use the 7th harmonic since a photon energy of 21.7 eV is sufficient to cover the full Brillouin zone, as explained in the introduction. The laser system is designed to support this harmonic with a close cut-off harmonic. The idea behind this gets clear, when looking at the equation for the cut-off harmonic (equation 1.70) and the ponderomotive energy (equation 1.64), one can see, that cut-off harmonic scales with ω^{-3} which means, that for a higher photon energy of the driving pulse, the maximum achievable harmonic order gets lowered. At the same time, the harmonic spacing which scales with 2ω increases with an increased driving pulse photon energy. As long as the necessary peak intensity for tunnel ionization can be reached and the designated harmonic is part of the harmonic-plateau, increasing ω results in a better single-atom response (section 1.3.2) and a better possibility for the isolation of single harmonic, due to the enlarged harmonic spacing. Applying the cut-off equation on our system and considering just odd integers, this results in a cut-off harmonic of 13th order. Due to this, the 9th harmonic is still assumed to be in the harmonic-plateau and by that of similar intensity than the 7th. In combination the

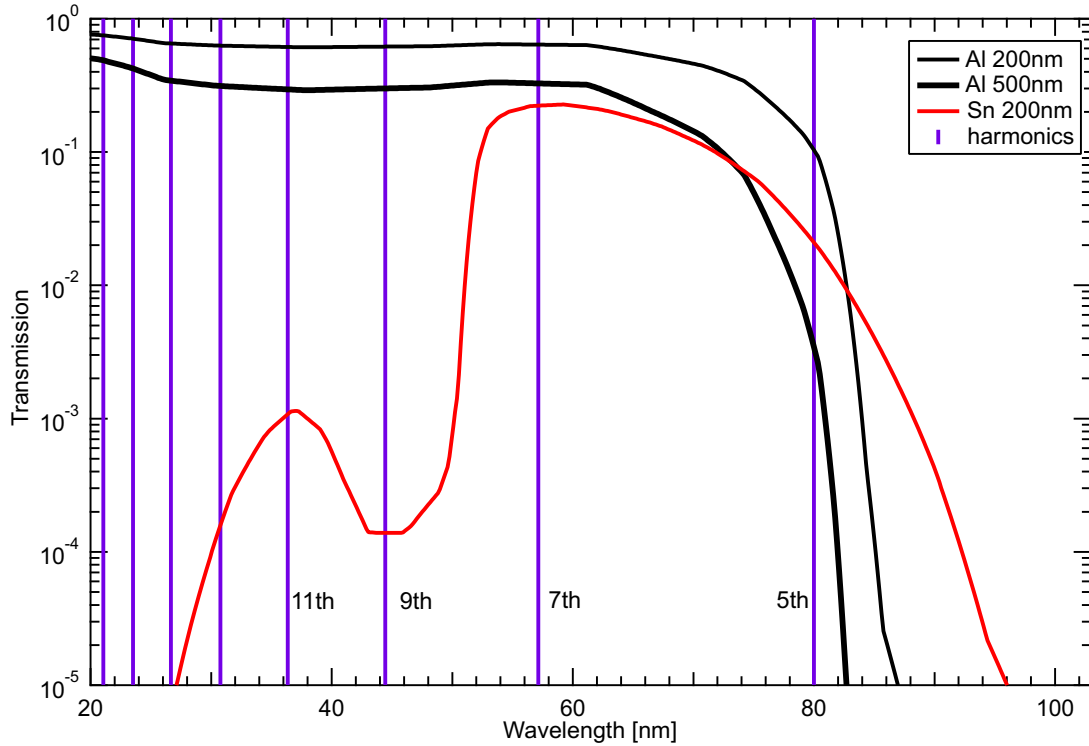


Figure 2.12: Calculated transmission of a 200 nm thick Al- and Sn-filter and a 500 nm thick Al-filter. The positions of different orders of high harmonics are marked by vertical lines. Despite the highest total attenuation of the 7th harmonic of the Sn-filter, compared to a equally or more than twice as thick Al-filter, provides the best contrast of the 7th to its neighboring harmonics and thus is the filter of our choice, because the isolation of the 7th harmonic is the main purpose of the metal filter.

before mentioned observed energy windows, the 9th harmonic would mess up almost every measurement and has to be attenuated exceptionally. Our approach is to isolate the 7th harmonic, without the use of a grating-monochromator. The harmonic separation which in our case is 6.2 eV. With this relatively huge energy separation, other energy selective components than grating-monochromators often can be applied more easily. In our case, the isolation of the 7th harmonic is achieved with the reflection on a silicon waver at Brewster's angle, only one multilayer mirror for focusing and thin metal films, as will be explain in more detail now.

Silicon Wafer at Brewster's angle

After the high harmonics generation in the noble gas, the collinear propagating and p-polarized UV and XUV beam hit on a silicon waver plate, a at an incidence angle corresponding to the Brewster's angle for 400 nm. This leads to a maximal suppression of the p-polarized part of the UV beam, whereas the 7th harmonic at 57.1 nm still gets

reflected. A calculation for the Brewster's angle and reflectivity was performed. For this purpose, a 2 nm thick SiO_2 cover-layer of the Si wafer was considered, which is a typical for the oxidation process which occurs when an untreated Si surface is exposed to an oxygenic environment, such as air. The resulting curves are plotted in figure 2.11. According to this, a Brewster's angle of 79.8° for the 400 nm beam and a 7th harmonic reflectivity of 83% are expected. This way, most of the UV is separated from the XUV. For an estimation of how much of the UV still is reflected, following considerations were done. The beam has a divergence and for this reason not only hits the wafer at Brewster's angle, but also in slightly different angles, leading to a higher reflectivity than at Brewster's angle. In addition, when assuming a Gaussian beam, the intensity over this angle distribution is not uniform but follows a Gaussian profile as a function of angle. Consequently, each angle of incidence corresponds to a certain reflectivity, weighted by a portion of the intensity related to the Gaussian profile. Mathematically translated this means, the reflectivity curve is multiplied with a normalized Gaussian, not convoluted. An illustration of this is depicted in figure 2.11 c). To fit the Gaussian to the present case, the beam's divergence is needed, because this angle, calculated by

$$\theta = \arctan \left(\frac{\lambda}{\pi w_0} \right) \quad (2.10)$$

corresponds to the $1/e^2$ intensity at the optical axis [32] and thus is optimal to calibrate the Gaussian function. With a beam divergence of 1.3° and integrating over the weighted reflectivity, a total reflectivity in power of the 400 nm beam is estimated to 0.4%.

XUV Mirror

After the silicon waver, the beam is reflected on a refocusing mirror, which consists of a multiple layer coating of Si/Sc, tailored for a maximum reflectivity for 22 eV near a normal angle of incidence. A reflectivity curve is given in figure 2.11 with a reflectivity of 29.6% for the 7th harmonic, while the most critical 9th harmonic is only weakly reflected with about 2%.

Thin Metal Filters

Thin metal filters with a thickness of a few hundreds of nanometers can provide a good opportunity to select certain regimes of wavelength due to their specific transmission properties. In our setup, we have the possibility to insert two such metal film in series. The thin metal films are free-standing, attached on a metal O-ring mount. As material 200 nm of Sn and Al as well as 500 nm of Al are currently mounted in the beamline. For the energies we use, tin offers a very convenient transmission window, which is depicted amongst others, as calculated transmission curve in figure 2.12 with data taken from [70]. Here we especially want to focus on the contrast of the 7th to the 9th harmonic. As shown, aluminum does not absorb the 7th harmonic very strong with a transmission of 64% for a 200 nm thick foil, but the 9th harmonic is equivalently strong transmitted. Tin exhibits a different transmission

characteristic, with a local minimum for the 9th and a local maximum for the 7th harmonic. Also higher harmonics than the 9th are attenuated very strongly, while with aluminum, the attenuation is does not alter significantly compared to the 7th harmonic. When looking at lower harmonics, then the tin provides the better attenuation for the 5th compared with aluminum of the same thickness. This makes Sn a very good filter possibility for our purposes. Due to its strong contrast and high absorption, only 200 nm thick filters are considered.

A summary of the theoretical reflectivity or transmission for each of these elements for the 7th and 9th harmonic is given in table 2.1. For the 7th harmonic, an overall transmission of 3.6% and $1 \times 10^{-4}\%$ for the 9th harmonic result with the assumptions made in this section.

	Si Wafer	XUV Mirror	Sn 200 nm	Al 200 nm
7 th	0.85	0.30	0.22	0.64
9 th	0.88	0.02	1×10^{-4}	0.62

Table 2.1: List of theoretical reflectivity or transmission factors of each filter element for the given harmonics.

2.3 XUV Characterization

In the previous section, the concepts and realizations of our monochromatized XUV light source were introduced. Following those considerations, we were able to set up a high-repetition rate XUV light source, functioning as a tool for trARPES measurements. In this section, the measured XUV pulse is characterized in its spectrum and energy resolution as well as the XUV flux and its dependency on the pressure and input power. How each measurement was done and thereby the evolution of the beamline are also introduced.

2.3.1 Spectral Characterization

For the spectral observation of the XUV source, a McPherson 234/302 VUV Monochromator with 0.2 m focal length and an entrance slit with an adjustable width from 0.01 mm to 3 mm is used. The concave corrected grating is platinum coated with 2400 grooves/mm, allowing for a detectable wavelength range from 30 nm to 275 nm with a resolution of 0.06 nm. The detecting unit is a Andor DO420 CCD camera with a 1024×255 pixel-array and a pixel size of $26 \times 26 \mu\text{m}^2$. It can be cooled thermoelectrically to -80°C . The arrangement of the spectrometer and the XUV diode (see next section) are already part of the final beamline and can be seen in figure ?? . The incoupling of the spectrometer, via an Au mirror without protective over-layers, is done after the filter-wheel chamber and a gate-valve, where the second thin metal filter is mounted. This mirror sits together with the XUV diode on a

manipulator, perpendicular to the beamline. When fully extracted, the XUV beam can go towards the ARPES chamber without disturbance.

When the full spectrum was measured, what attracted attention was that harmonics which do not coincide with the energy of the current central wavelength setting of the spectrometer, are displayed at a wrong wavelength or energy. Concretely, the 4th harmonic showed up at 49 nm instead of 44.4 nm. This is important, not just for the detection of other harmonics, but also for the determination of the bandwidth of the harmonic of interest, because the wavelength scaling is not correct but for the currently set central wavelength. A possible explanation for this is, that the incoupled beam has a discrepancy to the ideal beam path and the center of the CCD array from the camera does not perfectly match with the direction of the first diffraction order of the set central wavelength from the grating. To compensate for this mismatch a correction function was written, providing a good correction for the proximity region to the central wavelength allowing for bandwidth measurements of the current central wavelength with a reasonable result. For the overall spectra, the measurements for each harmonic are merged together from spectra taken at the expected central wavelength according to harmonic order. All shown spectra are treated with this correction.

In figure 2.13 the full measured spectrum is shown. In order to avoid a saturation of the camera by stray light, one of the metal filters must be inserted into the beam path. Figure 2.13 contains a spectrum measured with a 500 nm thin Al-filter and another, acquired with a Sn-filter of 200 nm thickness. Due to this and the other wavelength filtering elements, described in section 2.2.3, no characteristic harmonic plateau can be observed, because each harmonic is attenuated differently, but both differently filtered spectra are needed to gain a better understanding of it. Also the efficiencies of the grating and the CCD camera are a function of wavelength and alter the appearance of the spectrum. Only for the 5th, 7th and 9th harmonic, the peaks are corrected by these factors, since they needed to be taken from graphs in the data sheets.

Observing the aluminum-filtered spectrum one clearly sees a peak at the 11th harmonic, which does not occur in the tin-filtered spectrum (not shown in the spectrum, because the signal drops rapidly), but would be expected since the calculated cut-off harmonic is the 13th. The appearance of the 11th harmonic thus confirms that the estimated ponderomotive energy is reached, but since the 13th and higher harmonics are out of detection range of our spectrometer grating, this just can be seen as a lower limit. In the aluminum-filtered spectrum, the 9th and most undesired harmonic for our applications is still quite present. Apart from that, the 5th harmonic can be misinterpreted. It seems like the energy correction deviates strongly from the expected wavelength of 80.0 nm for this regime, either being at 73 nm or at well pronounced 89 nm. Comparing this with the tin filtered spectrum gives more information about this. Here, the 9th harmonic is much weaker compared to the Al-filtered spectrum. But at the same time, the peak at 89 nm is attenuated by the same amount of $\sim 3 \times 10^{-3}$ as the 9th harmonic. This indicates, that the strong peak at 89 nm corresponds to the second order diffraction of the 9th harmonic. And indeed, comparing the

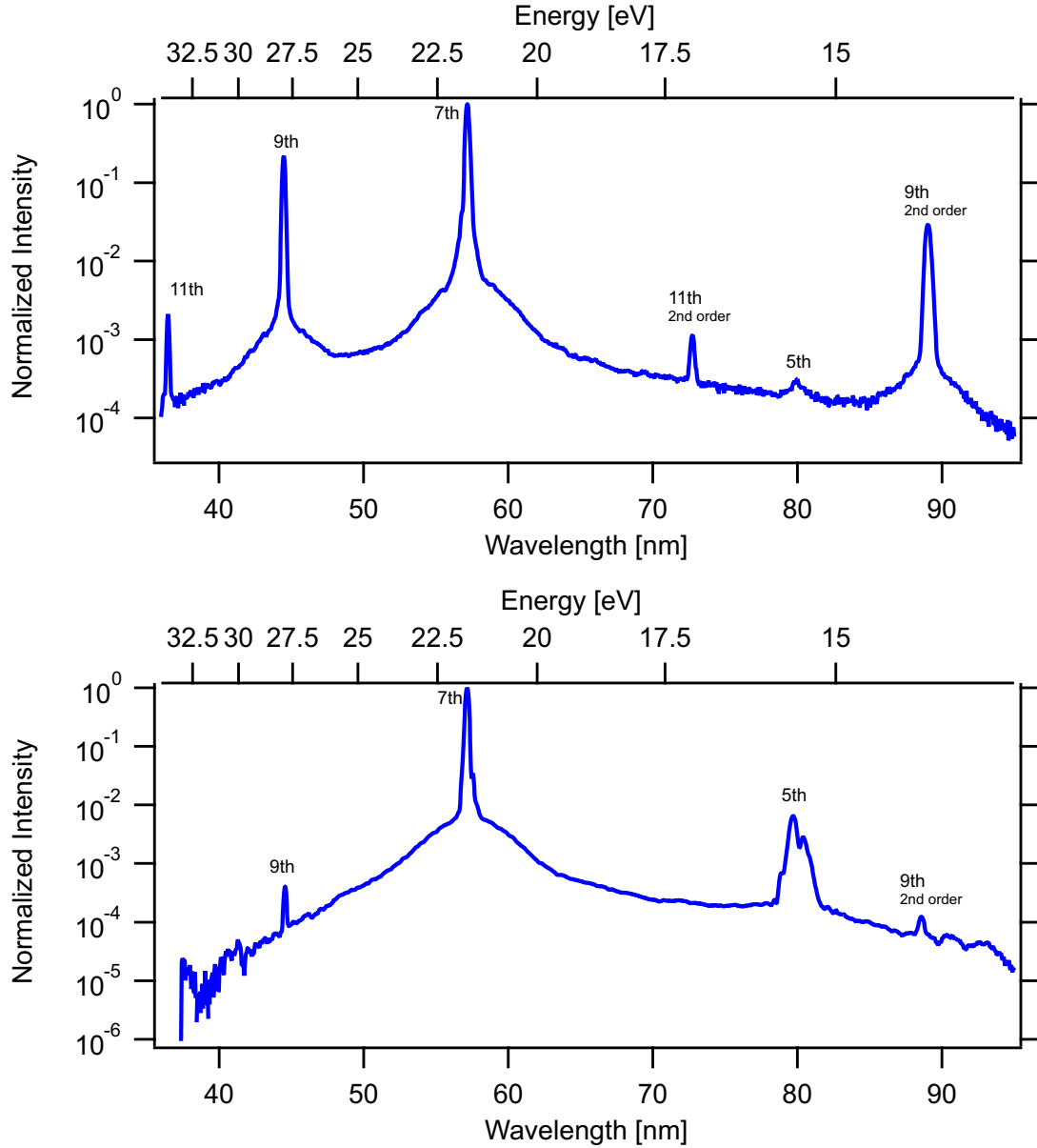


Figure 2.13: *Top*) Al-filtered spectrum as a composition of spectra taken at a central wavelength of 44.4 nm, 57.1 nm and 80.0 nm. *Bottom*) Sn-filtered spectrum with the same merged spectra than the top spectrum. Comparing both spectra gains insight into the structure of the original unaffected HHG spectrum, *e. g.* by comparing the attenuation ratios of different peaks, which then can be related to each other of being higher diffraction orders. A complete reconstruction at this point is not possible, since the spectra are still provided with a wavelength dependent diffraction efficiency, transmission through the beamline and quantum efficiency in the detector.

wavelengths of both peaks, they differ by a factor of 2, as it is expected from the diffraction equation, which is

$$m\lambda = d(\sin \theta_i + \sin \theta_r) \quad (2.11)$$

where m is the diffraction order, λ the diffracted wavelength and θ_i and θ_r the angle of incidence and the reflected angle, respectively. The same holds for the peak at 73 nm, being the second order diffraction of the 11th harmonic, leaving a very small peak at 80.0 nm for the 5th harmonic in the Al-filtered spectrum.

Harmonics Contrast

As already mentioned, for spectroscopic experimental methods, a single isolated harmonic is needed. For this purpose the contrasts of the 7th harmonic to the neighboring 5th and 9th harmonic were determined. This was done for the 200 nm thin Sn- and 500 nm thin Al-filter. To extract the contrast from these data, the background for each harmonic was subtracted and subsequently the relative intensity to the normalized 7th harmonic was calculated. In order to do so, first, the wavelength dependent grating and CCD camera efficiencies needed to be taken into account. In table ??tb:2.2 these efficiencies are stated, with the estimated uncertainties due to the uncertainty in extracting these values from the given graphs in the data sheets. Figure 2.14 shows these harmonics for the Al- and Sn-filter and table 2.2 summarizes the results.

The main interest in this analysis lies in the best suppression of the 9th harmonic. In contrast to the Al-filter, where the 9th harmonic still exhibits a relative intensity of 0.19 to the 7th, the Sn-filter leads to a relative intensity of the 9th harmonic of just 2.6×10^{-4} . This is a very good ratio achieved by just one Sn-filter and justifies the usage of tin as spectral filtering component. With the possibility to insert another tin-filter into the beam path, an even better contrast can be generated.

However, what is noticeable for the Sn-filtered 5th harmonic is a double featured peak. It stays unclear if the same occurs for the Al-filter, since there the 5th harmonic is very noisy due to its strong attenuation. Interestingly, the other harmonics does not seem to be affected in a considerable way. A possible explanation for this is given in [71]. Lower order high harmonics can be generated at the slope and not at the peak of the fundamental pulse. Thus, when the ionization fraction rises with the rising edge of the pulse, the harmonics generated after the peak intensity see a different phase- and blue-shift than the one from the rising slope. This would result in a harmonic splitting.

Harmonics Bandwidth

The bandwidth of the harmonic determines the minimum energy resolution which can be achieved by the ARPES measurement, since it is the main limiting source as long as the analyzer operates in well set conditions (< 30 meV) or thermal broadening is small compared to the XUV energy resolution. The credo here is, the smaller the bandwidth, the

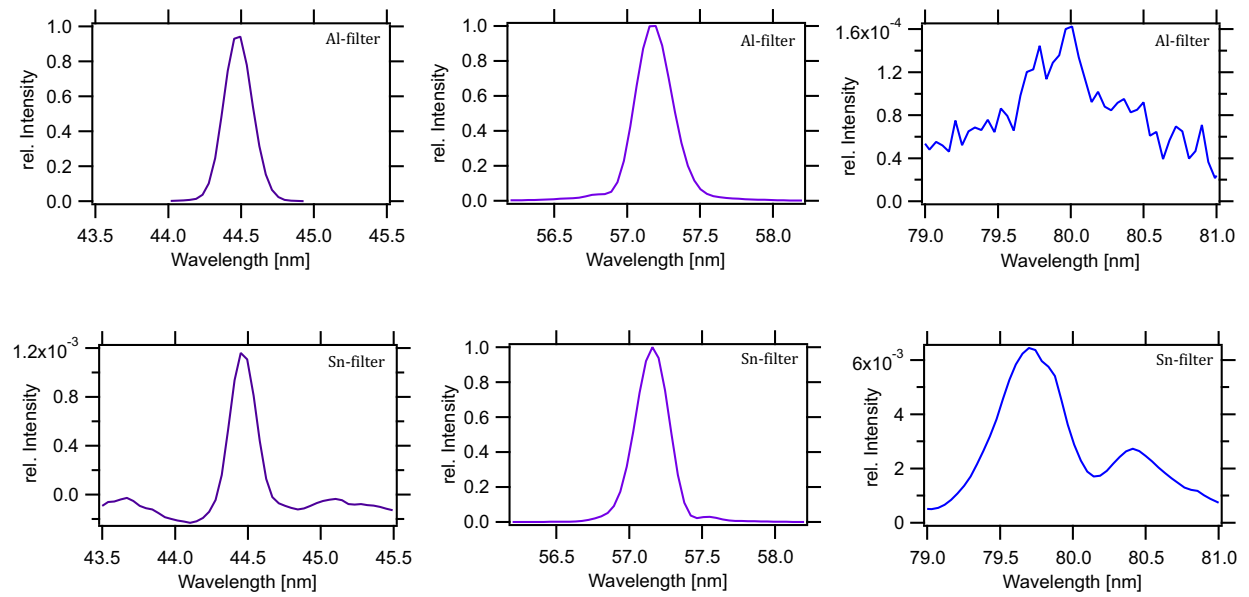


Figure 2.14: Contrast ratios of the 7th harmonic and its neighboring ones, with a relative intensity to the 7th's is shown. Data were subtracted by the background, put into ratio to the normalized 7th harmonic and corrected by the given efficiencies of the grating and CCD camera. Left column corresponds to the 9th harmonic, middle and right to the 7th and 5th, respectively. *Top*) Al-filtered spectrum. *Bottom*) Sn-filtered spectrum.

	9 th	7 th	5 th
Grating Efficiency [%]	0.008 ± 0.001	0.045 ± 0.002	0.052 ± 0.001
CCD QE [%]	25 ± 1	22 ± 1	19 ± 1
Aluminum Contrast	0.9 ± 0.3	1	$(9.3 \pm 0.5) \times 10^{-5}$
Tin Contrast	$(1.3 \pm 0.4) \times 10^{-3}$	1	$(5.6 \pm 0.4) \times 10^{-3}$

Table 2.2: The grating and the CCD camera have efficiency and quantum efficiency (QE), respectively, which are dependent on the wavelength. Thus, the data from the spectrometer have to be treated with these efficiencies to gain information about the achieved contrast of the 7th to its neighboring harmonics. Since the efficiencies read from a graph, they show quite strong uncertainties. The achieved contrasts are listed for a 200 nm thin Sn- and a 500 nm Al-filter. Tin clearly is the to be preferred due to its better contrast values, especially at the 9th harmonic.

better the energy resolution and therefor more desired, because the electronic structure of solid states can exhibit differences of only a few meV. For example, the band gap of a free standing germanene 2D material, is predicted to be of ~ 24 meV at the Dirac points [72]. The best obtained resolution was found for a 150 μm nozzle and a backing pressure of 3500 mbar. Applying this to the simulation from figure 2.7 then this corresponds to a phase-matching pressure of 1600 mbar. A Gaussian fit of this spectrum provides a bandwidth of (105 ± 8) meV, see figure 2.15.

Pressure and Power Dependency

During the experiment, one might be interested in changing the XUV intensity on the sample, in order to avoid saturation, improve the signal-to-noise ratio or other aspects. It is tempting to do so by changing the OPCPA power which is frequency doubled and drives the HHG, because of the motorized waveplate and thin film polarizers combination, it is the easiest way to do so. Whether or not this affects the spectral properties of the XUV is investigated in this section. Another parameter that can be adjusted easily is the backing pressure. Also its influence on the spectrum was observed.

The measurements were performed with Argon and a nozzle with a 150 μm opening. The highest XUV flux was achieved for ≈ 2000 mbar and 100% OPCPA power, which corresponded that day to about 4.7 W. The position of the gas target was optimized for these conditions and not changed during the scan of the backing pressure or fundamental power.

Figure 2.16 shows the results, with the backing pressure dependency on the left and the OPCPA power dependency on the right. Having a look at the FWHM as a function of the backing pressure, a trend of an increased bandwidth towards higher gas densities can be found. A change in the gas density also changes its refractive index, which is $n = n_0 + n_2 I$ with the linear refractive index n_0 . The intensity dependent nonlinear refractive index $n_2(I)$

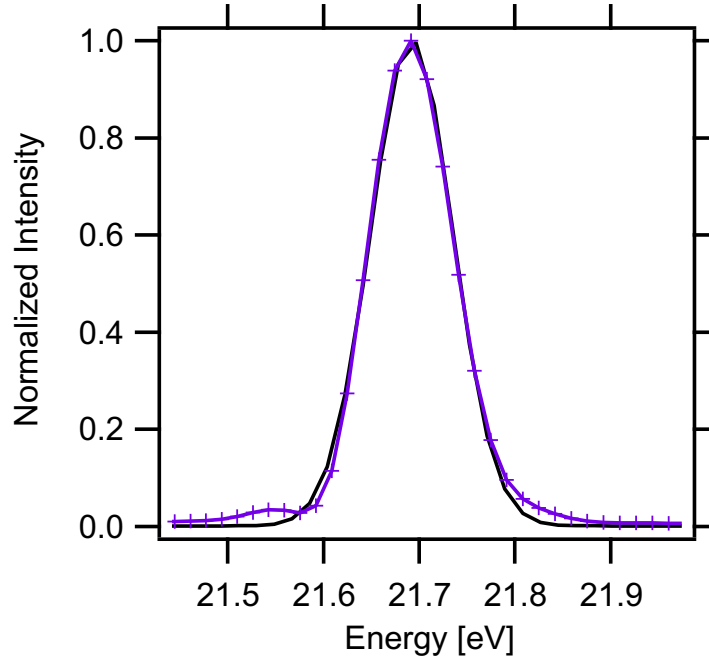


Figure 2.15: The spectrum of the 7th harmonic as a function of energy is shown. A Gaussian fit yields a FWHM of (105 ± 8) meV.

leads to a change of the refractive index, spatially and in time, because of the assumed Gaussian profile in those dimensions and thus affects the phase of the pulse, resulting in newly generated instantaneous frequencies and thus the photon energy, when $\delta\omega_n$ is added to ω_0 , compare equation 1.12. This can explain the increase in bandwidth with higher backing pressures, because as ref. [31] states, additional frequency components $\delta\omega_n$ to the central frequency ω_0 appear when the pulse propagates a distance L in a medium with a time-dependent refractive index:

$$\delta\omega_n = -\frac{\omega_c}{c_0} \int_0^L \frac{dn(z, t)}{dt} dz. \quad (2.12)$$

The linear increase in bandwidth confirms this assumption, since the refractive index scales linearly with the pressure. This leads to a rule of thumb, that the backing pressure should not exceed the minimum that is necessary to achieve phase-matching, otherwise a spectral broadening occurs, which decreases the energy resolution of the ARPES measurement. In addition, the backing pressure should not be changed during the experiment, in order to avoid an energy shift in the recorded photoelectron spectrum. However, the change of the central energy is quite weak and in the order of a tenth of a percent.

The OPCPA dependency reveals a more complex structure, with several effects overlapping, see figure 2.16 right column. In the bandwidth, a significant increase is observed in the range of 60% to 80% of the OPCPA power, followed by a drop until 100%, where the best phase-matching was achieved. Here again, additional frequency components are generated

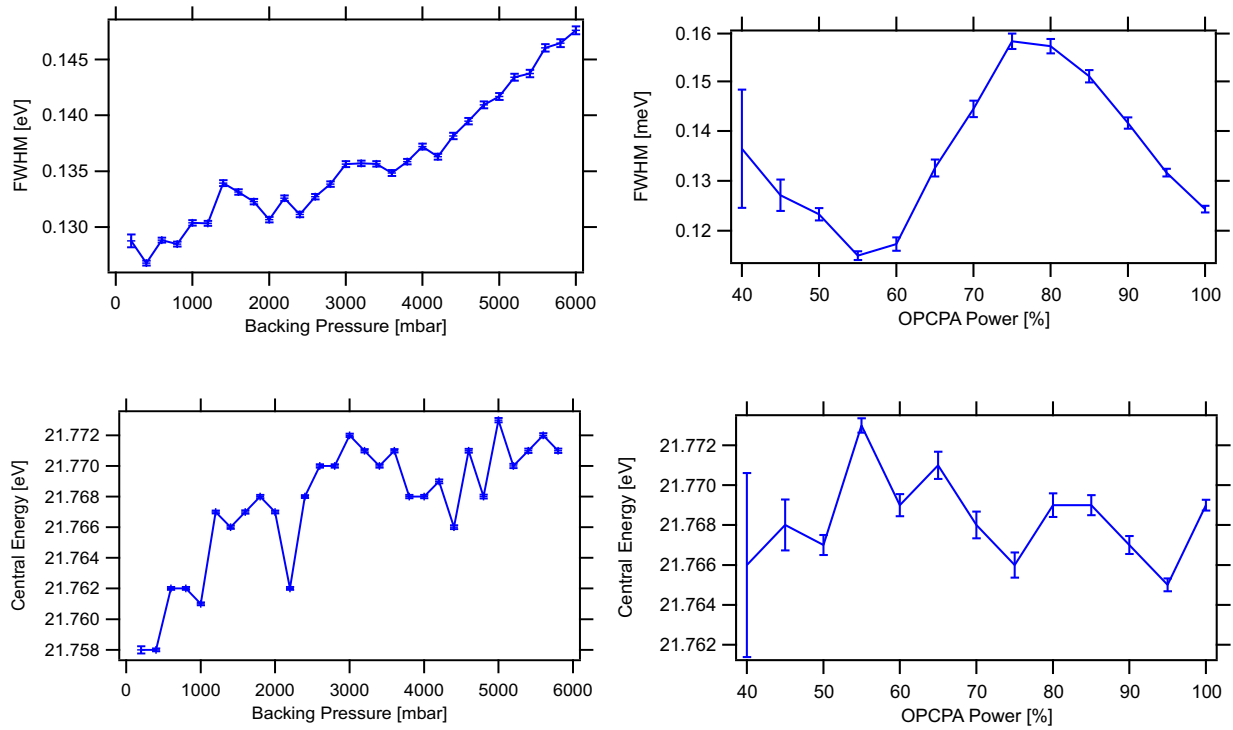


Figure 2.16: *Left*) Investigated influence of the backing pressure on the harmonics FWHM and central wavelength. See the text for its interpretation. *Right*) Investigated influence of the OPCPA power on the harmonics FWHM and central wavelength. See the text for its interpretation.

due to a greater change in the refractive index, contributed by $n_2(I)$ with increasing intensity. With higher intensity, free electrons increase and thus plasma dispersion. This leads again to a change in the refractive index, with a different sign compared to the one for the neutral dispersion. Another intensity dependent contributions to this was introduced in section 1.3.3, where the single-atom phase is intensity dependent, which in turn is strongly time dependent (compare equation 1.61), leading to new frequencies. The sign of its contribution depends on the dominant trajectory, which is phase-matched. In addition to all these effects, a higher intensity corresponds to more laser cycles which reach the intensity for the generation of the 7th harmonic and thus, more time separated contributions resembles with a narrower pulse in the frequency domain [37], reducing the bandwidth. It seems, that all theses effects balance in such a way, that the bandwidth decreases with increasing intensity, at least until the intensity is reached, which was optimized for phase-matching.

In contrast, the central energy does not seem to be affected by a changed fundamental power. Here, the same phase-changing effects should apply as for the bandwidth, except for increased number of contributing fundamental cycles. This could be an indication, that the other effects balance each other out, and the decrease in bandwidth mainly contributes to narrower spectral peaks.

As a conclusion, adjusting the XUV flux via the OPCPA power should be avoided, since it leads to a reduced energy resolution.

2.3.2 XUV Flux

For photoelectron spectroscopy, the number of XUV photons impinging on the sample is highly important. Is the XUV flux too weak, the photoemitted electrons might not be distinguishable from the background, is it too high, the signal is broadened due to space-charge effects between the photoelectrons. A certain flexibility in flux is also required, because different samples have different cross-sections and thus respond differently at a given XUV flux.

In this section, the absolute flux of the 7th harmonic in photons/s and its dependency on the backing pressure and OPCPA power are determined. But before that, the influence of the nozzle geometry and the type of noble gas was investigated.

Nozzle and Medium Dependency

After the nozzle type with two laser drilled orifices did not show promising results in flux and stability, only free jet nozzles with a single-orifice were further investigated. The size of the opening of the nozzle is supposed to influence the efficiency of the high-harmonics generation, because it also influences the size of the interaction volume. Due to a phase-mismatch of the driving laser to the high-harmonic order, a constructive gain in the high-harmonic is only possible within the coherence length, where this mismatch is $\leq \pi/2$.

Investigated were nozzle with an opening of 40 μm , 80 μm , 150 μm and 500 μm , in which the latter one does not have a converging inner diameter such as the others. The applicable backing pressure with the 500 μm nozzle was limited to a maximum of 1000 mbar, because

of its large opening and mass flow rate. If phase-mismatches and reabsorption would not be the limiting factors, this would not matter, because of the larger interaction volume, an equal number of emitting atoms compared to a smaller nozzle can be reached with a lower pressure.

Tabularized results of the XUV flux are shown in table 2.3. They are normalized to the flux of nozzle with the greatest flux, which was the one with the 40 μm orifice. With increasing diameter, the XUV flux decreases, indicating that the interaction volume is too big compared to the coherence length of the XUV generation. In contrast, the variation in XUV flux decreases towards the two smallest investigated openings. Despite that, the 150 μm nozzle was chosen for further characterizations and especially for ARPES measurements, because its greater ratio of gas target volume to focus spot size. Especially drifts of the laser beam would affect the XUV flux in a small gas volume much more. Whether or not this is the case in a time interval of typical ARPES measurements in the order of a day, still needs to be observed.

Nozzle Orifice	40 μm	80 μm	150 μm	500 μm
rel. Intensity	1.00	0.74	0.60	0.13
RMS Stability [%]	2	2	5	29

Table 2.3: Relative intensities and flux stabilities of the 7th harmonic as a function of the nozzle geometry.

The HHG efficiency for different noble gases was also investigated. Tests were performed with neon, argon and krypton. The highest XUV flux in the 7th harmonic was achieved with argon, followed by krypton, which yielded around 78% of the flux generated in argon (compare table 2.4). Heavier noble gases have a higher static dipole polarizabilities $\alpha_{\text{dip}}(\omega)$ for the same wavelength and thus should be more efficient for HHG [27]. But they also have a lower first ionization potential I_p , which lowers the needed intensity at which plasma dispersion from free electrons does not allow for phase-matching anymore. The ionization potential of Ar is best suited for the intensities in our tight focusing setup. The next lighter rare gas, neon, loses drastically in XUV output compared to argon, because its higher ionization potential demands for higher intensities in the laser focus. Compared to the

Noble Gas	Neon	Argon	Krypton
rel. Intensity	0.02	1.00	0.78

Table 2.4: Relative intensities of the 7th harmonic for different noble gases.

phase-matching pressure in Ar, the one need for Kr with a 150 μm nozzle was found to be around 75% of the one used for Ar, because Kr has a greater normal dispersion and thus not as much pressure is needed to compensate for the geometrical phase. Despite the higher pressure needed with Ar, the highest XUV flux in argon comes along another, economical

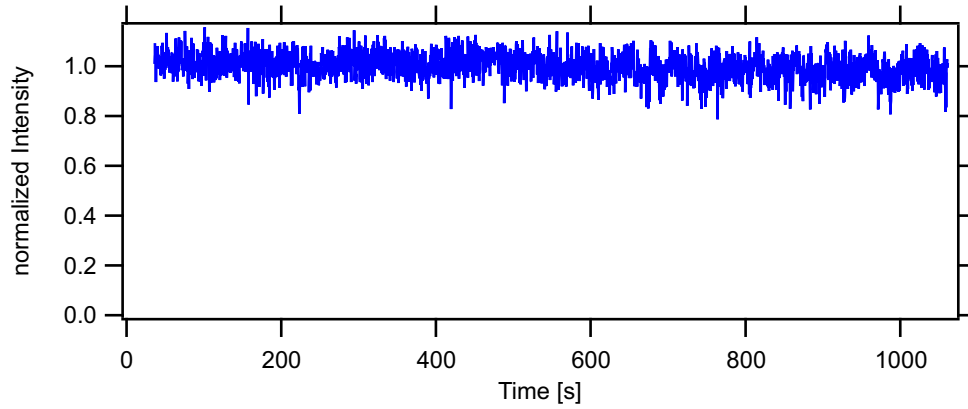


Figure 2.17: Recorded stability of the XUV flux at 100% OPCPA power. The data were acquired for 30 min and shows a standard deviation of 5%.

advantages. Argon is a lot cheaper than krypton, which is an important cost factor for long-term operations.

XUV flux and Stability

As already mentioned in previous sections, the XUV flux is measured with a diode, mounted on a manipulator, together with the incoupling mirror for the spectrometer. The diode is a AXUV100Al model from Opto Diode Corporation and has an active area of $10 \times 10 \text{ mm}^2$, covered with a 150 nm thick Al-filter and thus has a detection range of 17 to 80 nm. The responsivity η of the diode at 57.1 nm is $(0.13 \pm 0.01) \text{ A/W}$ according to its data sheet. The uncertainty is again estimated from the precision of reading the graph. The signal is recorded with a Keithley 6400 picoammeter.

The absolute photon flux ϕ of the 7th harmonic, with one inserted Sn-filter, can be calculated with the formula

$$\phi_7 = \frac{I_7 / \eta_7}{h\nu_7} T_7^{-1} \quad (2.13)$$

$$\text{with } T_7 = T_{Sn7} R_{M7} R_{BP7}. \quad (2.14)$$

Here, I_7 is the signal current which relates to the photons of the 7th harmonic, ν_7 is the frequency of the XUV photon and T_7 is the beamline's transmission of the 7th harmonic, with T_{Sn7} being the transmission of the Sn-filter, R_{M7} and R_{BP7} being the reflectivity of the XUV mirror and the silicon Brewster-plate, respectively.

In the silicon diode, each photon which can pass the aluminum layer and an energy of at least 1.12 eV can contribute to the signal. In order to estimate the share of the 7th harmonic to the total signal, its portion with respect to the 5th and 9th harmonic were taken. This was done by taking the background subtracted, Sn-filtered spectra from figure 2.14 and fitting their profile. Integrating these profiles yields a contribution of the 7th harmonic of 98.7% to the total signal, 1.3% for the 5th and 9th can be neglected, because its

contribution is in the sub-per mill regime. These portion are weighted with the responsivity of the diode for the associated harmonic, yielding a contribution of the 7th harmonic to the total signal current of 99.97%. A leakage of the 400 nm driving pulse can be excluded, because when the noble gas jet stream is turned off, the signal trails off in the background noise, measured without any beam. Whilst for R_{M7} and R_{BP7} only the calculated values are available, the actual transmission of the Sn-filter can be measured. Therefore, the intensity was measured with one Al-filter and again after filtering with an additional Sn-filter. The ratio of attenuation corresponds to the absorption of the tin foil. The mean value from two measurements yields a transmission for the 7th harmonic of $(8 \pm 2) \%$. This is less than half of the simulated transmission (22%). The company of the filters claims a thickness with a tolerance of $\pm 10\%$ [73]. According to the simulation used from reference [74], still 19% transmission would be expected in a 10% thicker foil. Other effects, such as surface oxidation in air to SnO and SnO₂ [75] can explain this reduced transmission, since oxidized tin has a much stronger absorption in the XUV [74]. The filters were exposed to air, when mounted into the beamline.

The highest measured flux with a 150 nm nozzle so far was achieved recently with 10 μ J driving laser power, 2000 mbar backing pressure of argon. In combination with the calculated values for the reflectivity of the Si Brewster-plate and the XUV mirror at 57.1 nm (table 2.1) and the measured transmission of the Sn-filter, a photon flux for the 7th harmonic of $(5 \pm 1) \times 10^{13}$ photons/s is estimated. This is equivalent to a conversion efficiency of the UV into the 7th harmonic of 3×10^{-5} . After spectral filtering, this means a flux of $(1.02 \pm 0.07) \times 10^{12}$ photons/s on the sample.

To the author's knowledge, this is the first time, that equal conversion efficiencies, predicted by Rothhardt et al. [41], of the 7th harmonic from a 400 nm driving pulse under tight focusing conditions, compared to a 50 kHz system used in reference [30], could be achieved.

The large standard deviation is a result of the uncertainty in the filter transmission and the diode's responsivity. The XUV signal exhibits a standard deviation of only 5%, as a measurement over half an hour at full OPCPA power revealed, see figure 2.17.

Pressure and Power Dependency

The in figure 2.18 shown data for the XUV flux as a function of backing pressure were acquired with a 150 μ m nozzle, an argon gas jet and 9.4 μ J energy per pulse. The best phase-matching and by thus the highest XUV flux were achieved with ≈ 2500 mbar backing pressure. Deviations from the phase-matching pressure from other measurements, such as in the earlier section of the spectral characterization, can be explained by different position of the nozzle along the x-axis in frame of reference used in figure 2.8. The growth in XUV flux as a function of backing pressure starts with a quadratic behavior and flattens towards the maximum, where the phase-matching pressure is reached. With a further increase in pressure, the flux decreases linearly again. According to [76, 77], the quadratic behavior resembles to a fully phase-matched case with no reabsorption. As the gas density increases,

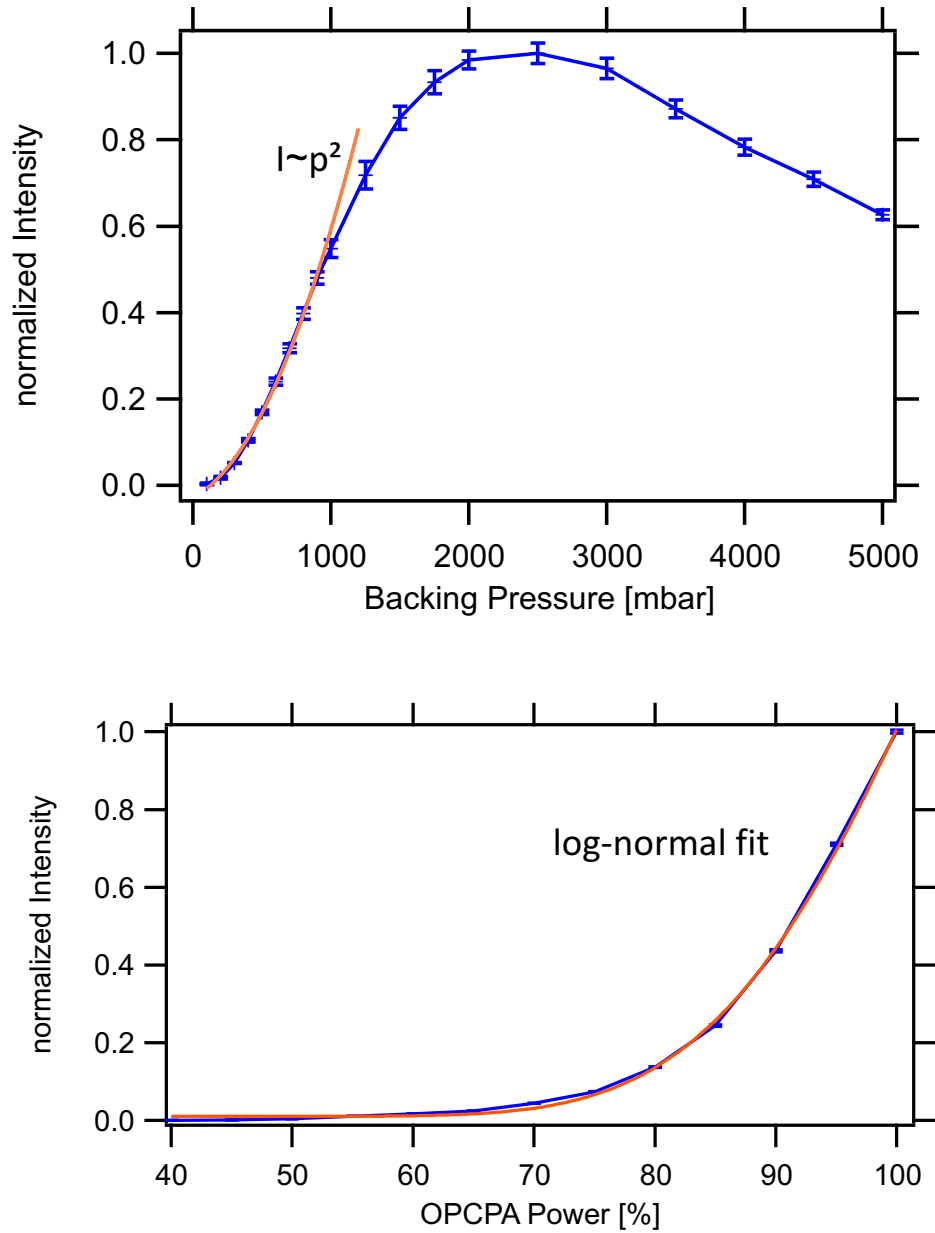


Figure 2.18: *Top*) The XUV flux growth for small backing pressures quadratically, meaning phase-matched conditions and no major absorption occurs. With an increased gas density, also the density of free electrons increases, leading to defocusing as well as an increased absorption due to more gas atoms. Ref. [42] claims, the reduction in XUV flux after the phase-matching pressure is trespassed, claims that the interaction volume is too large compared to the coherence length. *Bottom*) The XUV flux shows a monotonic increase with increasing OPCPA power up to 9.4 μJ energy per pulse as SHG maximum.

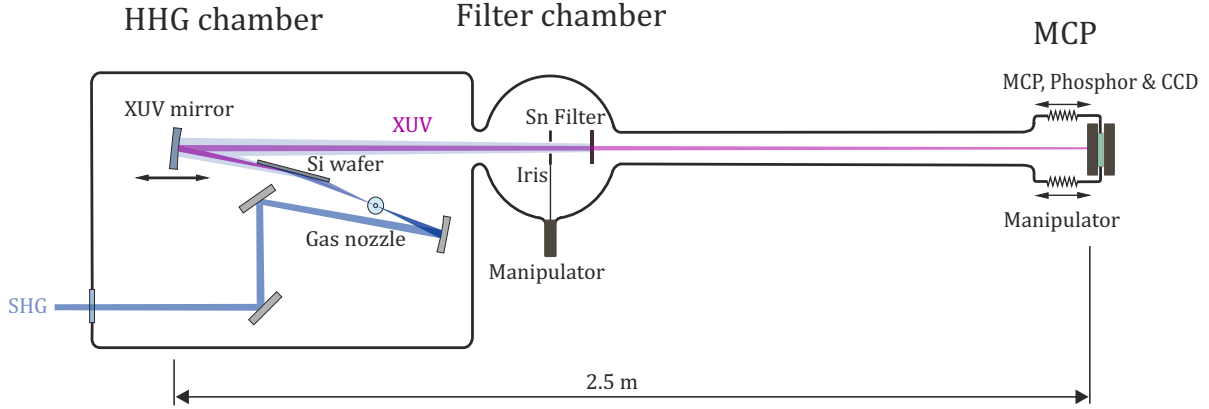


Figure 2.19: Beamline with the temporary assembled MCP for measuring the spot size at a foreseen sample distance of ≈ 2.5 m to the XUV mirror.

more free electrons induce a defocusing of the beam, leading to a change in phase and thus in XUV intensity. Reabsorption is also more likely, when the gas density increases. The linear decrease after the maximum is an indication, that the interaction volume from the gas target is in the order of $1/5$ of the coherence length [42], where the driving and 7th harmonic pulses are phase-matched. Best results are predicted when, the coherence length exceeds ten times the absorption length. This suggests, that higher XUV fluxes can be achieved, when nozzles with a smaller orifice are used.

In terms of XUV flux as a function of OPCPA power, the growth goes can be fitted with a log-normal function (compare 2.18).

2.3.3 XUV Spot Profile

Before assembling the final beamline, a transitory beamline was built to measure the XUV spot profile. For this purpose, a tube was attached to the filter chamber with the detector at its end. The tube's length was chosen in such a way, that the distance from the XUV focusing mirror to the detector was similar to the distance of the final sample position. For fine adjustments, the detector was mounted on a translation manipulator, making it possible to measure the spot in the focus. As detector, a micro channel plate (MCP) which converts the XUV photons into electrons and multiplying those, with a phosphor screen was used. The phosphor screen converts the electrons again into photon, but this time into an energy regime, which can be detected by a CCD camera, placed behind the screen. A schematic setup is depicted in figure 2.19 and the measured focus can be seen in figure 2.20. Using a focusing mirror with a curvature of $r = 600$ mm a $D4\sigma$ spot size of $(356 \pm 3) \mu\text{m} \times (333 \pm 3) \mu\text{m}$ with a mean value of $(345 \pm 4) \mu\text{m}$, or $(203 \pm 2) \mu\text{m}$ in FWHM, was measured.

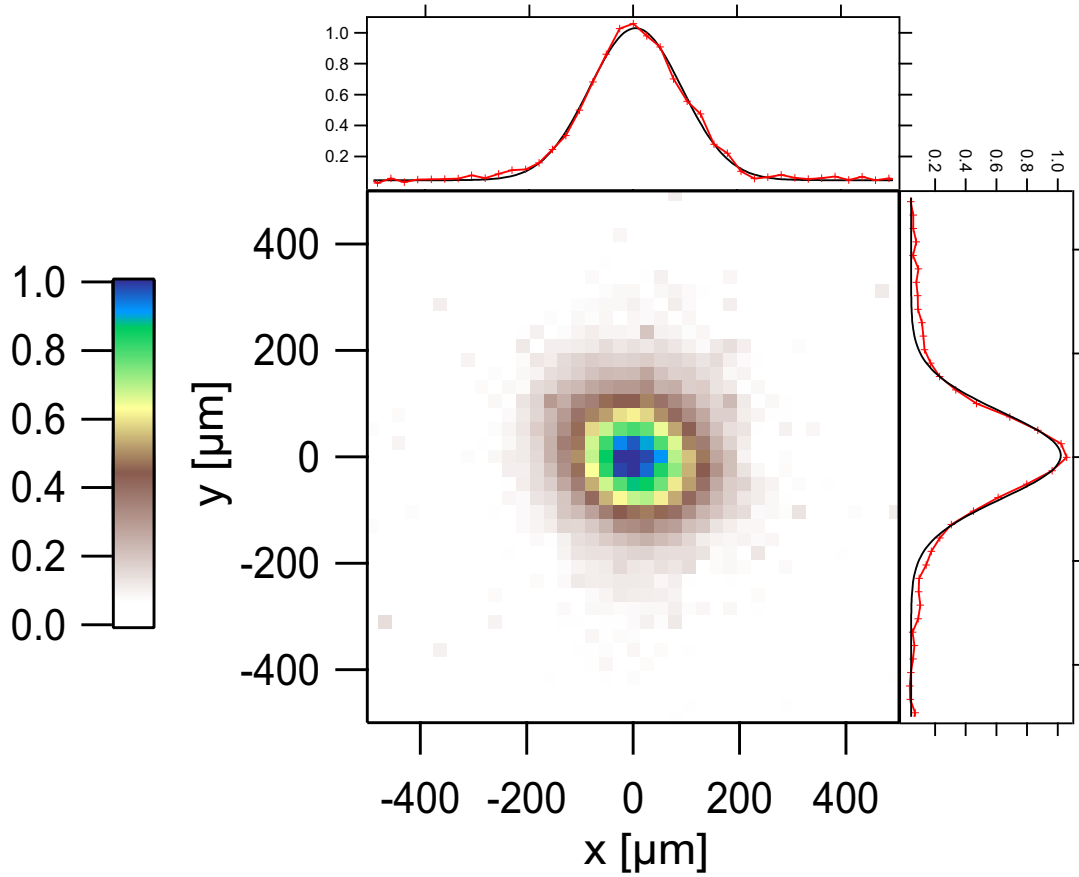


Figure 2.20: Focus of the 7th harmonic showing a $D4\sigma$ width of $(345 \pm 4) \mu\text{m}$ ($(203 \pm 2) \mu\text{m}$ FWHM). The horizontal and vertical line profiles are added. Measurement was performed with a MCP with phosphor screen and detected by a beam profiler.

Chapter 3

High-Repetition Rate XUV Photoelectron Spectroscopy and Future Implementations

The principle of photoelectron spectroscopy (PES) is based on an effect that was first discovered by Hertz [78], who observed, that electrons can be emitted from metallic surfaces when light was focused on it. Einstein interpreted this as being an effect of the quantum nature of light [79], which just occurs, when the energy of a single photon exceeds a material-dependent constant.

In solid state physics, the Fermi energy E_F is the most energetic state an electron can occupy, when the system is at ground-level, reached at 0 K. The binding energy E_B of electrons here is referred to E_F , with negative values for tighter bound states. For the photoemission of an electron, a photon is needed, whose energy $\hbar\omega$ is at least as high as the binding energy and a material- and surface-dependent work function ϕ , being the difference between E_F and the vacuum level [80]. Excess energy is carried by the electron as kinetic energy according to the formula:

$$E_K = \hbar\omega - E_B - \phi. \quad (3.1)$$

As can be seen from this equation, more strongly bound electrons have less kinetic energy. The electrons can be selected in kinetic energy and detected. Together with a known photon energy and work function, information about the binding energy can be gained. But these electron not only carry information about energies within a crystal. The electrons momentum vector \vec{k} can be separated into a perpendicular k_\perp and parallel component \vec{k}_\parallel with respect to the sample surface. During the process of the electron's transmission through the sample surface, \vec{k}_\perp is modified by the potential barrier and thus not conserved. In contrast, due to the constant crystal potential along the surface of the sample, \vec{k}_\parallel is conserved in the process of photo-emission [81]. The electrons are emitted within a cone and \vec{k}_\parallel is related to the polar emission angle θ by

$$\vec{k}_\parallel = \frac{1}{\hbar} \sqrt{2m_e E_K} \sin \theta \quad (3.2)$$

with the electron mass m_e . Thus, by measuring the electron emission as a function of angle, not only energy, but also the electron's crystal momentum information can be gained. Measuring angle-dependent photoelectrons is known as angle-resolved photoemission spectroscopy (ARPES) and provides information about the band structure of the investigated material.

Bound electrons can be excited into unoccupied states, when they are pumped with photons, which energy is not sufficient for photoemission but exceeds the band gap¹. Conventional ARPES without a pumping beam can not address non-equilibrium states. These states usually have a short lifetime and the electrons decay into lower energy levels again. But when simultaneously irradiated by a higher energetic XUV pulse (probe), these excited electrons can be photoemitted, containing information of band structures above the Fermi energy, which is highly interesting for the electrical properties of a material. This principle is referred as a pump/probe experiment.

When now the pump and probe pulses are delayed in time relative to each other, measurements of different steps of the time evolution of the process can be taken and thus dynamic phenomena investigated. This is called time-resolved ARPES (trARPES). This very powerful tool in our setup does not only allow to take movies of a process happening in the occupied states, but also of unoccupied states, which often only have $\approx 1\%$ of the density of occupied ones.

The XUV source's purpose is, to be a powerful, state-of-the-art tool in surface science for observations of the dynamic electron structures of solid state samples. The main focus of our trARPES facility with the HHG light source in the near future will be in the vastly growing interest in the field of transition metal dichalcogenides (TMDCs) [1, 2]. TMDCs are stacked, semiconducting materials, consisting of two-dimensional layers. As a bulk, these crystals exhibit inversion symmetry, whereas monolayers do not have this symmetry. As a consequence of reducing bulk of *e. g.* MoS₂ to a monolayer is the effect of a transition from an indirect into a direct band-gap, enhancing the light-emitting properties strongly, making it interesting *e. g.* as photodiodes [82]. Recently, it was shown, that monolayers of WSe₂ exhibit a spin-valley correlation of the band structure and this valley-selective electrons can be excited by circular polarized light [83, 84]. This paves the way for novel quantum electronic technologies. In multilayer or bulk samples, the bonding differs significantly. In-plane of a layer they are bound covalently. In contrast, the interlayer bonding is of van-der Waals interaction origin. This highly anisotropic bonding is very different to other 3D semiconductors such as Si or Ge.

We are interested in these fascinating characteristics of electronic structures and electron dynamics in such anisotropic materials and time-resolved ARPES can address and investigate these. Hence, WSe₂ is a good example to demonstrate the capabilities of the trARPES setup.

A more complete characterization of the XUV light source involves its application on such

¹Because of multi-photon processes, this can also occur with photon having less energy than an excitation over the band gap requires. But these effects are small in probability.

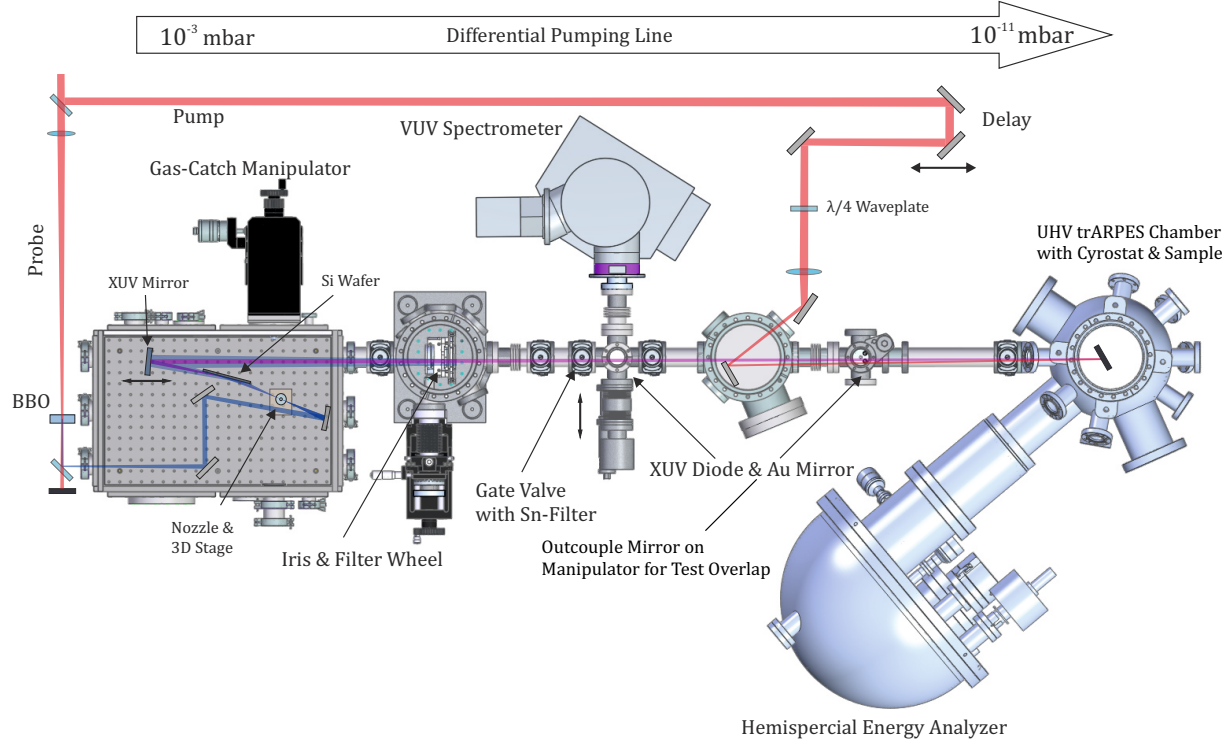


Figure 3.1: Beamline including the high-harmonics generation, its monochromatization, pump/probe pulses for trARPES, the sample and the hemispherical energy analyzer.

a sample, to investigate properties such as photon flux requirements, space-charge effects and its time-resolution. Before this was possible, the final beamline needed to be assembled and is described in the following section.

3.1 The trARPES Beamline

After the spot profile was characterized by the MCP measurement, the final setup was assembled. This beamline needs to fulfill following requirements: Enabling HHG in a dense rare gas jet, isolation of the 7th harmonic, maintaining ultra-high vacuum in the ARPES chamber, allowing time-resolved ARPES with a pump and probe pulse as well as the spectral and flux characterization of the XUV pulse.

In figure 3.1 an illustration of the actual beamline, which meets all these demands, is shown. The spectral monochromatization is achieved, as already explained in section 2.2.3, by separating the XUV from the UV with a silicon wafer at Brewster's angle, one concave-spherical XUV mirror and two thin metal filters. One of these filters is mounted in the filter wheel, while the second one is mounted in a gate valve. Another advantage of this filtering application is, that when the gate valve with the thin metal filter is fully closed, it also acts as a barrier for the noble gas, splitting the beamline into a high vacuum part

(HHG chamber) and an ultra-high vacuum section including the ARPES chamber. The beamline itself is pumped by two turbomolecular pumps, one with 260 ls^{-1} and another with 685 ls^{-1} nominal pumping speed for N_2 , both backed by a scroll pump. Hence, a pressure gradient of $1 \times 10^{-3} \text{ mbar}$ in the HHG chamber to the regime of 10^{-11} mbar is achieved during operation. The XUV flux can be measured with a XUV diode, mounted on a manipulator in such a way, that the diode can be inserted into the beam path. On the same mount is the incoupling mirror for the VUV spectrometer. For the sake of a better vacuum in the main beamline, the spectrometer can be separated by a gate valve and is pumped by a small turbomolecular pump with 67 ls^{-1} nominal pumping speed for N_2 . The pump pulse can be delayed in time with respect to the probe pulse by a retro-reflector, mounted on a motorized translation stage with a range of 150 mm to enable time-resolved scans. Before the pump beam enters the vacuum part of the beamline, it can be frequency doubled in a 100 μm thick type I BBO, which is not shown in 3.1 for the sake of a better clarity. Thus, pump photon energies of 1.55 eV and 3.1 eV are available. A achromatic $\lambda/4$ waveplate provides for a linear to circular pump polarization. Outside the vacuum chamber, the pump beam is focus with a $f = 1000 \text{ mm}$ lens and enters through a 1 mm thick CaF_2 window the vacuum part where it is reflected onto the sample via a rectangular mirror and as collinear to the probe beam as possible.

The sample itself is mounted a sample-holder, which is placed on a carving 6-axis manipulator, fully motorized by stepper motors and can be cooled down close to helium condensation temperature by a cryostat, see figure 3.2. These degrees of freedom in motion enable the scan in the reciprocal momentum space. The analyzer is a hemispherical PHOIBOS 150 analyzer. Both, the carving manipulator as well as the hemispherical analyzer are from SPECS Surface Nano Analysis GmbH. Following the description of [85, 86], the working principle of the analyzer is, that photoemitted electrons are focused in a system of electron lenses and retarded or accelerated towards an energy called the *pass energy*. In the hemisphere, the electrons are analyzed according to their energy by a radial electrostatic field within an inner and an outer hemisphere. Different operation modes of the electrostatic lenses allows for different acceptance angles of the photoelectrons. The detection unit is a MCP in combination with a phosphor screen, where the multiplied electrons are converted into a photon signal, which in turn can be detected by a CCD camera.

For finding the spatial overlap of the pump and probe pulse, there is a stripe of a fluorescent crystal attached to the carving manipulator, below the sample holder. This stripe can be observed by a camera, allowing for overlapping the pump and probe pulse. For the temporal overlap, both beams can be outcoupled from the vacuum beamline by a mirror on a manipulator before the ARPES chamber. In an equal distance from the mirror to the sample, a diode can be placed in this test overlap. With another diode, which gets the signal from a reflection from the OPCPA, triggers an oscilloscope. By either blocking the pump or probe pulse, both signals can be brought into the same delay with respect to the trigger and thus should temporally overlap at the sample. It turned out, that this method has a systematical error of $\approx 250 \text{ ps}$, but knowing this, one has a hint in which

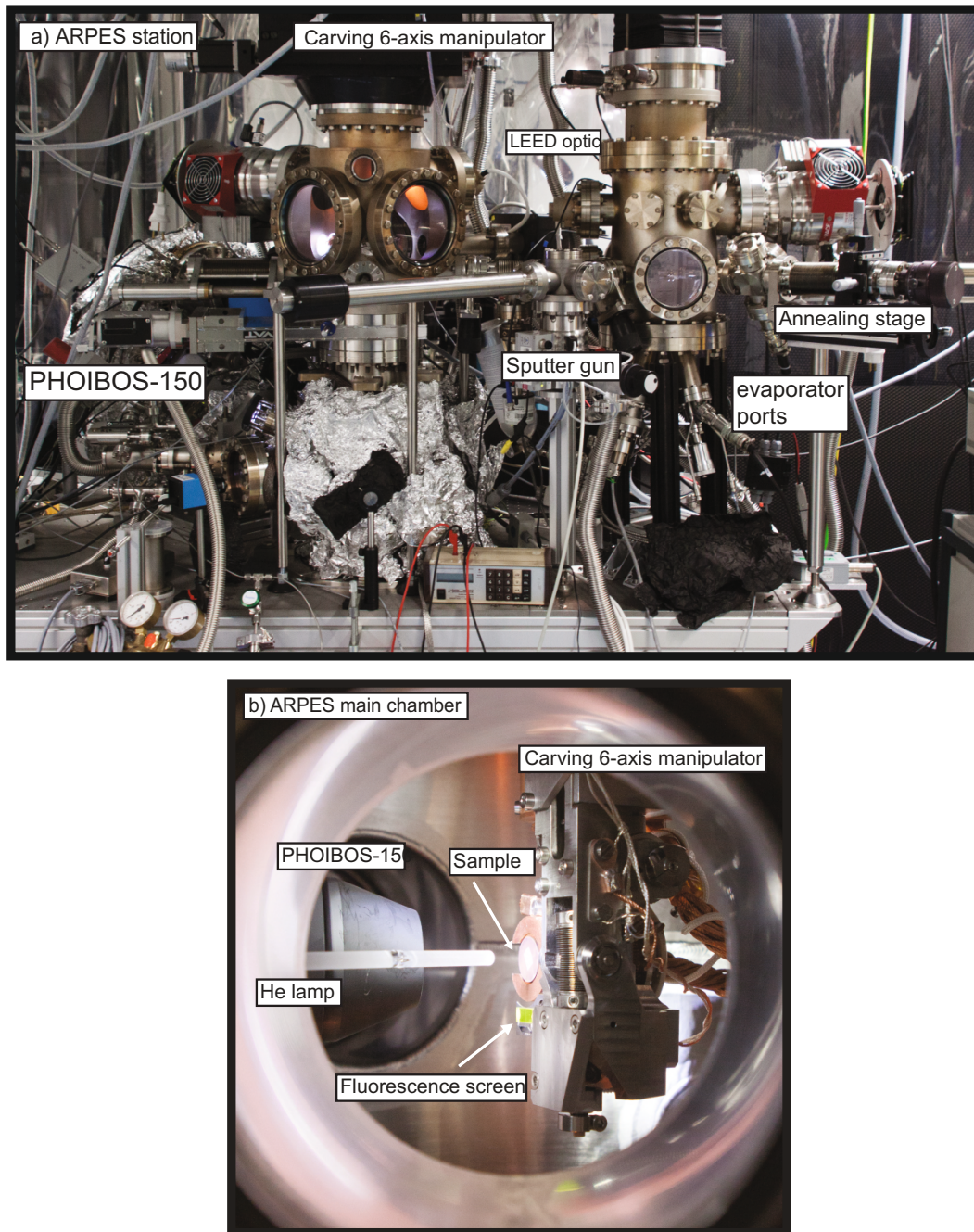


Figure 3.2: a) Shown is the ARPES station with the carving manipulator, the hemispherical energy analyzer PHOIBOS 150 and the sample-preparation chamber, including evaporation ports equipped with different metals, a sputter gun, an annealing stage as well as a low energy electron diffraction (LEED) optic. b) Close-up of the main chamber. The sample holder and the fluorescence screen for the pump-probe overlap are mounted on the carving 6-axis manipulator. Next to the entrance lens of the PHOIBOS 150 is a helium lamp for static, high energy resolution measurements.

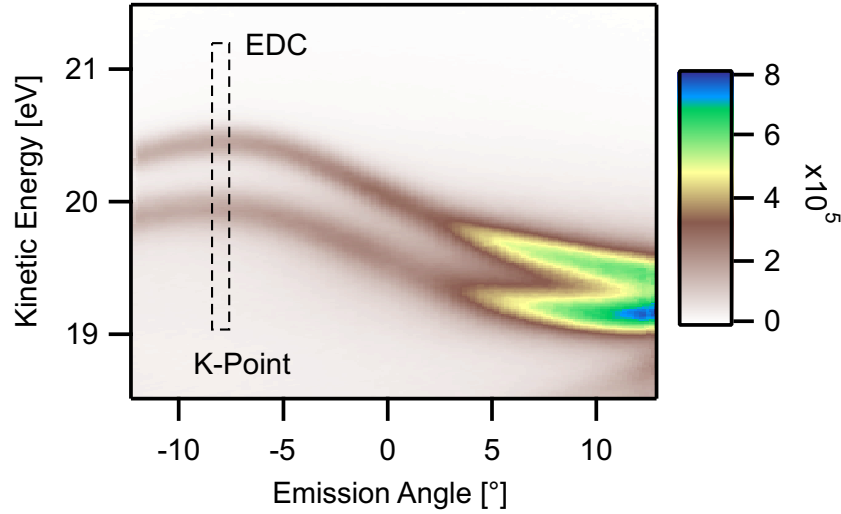


Figure 3.3: Static ARPES measurement on bulk WSe₂. The top two valence bands as a function of the crystal momentum k_{\parallel} clearly can be resolved. The rectangle shows the cut of the EDCs, investigated in 3.4 a) and b).

regime the fine tuning can be done by direct observation of the PES signal.

3.2 ARPES and Space-Charge Effects

One of the first measurements which were done with the new high-repetition rate XUV light source, was static ARPES on bulk WSe₂. This material has a maximum of the top two valence bands at the K-point² [82]. As figure 3.3 shows, these two momentum-dependent bands can be well resolved and distinguished from each other. In energy, they are separated by ≈ 0.5 eV. The measurement was performed at room temperature and with only 60 s acquisition time, showing how fast a reasonable spectrum can be acquired with the 500 kHz light source and the achieved counting rate. The higher the XUV flux is, the higher is the counting rate. In this connection, one needs to observe if a good regime of counts is reached. By 'good' is as high as possible counting rate meant, before space-charge effects start to influence the spectrum. This is the limit of XUV flux which wants to be applied. The investigation of the occurrence of such effects is done in the following.

Cuts along a fixed emission angle in figure 3.3 provide energy distribution curves (EDCs). At the K-point, EDCs of the top two valence bands were investigated as a function of XUV flux. Figure 3.4 a) displays these EDCs with normalized intensities. With an increasing XUV flux, an obvious shift of the bands towards higher energies can be seen. A more detailed investigation of the energy for the peaks of both bands can be found in figure 3.4

²The K-point are the corners of the first hexagonal Brillouin zone.

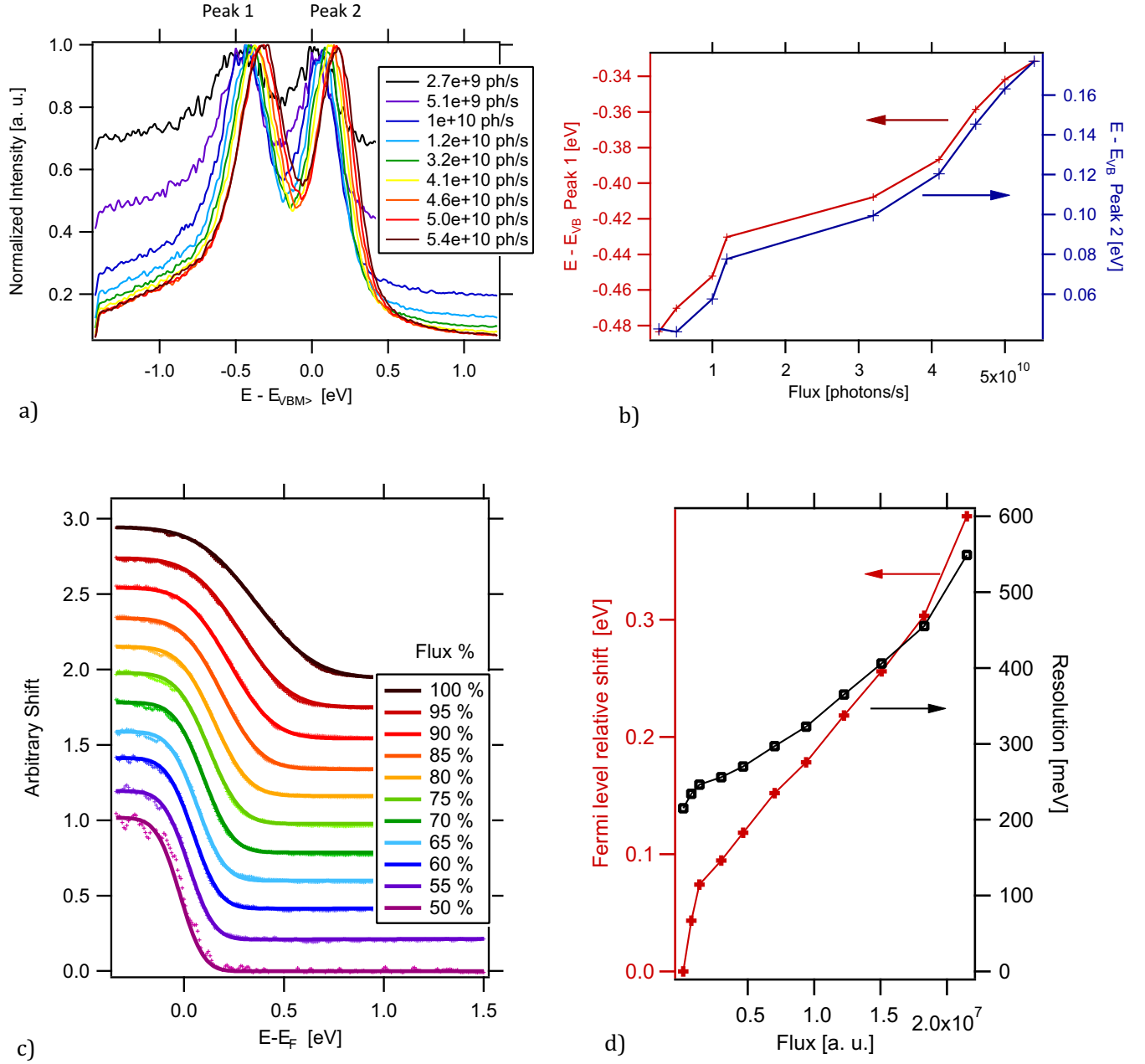


Figure 3.4: a) EDCs of WSe₂ at the K-point as a function of XUV flux. The top two valence bands reveal a shift towards higher energies with an increasing XUV flux. b) Both valence band peaks show energy shifts with a similar response to the XUV flux. c) The Fermi edge of a polycrystalline gold surface at 77 K shows a strong broadening because of space-charge effects, induced to an increased XUV flux. d) Broadening and shift of the Fermi edge as a function of XUV flux.

b). Both band shifts are affected by an increased photo-flux in the same way. The highest flux in this investigation is 20 times the lowest flux. In this range, a shift of ≈ 140 meV occurs.

An explanation for this is the effect of the space-charge. With each XUV pulse, many electrons are photoemitted, forming an electron cloud in front of the sample surface. During this process, the majority of electrons scatter *e. g.* with other electrons or phonons and thus lose kinetic energy, or were emitted from a tighter bound state, resulting in less kinetic energy. Electrons are repelled from each other due to their Coulomb interactions. The small fraction that made it into the vacuum state without scattering, is selected and detected by the analyzer. In general, these are the electrons of interest for ARPES measurements. Since these electrons feel the repulsive force of many slower electrons coming from the sample direction, they are accelerated to even higher kinetic energies. This results in the detected energy shift, growing in strength, the more electrons are photoemitted. But changes in energy do not only happen towards higher energies. The detected electrons also repel each other and thus alter their kinetic energy in each direction, leading to energetic broadening and thus loss of energy resolution. A more detailed research on space-charge can be found in reference [6].

This broadening was also investigated with a polycrystalline gold film, cooled with liquid nitrogen to 77 K, where a clear Fermi edge is expected. A clear broadening of the Fermi edge was observed, as figure 3.4 c) shows. The vertical shift in the plot is just for a better clarity and does not have a physical meaning. In figure 3.4 d), the broadening of the edge and the shift towards higher energies is plotted. The shift shows the same response to higher XUV fluxes as for WSe₂. The width (measured as the 10/90 rise) is the smallest for the lowest applied XUV flux and increases monotonously with it, as expected. This behavior can not be explained by a changed bandwidth of the XUV pulse, where a decrease is noticed when going to 100% OPCPA power, compare figure 2.16. Hence, the reduction in energy resolution, which was observed in the applied flux regime, comes along with an increased space-charge effect.

For our XUV source, the conclusion can be drawn, that we have enough flux for the current used samples, since space-charge effects are the limiting factor in energy resolution. To yield best results in energy resolution, an attenuation of the XUV flux to a minimum counting rate should be done. Therefor, an attenuation with the aperture in the filter-wheel chamber provides the best possibility, since this does not affect the XUV's bandwidth.

3.3 Temporal Resolution with LAPE

The investigation of dynamics in electronic structures requires a pulse which excites electrons (pump pulse) into formally unoccupied states, from where they relax towards the Fermi level. A second, high energetic pulse, the probe pulse, is used to photoemit those excited electrons to take a snapshot from the current state. Time-delaying one of the pulses (usually

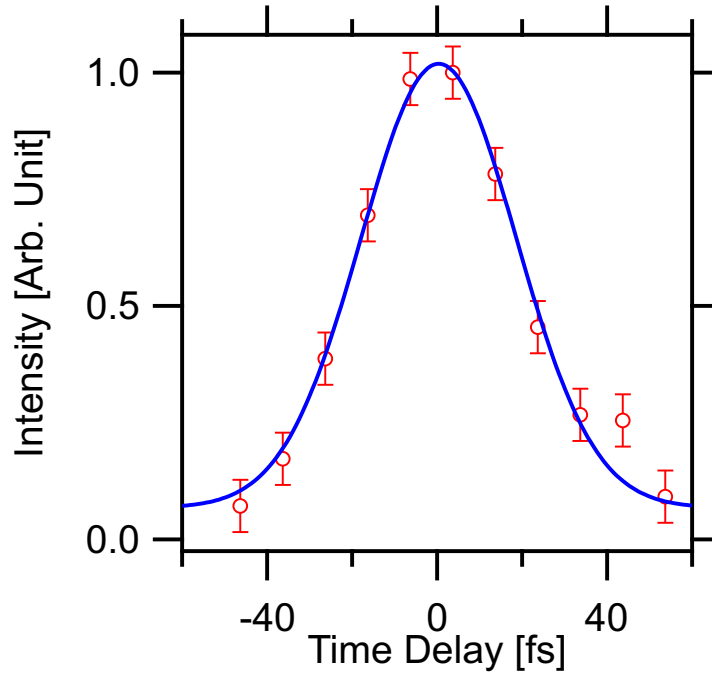


Figure 3.5: Cross-correlation of the pump and probe pulse, achieved with the laser-assisted photoelectric effect, yielding a FWHM temporal resolution of (43 ± 2) fs.

the pump pulse) allows to trace the evolution of these excited states. Since our delay-stage (Newport GTS150) allows sub-femtosecond resolution, the determining factors for the achievable temporal resolution are the pulse durations of the pump and probe pulse. A good method to measure the cross-correlation of pump and probe pulse uses the laser-assisted photoelectric effect (LAPE) [87]. The first demonstration on solid state surfaces was done by Miaja-Avila et al. [88].

With LAPE, the photoemission spectrum shows separated sidebands from the main photoemission peak. In energy, these sidebands are separated by the pump photon energy $\hbar\omega$. The photoemitted electrons, situated in the continuum state, are modulated in energy by the pump light field. Regarding the relative phase, this results in higher and lower kinetic energies. Determining the amplitudes of the sidebands for different pump-probe delays, yields a system response function, which contains information about the time-resolution achievable with these pulses.

Such a measurement was done on TiSe_2 and is depicted in figure 3.5. The obtained signal is a cross-correlation of the pump and probe pulse. A Gaussian fit of the cross-correlation yields a FWHM temporal resolution of (43 ± 2) fs. Before this measurement, the pump pulse was characterized by a FROG measurement in FWHM pulse duration of about 35 fs. The prism compressor was then optimized for a maximal two-photon photoemission of the pump pulse on the sample, allowing the assumption, that minimum pulse duration of the pump pulse is achieved at the sample. To reproduce the temporal system response function,

the assumed pump pulse with a FWHM of 35 fs and a Gaussian profile, was convoluted with another Gaussian pulse, representing the probe pulse. With a FWHM input parameter of ≈ 20 fs for the probe pulse, a similar function as experimentally achieved could be generated. Cross-checking this with the calculated time-bandwidth product for the 7th harmonic with a FWHM in energy of 105 meV, yields a minimum pulse duration of ≈ 18 fs for the assumed Gaussian pulse, which is in good agreement with the estimated XUV pulse duration.

3.4 Time-resolved ARPES on WSe₂

Monolayers of WSe₂ have a direct band gap at the K-point. Transitions of electrons into unoccupied states at this point can be resonantly pumped with our 1.55 eV pump beam. Figure 3.6 a) and b) show this. A clear signal of the occupied states at the K-valley can be seen. But also at the Σ -point³, which can not be occupied by the pump pulse, since the k-momentum of photons is too small for indirect transitions and three-particle processes involving an additional phonon are too unlikely for such a strong signal.

Delaying the pump pulse with respect to the probe in time, enables a dynamical investigation of this process. Such a scan with steps in 10 fs is shown figure 3.6 c). This reveals, that electrons in the K-valley scatter very fast, within a couple of tens of femtoseconds, into other states. In contrast, the Σ -valley is the minimum of the conduction band, where only recombination with holes are possible. These are much slower processes.

These experiments represent only a first proof-of-principle, but demonstrate well the wealth of information about the carrier relaxation pathways and the redistribution of energy in such a system, that can be gained by the XUV trARPES setup directly on a femtosecond timescale.

³The Σ -point is in the middle of the K-point to the Γ -point (center of the Brillouin zone) in a hexagonal first Brillouin zone.

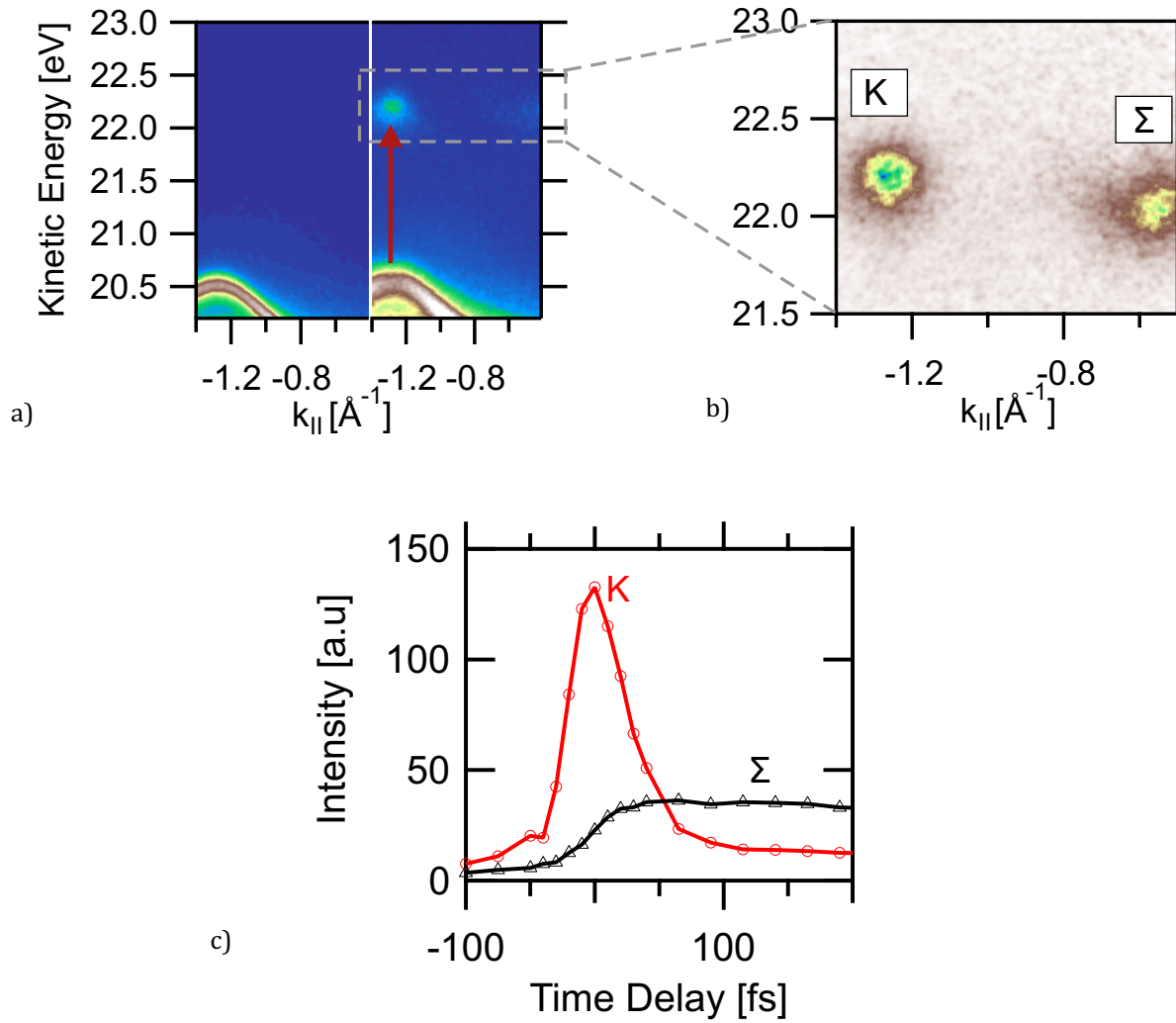


Figure 3.6: a) and b): Excitation of unoccupied states in the K-valley of resonant pumping at 1.55 eV in comparison with static ARPES from a He lamp, where no occupied states can be observed. Time-resolved scans show very fast processes in c).

3.5 NOPA as Pump Source

For an efficient excitation of electrons into unoccupied states, photons with the right energy are needed to overcome the band gap. In case of WSe₂ and 1.55 eV pump photon energy, this is fulfilled around the K-point. But as the calculated band structure of WSe₂ by Riley et al. [3] in figure 3.7 shows, different k-values require different pumping energies, especially towards higher photon energies compared to the 800 nm pump. Also other materials might require another pumping wavelength.

For this reason, it is desired to have a pump light source which covers the whole visible spectrum. In order to achieve this, the implementation of a noncollinear optical parametric amplifier (NOPA) in the pump beam was tested.

After a brief introduction to the theory of the working principle of a NOPA was done in section 1.2.5. The realization of this implementation and first results will be shown here.

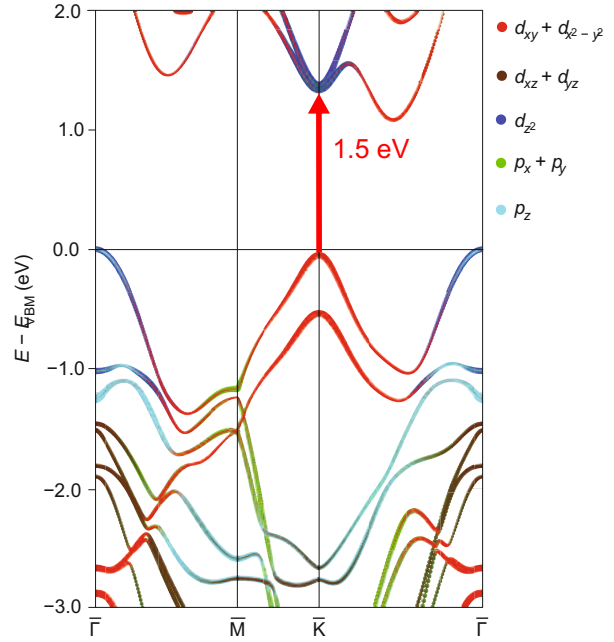


Figure 3.7: Calculated band structures of WSe₂, showing a direct band gap at the K-point, which can be pumped with 800 nm. Figure adopted from [3].

3.5.1 Experimental Challenges and Realization

The PES pump source we want should be allow for selective resonant excitation of unoccupied states and tunable across the visible spectrum. Because the pump photons of the NOPA need to have more energy than the signal photons which should be amplified, a 400 nm beam serves just fine, since it is from the high energetic end of the visible spectrum and can be easily achieved by frequency doubling of our OPCPA beam. The pulse duration of the NOPA output should be around 40 fs, which requires an amplified bandwidth of $\Delta\lambda \approx 15$ nm, depending on the central wavelength.

In the pump-probe experiment, the pump needs to overlap with the probe temporally, thus using the same 500 kHz source for the NOPA as for the HHG is convenient. The idea was, to use the remaining part of the 800 nm, which is not frequency doubled in the SHG stage in front of the HHG chamber. In turn, the signal beam should be generated by

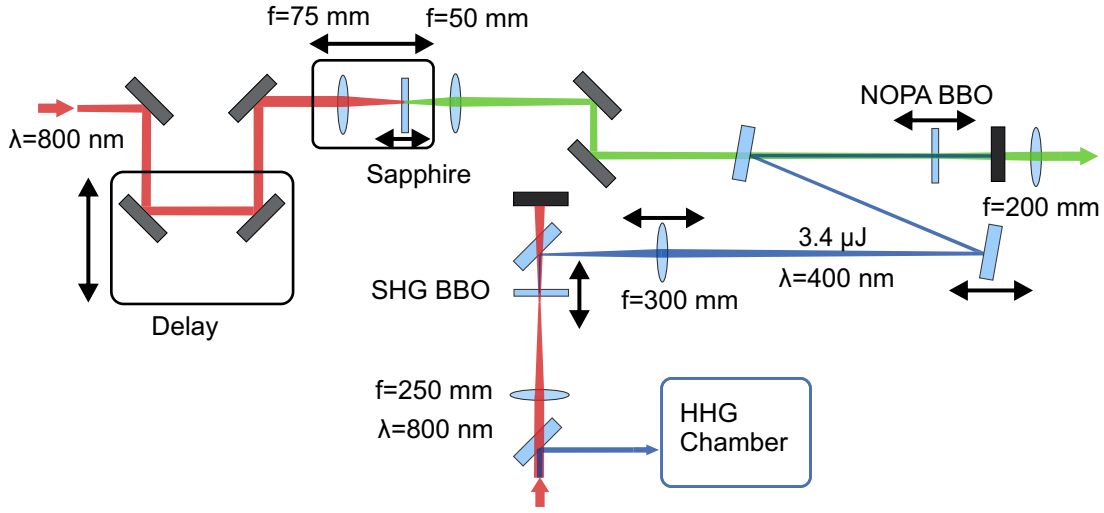


Figure 3.8: Implementation of a NOPA into the pump beam of the trARPES setup. The initial pump generates a supercontinuum, acting as the NOPA signal, whilst the residual 800 nm from the probe SHG is separated and again frequency doubled. This beam is supposed to be the NOPA pump.

supercontinuum generation, driven by the currently used 800 nm trARPES pump beam. Using those beams is challenging, since they already experienced several nonlinear stages and strong phase degeneration is expected. In addition, long beam paths increase pointing instabilities. Another requirement for the NOPA is, to be as compact as possible, because temporal overlap with the XUV at the sample is necessary.

The NOPA setup we aimed for follows the design considerations done by Piel et al. [91] with slight modifications. A scheme of our setup is depicted in figure 3.8. For an efficient amplification, a peak intensity of $>100 \text{ GW/cm}^2$ is needed [91], demanding for a high intense pump beam. After the SHG in the probe arm, the residual 800 nm beam is separated from the frequency doubled part by a 45° dichroic mirror in transmission. This beam is focused with a $f = 250$ mm fused silica (FS) lens close before a $100 \mu\text{m}$ thick type I BBO for SHG, yielding $3 \mu\text{J}$ of 400 nm with a FWHM bandwidth of 7 nm. Piel et al. suggests to recollimate the pump beam with a lens and finally focusing it with a concave mirror into the NOPA crystal. In order to avoid aberration effects from a spherical mirror, the pump is focused, after separating it from the residual 800 nm by a dichroic mirror, with a single $f = 300$ mm FS lens, mounted on a translation stage for tuning the focus position at the NOPA crystal. In order to achieve the noncollinearity angle of 3.7° in the nonlinear crystal (compare with figure 1.5 where the same input parameters are used as in our setup) the pump beam height is lowered with respect to the signal beam and the noncollinearity angle is achieved vertically, whilst in horizontal direction, pump and signal propagate collinear in front of the NOPA crystal. After the focusing lens, two high-reflective 0° dielectric mirrors reflect the pump into the nonlinear crystal. The first mirror is mounted

on a translation stage for fine-tuning the spot size on the crystal, while the last mirror directs the pulse into a vertical displacement for intersecting with the signal at the crystal position with an internal angle of $\alpha = 3.7^\circ$. The NOPA crystal is a 2 mm thick type I BBO, cut for an phase-matching angle of $\theta_m = 31.3^\circ$ with a protective coating. The difference in phase-matching angles compared to the one described by Cerullo [17] of the defined reference beam. In our case, the signal is considered to be normal to the crystal's surface, not the pump, in order to avoid spatial dispersion effects of the broadband signal.

This broadband signal is generated with 130 nJ at 800 nm after a mode-cleaning aperture and focusing with a $f = 75$ mm FS lens into a 3 mm thick sapphire disk. The high diverging supercontinuum is recollimated with a $f = 50$ mm FS lens. The sapphire disk is mounted on a translation stage, which in turn is mounted on a bigger translation stage, together with the focusing mirror. This allows adjustments for a stable single-filament supercontinuum generation and adjusting the spot size in the NOPA crystal. Before this crystal, the beam is displaced horizontally with two mirrors, which allows for an easy spatial adjustment of the signal beam on the NOPA crystal.

An additional advantage of the NOPA is, that due to the noncollinearity, no further beam separation of the amplified signal is needed.

3.5.2 First Results

The experimental part for this thesis ended with the proof of principle, that amplification can be achieved in a NOPA setup, described in the previous section. Such an amplification could be found. The achieved spot profiles of pump and signal are depicted in the left picture of figure 3.9. The profiles were taken with a beam profiler at the position of the NOPA BBO. A $D4\sigma$ width of 0.24 mm and 0.23 mm was determined for the pump and signal, respectively. Taking two lenses, the beam splitter and the BBO into account, an assumed pulse duration of 80 fs for the pump and thus a peak intensity of 1.9×10^{11} W/cm² is reached, being sufficient for amplification. Placing the beam profiler at the exact position of the NOPA BBO was hard, that is way the spatial overlap was done with a 10 μ m wide slit, which could be mounted in the rotation stage, where the BBO is mounted, and thus allowing the slit being located at the right position. In the right picture of figure 3.9 the diffraction pattern for both beams are overlap and thus in the right horizontal position. This method proved to be very precise and easy in use. No further adjustment was necessary as soon as the temporal overlap was found as well. Latter was done by the same method, including an OPCPA triggered diode, as described in section 3.1 for the trARPES overlap. A spectrum of the supercontinuum, generated in a 3 mm thick disk of sapphire with 130 nJ at 800 nm, is shown in figure 3.10. Filtering the intense fundamental with a 700 nm low-pass filter, a stable supercontinuum energy per pulse of (4.22 ± 0.02) nJ at 500 kHz was measured.

Also in figure 3.10, the first amplified spectrum, without low-pass filter is shown. It shows an amplification bandwidth of ≈ 50 nm, which proves, that the white-light does not need to be further stretched, but a bit shorter pump pulse would improve the situation a bit. This can be achieve by using thinner lenses and a thinner dichroic mirror.

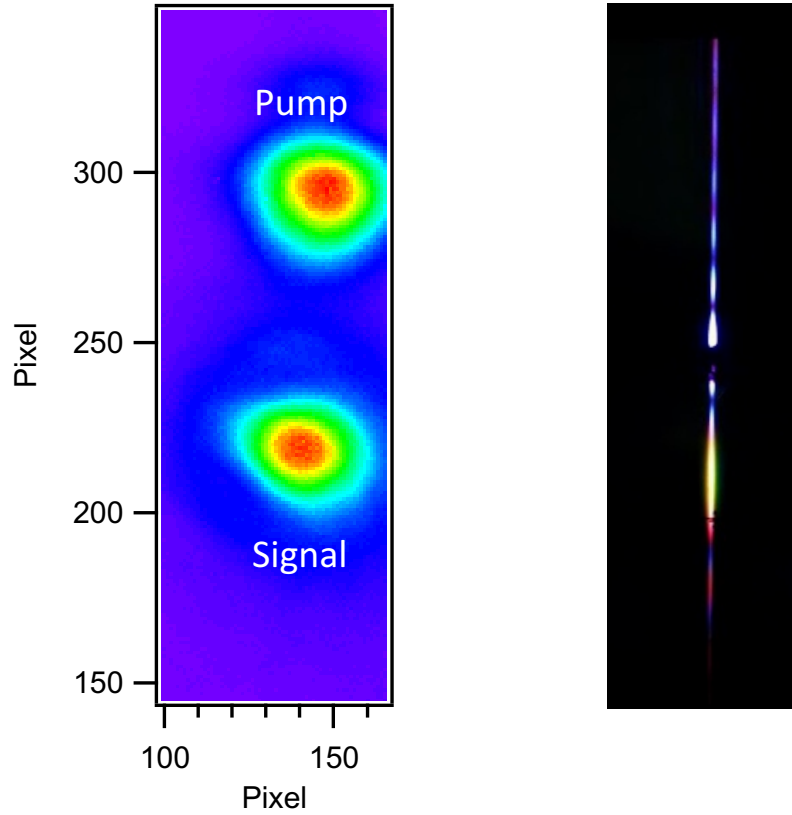


Figure 3.9: *Left)* With a beam profiler investigated spot profiles of pump and signal at the nonlinear crystal position. The pump has a $D4\sigma$ width of 0.24 mm and the signal 0.23 mm. *Right)* Finding the spatial overlap in horizontal direction of pump and signal with a $10\text{ }\mu\text{m}$ slit mounted in the NOPA BBO mount. The overlap is found, when both diffraction pattern occur in the same horizontal position, as shown in the picture.

It could be shown, that amplification achieved by a NOPA in the trARPES pump arm is possible. Besides fine-tuning the phase-matching angle for a more efficient amplification, modifications in the beam path should be done. Before the SHG BBO, the NOPA pump is adjusted in height by a periscope, but it also changes the propagation direction by 90° with respect to the initial path. Thus, variations in beam pointing before the separation into pump and probe beams result in walk-offs into different directions, leading to a reduced spatial overlap in the NOPA BBO and thus a lowered and instable amplification. After a strong and stable enough amplification can be generated, the signal pulse needs to be compressed in time, to compensate the linear chirp. This can be done in a prism compressor [92]. In order to preserve time-overlap of the pump and probe on the sample, also the probe path needs to be modified.

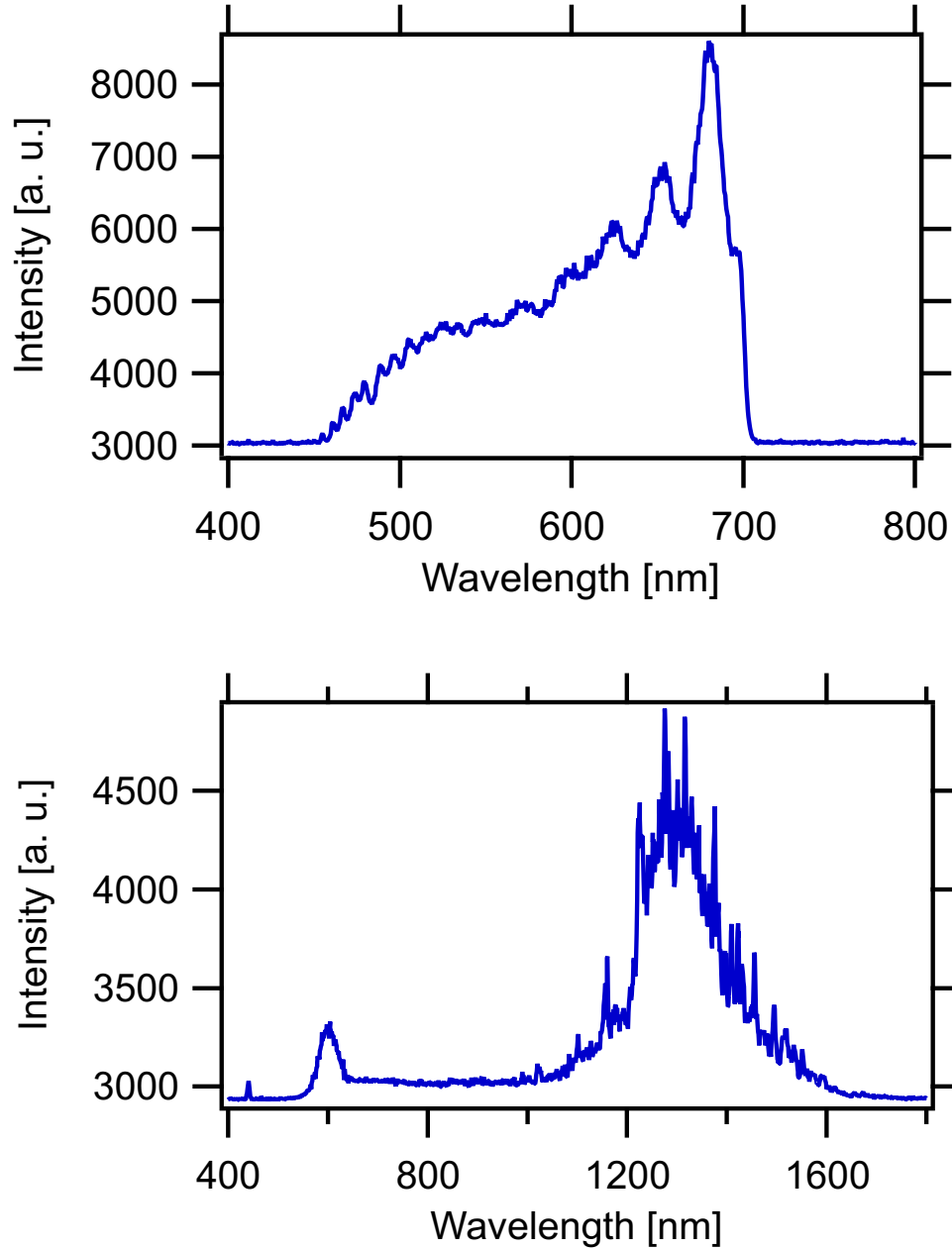


Figure 3.10: *Top*) Spectrum of the supercontinuum, generated in a 3 mm thick sapphire disk with 130 nJ at 800 nm. It reaches from 460 nm to 700 nm. The cut-off and the fringe-like modification of the spectrum is caused by the use of a 700 nm low-pass filter. *Bottom*) Spectrum of the first amplification in the NOPA. Spectrum was taken without the 700 nm low-pass filter.

Chapter 4

Summary

Within the framework of this thesis, it was possible to establish a 500 kHz high-repetition rate XUV light source for trARPES measurements. A novel designed all ytterbium-based fiber-slab combination, pumping an OPCPA laser system with frequency doubled output was used for high harmonic generation. The challenges of an efficient HHG with low pulse energies resulting from such a high-repetition rate system were faced by tight focusing conditions. In order to achieve phase-matching, high backing pressures of a few bars were needed. To overcome the arising problem of XUV reabsorption and a too high gas load on the vacuum pumping system, a gas-catch was constructed and installed, enabling us the long term stable application of up to 6 bar backing pressure.

Spectral filtering with a contrast of 2.6×10^{-4} was achieved by the use of a silicon wafer at Brewster's angle, a XUV mirror with a special tailored reflectivity and a thin Sn metal foil. Latter also acts as a differential pumping barrier, allowing for base pressures in the ARPES chamber while operation below 10^{-10} mbar. The 7th harmonic of a 400 nm driving laser was selected, allowing for the investigation of the full Brillouin zone due to its 21.7 eV photon energy. A 7th's harmonic bandwidth of (105 ± 8) meV was measured by a VUV spectrometer. Very high conversion efficiencies from the driving laser to the 7th harmonic of 3×10^{-5} could be generated, proving the theory, that similar conversion efficiencies can be achieved with tight focusing compared to loose focusing. This corresponds to a photon flux of $(1.02 \pm 0.07) \times 10^{12}$ photons/s on the sample. To our surprise, the highest flux was generated in an argon jet, making this XUV source very cost efficient.

After assembling the beamline, flux dependent measurements on WSe₂ and polycrystalline gold revealed that the photon flux is more than enough and space-charge effects are the limiting factors for the maximal applicable flux. This means, we can reach the optimum compromise of counting statistics and energy resolution, which is accessible for this repetition rate. Time-resolved ARPES measurements showed, that our facility is capable of tracing time dependent processes, not just of occupied states, but also unoccupied ones with low electron density.

For the future development of the beamline, a NOPA as pump source was in discussion. A proof of concept test amplifier was built, which achieved amplification by recycling the fundamental beam after SHG. For a more efficient amplification, more stability is needed,

which could be gained with another beam path, that signal and pump beams experience equal beam pointings in the NOPA BBO.

Bibliography

- [1] A. K. Geim and I. V. Grigorieva. Van der Waals heterostructures. *Nature*, 499(7459):419–425, 2013.
- [2] K. S. Novoselov, D. Jiang, F. Schedin, T. J. Booth, V. V. Khotkevich, S. V. Morozov, and A. K. Geim. Two-dimensional atomic crystals. *Proceedings of the National Academy of Sciences of the United States of America*, 102(30):10451–10453, 2005.
- [3] J. M. Riley et al. Direct observation of spin-polarized bulk bands in an inversion-symmetric semiconductor. *Nature Physics*, 10(11):835–839, 2014.
- [4] S. Mathias, L. Miaja-Avila, M. M. Murnane, H. Kapteyn, M. Aeschlimann, and M. Bauer. Angle-resolved photoemission spectroscopy with a femtosecond high harmonic light source using a two-dimensional imaging electron analyzer. *Review of Scientific Instruments*, 78(8):8, 2007.
- [5] B. Frietsch, R. Carley, K. Dobrich, C. Gahl, M. Teichmann, O. Schwarzkopf, P. Wernet, and M. Weinelt. A high-order harmonic generation apparatus for time- and angle-resolved photoelectron spectroscopy. *Review of Scientific Instruments*, 84(7):10, 2013.
- [6] S. Hellmann, K. Rossnagel, M. Marczyński-Buhlow, and L. Kipp. Vacuum space-charge effects in solid-state photoemission. *Physical Review B*, 79(3):12, 2009.
- [7] Rick Trebino. *Frequency-Resolved Optical Gating: The Measurement of Ultrashort Laser Pulses*. Springer US, Boston, MA, 2000.
- [8] Jean-Claude Diels. *Ultrashort laser pulse phenomena fundamentals, techniques, and applications on a femtosecond time scale*. Optics and photonics. Elsevier/Academic Press, Burlington, MA, 2nd ed edition, 2006.
- [9] Paul N Butcher and David Cotter. *The elements of nonlinear optics*, volume 9. Cambridge university press, 1991.
- [10] L. F. Mollenauer, R. H. Stolen, and J. P. Gordon. Experimental-Observation of Picosecond Pulse Narrowing and Solitons in Optical Fibers. *Physical Review Letters*, 45(13):1095–1098, 1980.

- [11] A. Schiffrin, T. Paasch-Colberg, N. Karpowicz, V. Apalkov, D. Gerster, S. Muhlbrandt, M. Korbman, J. Reichert, M. Schultze, S. Holzner, J. V. Barth, R. Kienberger, R. Ernstorfer, V. S. Yakovlev, M. I. Stockman, and F. Krausz. Optical-field-induced current in dielectrics (vol 70, pg 493, 2013). *Nature*, 507(7492):386–387, 2014.
- [12] E. Goulielmakis, M. Schultze, M. Hofstetter, V. S. Yakovlev, J. Gagnon, M. Uiberacker, A. L. Aquila, E. M. Gullikson, D. T. Attwood, R. Kienberger, F. Krausz, and U. Kleineberg. Single-Cycle Nonlinear Optics. *Science*, 320(5883):1614–1617, 2008.
- [13] P. A. Franken, G. Weinreich, C. W. Peters, and A. E. Hill. Generation of Optical Harmonics. *Physical Review Letters*, 7(4):118, 1961.
- [14] T. H. Maiman. Stimulated Optical Radiation in Ruby. *Nature*, 187(4736):493–494, 1960.
- [15] Robert W. Boyd. *Nonlinear optics*. Academic Press, Burlington, MA, 3rd ed edition, 2008.
- [16] Valentin G. Dmitriev. *Handbook of Nonlinear Optical Crystals*. Springer Series in Optical Sciences. Springer Berlin Heidelberg, Berlin, Heidelberg, third revised edition edition, 1999.
- [17] Giulio Cerullo and Sandro De Silvestri. Ultrafast optical parametric amplifiers. *Review of Scientific Instruments*, 74(1):1–18, 2003.
- [18] R. R. Alfano and S. L. Shapiro. EMISSION IN REGION 4000 TO 7000 Å VIA 4-PHOTON COUPLING IN GLASS. *Physical Review Letters*, 24(11), 1970.
- [19] S. Uhlig. *Self-Organized Surface Structures with Ultrafast White-Light*. Springer Spektrum, 2015.
- [20] A. McPherson, G. Gibson, H. Jara, U. Johann, T. S. Luk, I. A. McIntyre, K. Boyer, and C. K. Rhodes. Studies of Multiphoton Production of Vacuum-Ultraviolet Radiation in the Rare Gases. *Journal of the Optical Society of America B-Optical Physics*, 4(4): 595–601, 1987.
- [21] L.V. Keldysh. IONIZATION IN THE FIELD OF A STRONG ELECTROMAGNETIC WAVE. *Zh. Eksperim. i Teor. Fiz.*, 1964.
- [22] P. B. Corkum. PLASMA PERSPECTIVE ON STRONG-FIELD MULTIPHOTON IONIZATION. *Physical Review Letters*, 71(13):1994–1997, 1993.
- [23] M. Lewenstein, P. Balcou, M. Y. Ivanov, A. Lhuillier, and P. B. Corkum. THEORY OF HIGH-HARMONIC GENERATION BY LOW-FREQUENCY LASER FIELDS. *Physical Review A*, 49(3):2117–2132, 1994.

- [24] Carsten Winterfeldt, Christian Spielmann, and Gustav Gerber. Optimal control of high-harmonic generation. *Rev. Mod. Phys.*, 80:117–140, 2008.
- [25] M. J. DeWitt and R. J. Levis. Calculating the Keldysh adiabaticity parameter for atomic, diatomic, and polyatomic molecules. *Journal of Chemical Physics*, 108(18):7739–7742, 1998.
- [26] M. V. Ammosov, N. B. Delone, and V. P. Krainov. TUNNEL IONIZATION OF COMPLEX ATOMS AND ATOMIC IONS IN A VARYING ELECTROMAGNETIC-FIELD. *Zhurnal Eksperimentalnoi I Teoreticheskoi Fiziki*, 91(6):2008–2013, 1986.
- [27] C. Heyl. High-Order Harmonic Generation at 100 kHz Repetition Rate for Time-Resolved Two-Photon Photoemission. Diplomarbeit, Philipps-Universität Marburg, 2010.
- [28] T. Popmintchev, M. C. Chen, P. Arpin, M. M. Murnane, and H. C. Kapteyn. The attosecond nonlinear optics of bright coherent X-ray generation. *Nature Photonics*, 4(12):822–832, 2010.
- [29] C. J. Lai, G. Cirimi, K. H. Hong, J. Moses, S. W. Huang, E. Granados, P. Keathley, S. Bhardwaj, and F. X. Kartner. Wavelength Scaling of High Harmonic Generation Close to the Multiphoton Ionization Regime. *Physical Review Letters*, 111(7):5, 2013.
- [30] H. Wang, Y. M. Xu, S. Ulonska, J. S. Robinson, P. Ranitovic, and R. A. Kaindl. Bright high-repetition-rate source of narrowband extreme-ultraviolet harmonics beyond 22 eV. *Nature Communications*, 6:7, 2015.
- [31] C. Winterfeldt. *Generation and control of high-harmonic radiation*. PhD thesis, Julius-Maximilians-Universität Würzburg, 2006.
- [32] Bahaa E. A. Saleh and Malvin Carl Teich. *Fundamentals of photonics*. Wiley series in pure and applied optics. Wiley, Hoboken, NJ, 2nd ed edition, 2007.
- [33] S. M. Feng and H. G. Winful. Physical origin of the Gouy phase shift. *Optics Letters*, 26(8):485–487, 2001.
- [34] X. F. Li, A. Lhuillier, M. Ferray, L. A. Lompre, and G. Mainfray. MULTIPLE-HARMONIC GENERATION IN RARE-GASES AT HIGH LASER INTENSITY. *Physical Review A*, 39(11):5751–5761, 1989.
- [35] P. Balcou, P. Salieres, A. Lhuillier, and M. Lewenstein. Generalized phase-matching conditions for high harmonics: The role of field-gradient forces. *Physical Review A*, 55(4):3204–3210, 1997.
- [36] Anne L’Huillier. *High-Order Harmonic Generation and Attosecond Light Pulses: An Introduction*. Wiley-VCH Verlag GmbH and Co. KGaA, 2014.

- [37] S. Eich, A. Stange, A. V. Carr, J. Urbancic, T. Popmintchev, M. Wiesenmayer, K. Jansen, A. Ruffing, S. Jakobs, T. Rohwer, S. Hellmann, C. Chen, P. Matyba, L. Kipp, K. Rossnagel, M. Bauer, M. M. Murnane, H. C. Kapteyn, S. Mathias, and M. Aeschlimann. Time- and angle-resolved photoemission spectroscopy with optimized high-harmonic pulses using frequency-doubled Ti:Sapphire lasers. *Journal of Electron Spectroscopy and Related Phenomena*, 195:231–236, 2014.
- [38] P. Schwerdtfeger. Table of experimental and calculated static dipole polarizabilities for the electronic ground states of neutral elements (in atomic units), 2016. URL <http://ctcp.massey.ac.nz/Tablepol2016.pdf>.
- [39] A. Lhuillier, X. F. Li, and L. A. Lompre. PROPAGATION EFFECTS IN HIGH-ORDER HARMONIC-GENERATION IN RARE-GASES. *Journal of the Optical Society of America B-Optical Physics*, 7(4):527–536, 1990.
- [40] C. M. Heyl, J. Gudde, A. L’Huillier, and U. Hofer. High-order harmonic generation with mu J laser pulses at high repetition rates. *Journal of Physics B-Atomic Molecular and Optical Physics*, 45(7):9, 2012.
- [41] J. Rothhardt, M. Krebs, S. Hadrich, S. Demmler, J. Limpert, and A. Tunnermann. Absorption-limited and phase-matched high harmonic generation in the tight focusing regime. *New Journal of Physics*, 16:15, 2014.
- [42] A.L. Lytle. *Phase Matching and Coherence of High-Order Harmonic Generation in Hollow Waveguides*. PhD thesis, University of Colorado, 2008.
- [43] T. Brabec and F. Krausz. Intense few-cycle laser fields: Frontiers of nonlinear optics. *Reviews of Modern Physics*, 72(2):545–591, 2000.
- [44] F. Lindner, W. Stremme, M. G. Schatzel, F. Grasbon, G. G. Paulus, H. Walther, R. Hartmann, and L. Struder. High-order harmonic generation at a repetition rate of 100 kHz. *Physical Review A*, 68(1):8, 2003.
- [45] C. T. Chiang, M. Huth, A. Trutzschler, M. Kiel, F. O. Schumann, J. Kirschner, and W. Widdra. Boosting laboratory photoelectron spectroscopy by megahertz high-order harmonics. *New Journal of Physics*, 17:8, 2015.
- [46] M. Krebs, S. Hadrich, S. Demmler, J. Rothhardt, A. Zair, L. Chipperfield, J. Limpert, and A. Tunnermann. Towards isolated attosecond pulses at megahertz repetition rates. *Nature Photonics*, 7(7):555–559, 2013.
- [47] P. Russbueltdt, T. Mans, J. Weitenberg, H. D. Hoffmann, and R. Poprawe. Compact diode-pumped 1.1 kW Yb:YAG Innoslab femtosecond amplifier. *Optics Letters*, 35(24):4169–4171, 2010.

- [48] M. Puppín, Y. P. Deng, O. Prochnow, J. Ahrens, T. Binhammer, U. Morgner, M. Krenz, M. Wolf, and R. Ernstorfer. 500 kHz OPCPA delivering tunable sub-20 fs pulses with 15 W average power based on an all-ytterbium laser. *Optics Express*, 23(2):1491–1497, 2015.
- [49] M. Puppín, Y. P. Deng, O. Prochnow, J. Matyschok, T. Binhammer, U. Morgner, M. Wolf, and R. Ernstorfer. *Fiber-Slab-Pumped OPCPA for XUV-Based Time-Resolved Photoelectron Spectroscopy at 500 kHz Repetition Rate*, volume 162 of *Springer Proceedings in Physics*, pages 766–769. Springer-Verlag Berlin, Berlin, 2015.
- [50] E. P. Ippen. Principles of Passive-Mode Locking. *Applied Physics B-Lasers and Optics*, 58(3):159–170, 1994.
- [51] A. Chong, J. Buckley, W. Renninger, and F. Wise. All-normal-dispersion femtosecond fiber laser. *Optics Express*, 14(21):10095–10100, 2006.
- [52] M. Bradler, P. Baum, and E. Riedle. Femtosecond continuum generation in bulk laser host materials with sub- μ J pump pulses. *Applied Physics B-Lasers and Optics*, 97(3):561–574, 2009.
- [53] D. G. Andrews. *An Introduction to Atmospheric Physics*. Cambridge University Press, Cambridge, U.K.; New York, U.S.A., 2000.
- [54] H. C. Bandulet, D. Comtois, A. D. Shiner, C. Trallero-Herrero, N. Kajumba, T. Ozaki, P. B. Corkum, D. M. Villeneuve, J. C. Kieffer, and F. Legare. High harmonic generation with a spatially filtered optical parametric amplifier. *Journal of Physics B-Atomic Molecular and Optical Physics*, 41(24):7, 2008.
- [55] Zenghu Chang. *Fundamentals of attosecond optics*. CRC Press, Boca Raton, FL, 2011.
- [56] Masahiko Daimon and Akira Masumura. High-accuracy measurements of the refractive index and its temperature coefficient of calcium fluoride in a wide wavelength range from 138 to 2326 nm. *Appl. Opt.*, 41(25):5275–5281, Sep 2002.
- [57] D. Eimerl, L. Davis, S. Velsko, E. K. Graham, and A. Zalkin. Optical, mechanical, and thermal properties of barium borate. *Journal of Applied Physics*, 62(5):1968–1983, 1987.
- [58] E. M. Bothschafter, A. Schiffrin, V. S. Yakovlev, A. M. Azzeer, F. Krausz, R. Ernstorfer, and R. Kienberger. Collinear generation of ultrashort UV and XUV pulses. *Optics Express*, 18(9):9173–9180, 2010.
- [59] E. Bothschafter. Collinear Generation and Characterization of Ultrashort UV and XUV Laser Pulses. Diplomarbeit, Universität Stuttgart, 2009.
- [60] P. J. Leonard. Refractive indices, verdet constants, and polarizabilities of the inert gases. *Atomic Data and Nuclear Data Tables*, 14(1):21.

-
- [61] Hans Pauly. *Atom, Molecule, and Cluster Beams I Basic Theory, Production and Detection of Thermal Energy Beams*. Springer Series on Atomic, Optical, and Plasma Physics. Springer Berlin Heidelberg, Berlin, Heidelberg, 2000.
- [62] J. P. Brichta, M. C. H. Wong, J. B. Bertrand, H. C. Bandulet, D. M. Rayner, and V. R. Bhardwaj. Comparison and real-time monitoring of high-order harmonic generation in different sources. *Physical Review A*, 79(3):6, 2009.
- [63] A. Cabasse, G. Machinet, A. Dubrouil, E. Cormier, and E. Constant. Optimization and phase matching of fiber-laser-driven high-order harmonic generation at high repetition rate. *Optics Letters*, 37(22):4618–4620, 2012.
- [64] M. Weinelt. Time-resolved two-photon photoemission from metal surfaces. *Journal of Physics-Condensed Matter*, 14(43):R1099–R1141, 2002.
- [65] R. Haight and D. R. Peale. ANTIBONDING STATE ON THE GE(111) - AS SURFACE - SPECTROSCOPY AND DYNAMICS. *Physical Review Letters*, 70(25):3979–3982, 1993.
- [66] R. Carley, K. Dobrich, B. Frietsch, C. Gahl, M. Teichmann, O. Schwarzkopf, P. Wernet, and M. Weinelt. Femtosecond Laser Excitation Drives Ferromagnetic Gadolinium out of Magnetic Equilibrium. *Physical Review Letters*, 109(5):4, 2012.
- [67] J. Hebling. Derivation of the pulse front tilt caused by angular dispersion. *Optical and Quantum Electronics*, 28(12):1759–1763, 1996.
- [68] L. Poletto, P. Villoresi, F. Frassetto, F. Calegari, F. Ferrari, M. Lucchini, G. Sansone, and M. Nisoli. Time-delay compensated monochromator for the spectral selection of extreme-ultraviolet high-order laser harmonics. *Review of Scientific Instruments*, 80(12):8, 2009.
- [69] R. Haight and D. R. Peale. TUNABLE PHOTOEMISSION WITH HARMONICS OF SUBPICOSECOND LASERS. *Review of Scientific Instruments*, 65(6):1853–1857, 1994.
- [70] B. L. Henke, E. M. Gullikson, and J. C. Davis. X-RAY INTERACTIONS - PHOTOABSORPTION, SCATTERING, TRANSMISSION, AND REFLECTION AT $E=50\text{--}30,000$ EV, $Z=1\text{--}92$. *Atomic Data and Nuclear Data Tables*, 54(2):181–342, 1993.
- [71] C. Kan, C. E. Capjack, R. Rankin, and N. H. Burnett. SPECTRAL AND TEMPORAL STRUCTURE IN HIGH HARMONIC EMISSION FROM IONIZING ATOMIC GASES. *Physical Review A*, 52(6):R4336–R4339, 1995.
- [72] M. E. Davila and G. Le Lay. Few layer epitaxial germanene: a novel two-dimensional Dirac material. *Scientific Reports*, 6:20714, 2016.

- [73] Lebow Company. About Foils. URL `\url{http://www.lebowcompany.com/about_foils.htm}`.
- [74] E. Gullikson. X-Ray Interactions With Matter. URL `\url{http://henke.lbl.gov/optical_constants/}`.
- [75] S. Cho, J. Yu, S. K. Kang, and D. Y. Shih. The oxidation of lead-free Sn alloys by electrochemical reduction analysis. *Jom*, 57(6):50–52, 2005.
- [76] A.R. Rundquist. *Phase-matched generation of coherent, ultrafast x-rays using high harmonics*. PhD thesis, Washington State University, 1998.
- [77] Popmintchev, T. and Chen, M. C. and Cohen, O. and Grisham, M. E. and Rocca, J. J. and Murnane, M. M. and Kapteyn, H. C. Extended phase matching of high harmonics driven by mid-infrared light. *Optics Letters*, 33(18):2128–2130, 2008.
- [78] H. Hertz. Ueber einen Einfluss des ultravioletten Lichtes auf die elektrische Entladung. *Annalen der Physik*, 267(8):983–1000, 1887.
- [79] A. Einstein. Über einen die Erzeugung und Verwandlung des Lichtes betreffenden heuristischen Gesichtspunkt [AdP 17, 132 (1905)]. *Annalen der Physik*, 14(S1):164–181, 2005.
- [80] Stefan Hüfner. *Photoelectron Spectroscopy Principles and Applications*. Advanced Texts in Physics. Springer Berlin Heidelberg, Berlin, Heidelberg, third revised and enlarged edition edition, 2003.
- [81] H. Vita. *Interaction of magnetic and non-magnetic metals with graphene*. PhD thesis, Humboldt-Universität zu Berlin.
- [82] K. F. Mak, C. Lee, J. Hone, J. Shan, and T. F. Heinz. Atomically Thin MoS₂: A New Direct-Gap Semiconductor. *Physical Review Letters*, 105(13):4, 2010.
- [83] R. Bertoni et al. Generation and evolution of spin-, valley- and layer-polarized excited carriers in inversion-symmetric WSe₂. *eprint arXiv:1606.03218*, 2016.
- [84] D. Xiao, G. B. Liu, W. X. Feng, X. D. Xu, and W. Yao. Coupled Spin and Valley Physics in Monolayers of MoS₂ and Other Group-VI Dichalcogenides. *Physical Review Letters*, 108(19):5, 2012.
- [85] SPECS Surface Nano Analysis GmbH. *PHOIBOS 100/150 Hemispherical Energy Analyzer Series*, 2008. Technical Manual.
- [86] S. Hüfner. *Very High Resolution Photoelectron Spectroscopy*. Lecture Notes in Physics. Springer Berlin Heidelberg, Berlin, Heidelberg, 2007.

- [87] J. M. Schins, P. Breger, P. Agostini, R. C. Constantinescu, H. G. Muller, A. Bouhal, G. Grillon, A. Antonetti, and A. Mysyrowicz. Cross-correlation measurements of femtosecond extreme-ultraviolet high-order harmonics. *Journal of the Optical Society of America B-Optical Physics*, 13(1):197–200, 1996.
- [88] L. Miaja-Avila, C. Lei, M. Aeschlimann, J. L. Gland, M. M. Murnane, H. C. Kapteyn, and G. Saathoff. Laser-Assisted Photoelectric Effect from Surfaces. *Phys. Rev. Lett.*, 97:113604, 2006.
- [89] T. J. Driscoll, G. M. Gale, and F. Hache. TI SAPPHIRE 2ND-HARMONIC-PUMPED VISIBLE RANGE FEMTOSECOND OPTICAL PARAMETRIC OSCILLATOR. *Optics Communications*, 110(5-6):638–644, 1994.
- [90] E. Riedle, M. Beutter, S. Lochbrunner, J. Piel, S. Schenkl, S. Sporlein, and W. Zinth. Generation of 10 to 50 fs pulses tunable through all of the visible and the NIR. *Applied Physics B-Lasers and Optics*, 71(3), 2000.
- [91] J. Piel, E. Riedle, L. Gundlach, R. Ernstorfer, and R. Eichberger. Sub-20 fs visible pulses with 750 nJ energy from a 100 kHz noncollinear optical parametric amplifier. *Optics Letters*, 31(9):1289–1291, 2006.
- [92] R. L. Fork, O. E. Martinez, and J. P. Gordon. NEGATIVE DISPERSION USING PAIRS OF PRISMS. *Optics Letters*, 9(5):150–152, 1984.

Acknowledgements

My special gratitude belongs to my LMU advisor Prof. Dr. Matthias Kling, who took the burden upon him to supervise me in this external master's thesis!

The same accounts for Dr. Ralph Ernstorfer, who offered me to do my thesis as a part of his fantastic group. Thanks for many detailed insights into physics during the discussions. I also want to thank Prof. Dr. Martin Wolf, the director of the physical chemistry department at the FHI.

Thanks to Michele Puppin, who guided me through my practical work.

For many helpful comments and time, I also want to thank Dr. Laurenz Rettig.

Thanks Dr. Hendrik Vita for detailed help, whenever it was necessary.

For having a good time in the group, I want to thank Christoper Nicholson, Jannik Malter, Dr. Daniel Wegkamp, Dr. Lutz Waldecker, Manuel Krüger and the rest of the Fabekstraßen crew.

For perfect and friendly technical support, thanks to Sven Kubala and Reinhard Franke.

Last but not least, thanks to Jan, Christian, Susanne, my family and especially Stella, who supported me over the last month!

Erklärung

Hiermit erkläre ich, die vorliegende Arbeit selbständig verfasst zu haben und keine anderen als die in der Arbeit angegebenen Quellen und Hilfsmittel benutzt zu haben.

Ort, Datum

Unterschrift